Magnetic Properties Studied by Density Functional Calculations Including Orbital Polarisation Corrections

DISSERTATION

zur Erlangung des akademischen Grades

Doktor rerum naturalium
(Dr. rer. nat.)

vorgelegt

der Fakultät Mathematik und Naturwissenschaften
der Technischen Universität Dresden

DIPL. PHYS. CARSTEN NEISE
geboren am 12.09.1981 in Dresden

Eingereicht am 16.12.2010

LEIBNIZ-INSTITUT FÜR FESTKÖRPER- UND
WERKSTOFFFORSCHUNG DRESDEN

1. Reviewer: Prof. Dr. Helmut Eschrig
2. Reviewer: Prof. Dr. Hubert Ebert

Day of the defense: 08.06.2011

Contents

List of Figures

List of Tables

List of Abbreviations

ϵ	electrostatic electron charge
ϵ_0	vacuum permittivity
$\hbar$	reduced Planck's constant
μ_0	vacuum permeability
μ_B	**B**ohr magneton
μ_l	orbita**l** moment
μ_s	**s**pin moment
μ_{tot}	**tot**al moment
σ	stress
eV	electron **V**olt
Ha	**Ha**rtree
Pa	**Pa**scal
Ry	**Ry**dberg
$a.u.$	**a**tomic **u**nits
a_B	**B**ohr radius
c	speed of light
e	electrodynamic **e**lectronic charge
m_e	**e**lectronic **m**ass
M_i	**m**ass of nuclei
N_A	**A**vogrado's constant
Å	**A**ngstroem
AD	**ad**iabatic approach
APW	**a**ugmented **p**lane **w**aves
ARPES	**a**ngle **r**esolved **p**hoto**e**mission **s**pectra
ASA	**a**tomic **s**phere **a**pproximation
ASW	**a**ugmented **s**pherical **w**aves
BO	**B**orn-**O**ppenheimer
C	**c**orrelation
CDFT	**c**urrent **d**ensity **f**unctional **t**heory
CPA	**c**oherent **p**otential **a**pproximation
cRPA	**c**onstraint **r**andom **p**hase **a**pproximation
DC	**d**ouble **c**ounting
DFT	**d**ensity **f**unctional **t**heory
DMFT	**d**ynamical **e**an **f**ield **t**heory
DOS	**d**ensity **o**f **s**tates
EAVG	**e**nsemble **av**era**g**e
EBP	**e**pitaxial **B**ain **p**ath
EdH	**E**instein **d**e **H**aas
EXP	**e**x**p**eriment
EXX	**e**xact e**x**change
f.u.	**f**ormula **u**nit
FP-LMTO	**f**ull **p**otential linearized **m**uffin-**t**in **o**rbitals method
FPLO	**f**ull **p**otential nonorthogonal **l**ocal **o**rbital minimum basis band structure scheme
FSM	**f**ixed **s**pin **m**oment
FT	**f**orce **t**heorem
GGA	**g**eneralized **g**radient **a**pproximation
HF	**H**artree **F**ock

1

Introduction

Understanding macroscopic properties of solids requires the knowledge and the interpretation of the electronic and the magnetic structure. Since the beginning of last century tremendous progress in this field has been made. The *Born-Oppenheimer approximation* [1], in which the motion of the nuclei is separated from the motion of the electrons, was a crucial step in electronic structure theory in the 1920s. Another successful achievement was the development of the *Hartree-Fock* (HF) method [2–4]. In HF theory, the single-particle wave function of the electrons is used to solve the many-body problem. One should keep in mind that the number of particles in solids is of the order of 10^{23}, and there are three times more coupled differential equations, which have to be solved. Although computer power increases faster and faster nowadays, it remains hopeless to solve the many-body problem numerically without further simplifications. A milestone was the formulation of the *Thomas-Fermi* (TF) theory [5, 6]. It was the first model which reduced the many-body problem to the electron density, for which only a single 3-dimensional integral equation has to be solved. Despite its success the TF model suffers from its crude approximation of the kinetic energy and the absence of *exchange- and correlation* (XC) effects.

Since the introduction in the 1960s, *density functional theoretical* DFT investigations have been established as an important branch of condensed matter physics. This method is one of the most-widely used nowadays. The fundamental ideas were developed by Kohn, Hohenberg, and Sham [7, 8]. Hohenberg and Kohn proved that there exists at most one potential for a given ground-state density. Later on, Kohn and Sham established the famous Kohn-Sham equation which provides a formally exact solution of the many-body problem for the ground-state by introducing a so-called XC potential. This potential includes all interaction effects beyond mean-field theory. However, even though the Kohn-Sham equations formally provide an exact solution one can not solve them, because the figuring XC potential is not known. Approximations are needed for this XC potential. Thus the accuracy of the calculated ground-state properties of atoms, molecules, and solids depends on the chosen approximation for the XC potential.

Kohn and Sham proposed the most straightforward approximation for the XC potential, the *local density approximation* (LDA) [8]. The generalisation into a spin dependent formalism (LSDA) was done by von Barth and Hedin [9]. Itinerant magnetism is described quite successfully within LSDA, e.g. the Stoner parameter [10, 11] is accessible by DFT calculations [12]. Even though LDA and LSDA are approaches for the homogeneous electron gas, they provide surpris-

ingly accurate results while being computationally very convenient. However a more realistic description of inhomogeneous systems would be to include gradient terms of the XC potential with respect to the electron density. One most successful recent attempt in this field is called *generalised gradient approximation* (GGA). Higher order derivatives have been included in the XC potential over the last years [13]. These approaches are referred to by the name *meta-GGA*. It seems that GGA gives more realistic bond lengths for most of the investigated compounds than obtained within LDA. But the magnetism for the most studied cases of d- and f-shells is equally well reflected in LSDA and in GGA if the same volume is used in the calculations. In order to find the correct ground-state, calculations combining the analysis of structural and magnetic properties have to be done. Take, for example, the element Fe for which in collinear LSDA the ground-state is obtained to be non-magnetic in the *face centered cubic* (FCC) structure. Nevertheless nature prefers a strong ferromagnet in the *body centered cubic* (BCC) structure. This is perfectly obtained within GGA. The "homogeneous electron gas" ansatz fails if one wants to describe so-called strongly correlated systems, e.g. consider transition metal oxides as CoO, NiO, or CuO. In those compounds a strong coulomb repulsion in the incompletely screened d states exists, which is neither included in LSDA nor in GGA. Thence a metallic behaviour is obtained, while experiments verify Mott insulators. The inclusion of local Coulomb repulsion remedies this discrepancy between theory and experiment. This method is known as the LSDA+U method [14, 15].

It seems that for metallic systems the *spin polarisation* (SP) is already well described within LSDA (and GGA). However, there are discrepancies between the measured and calculated orbital magnetic properties, which are accessible in relativistic calculations only. Hence the question arises how to include *orbital polarisation* (OP) into DFT in a proper way. In atoms Hund's rules are satisfied, which describe SP, OP and *spin orbit* (SO) coupling in atoms. Typical energy scales in atoms according to Hund's rules are about $1 \ldots 10$ eV for the spin polarisation, $0.1 \ldots 2$ eV for orbital polarisation as well as SO coupling [16]. The atomic energies are altered in solids and then their order may be transposed in comparison to free atoms. E.g. band formation, crystal field, and hybridization of the valence electrons tend to quench the orbital moment. So OP is reduced in these compounds, e.g. in $3d$ transition metals the orbital moment is one order of magnitude smaller than the spin moment.

One significant part in this thesis is to investigate the effect of OP, e.g. in actinide systems. Recall, that relativistic effects become crucial for atomic numbers above 30, e.g. the *magneto-crystalline anisotropy* energy (MCA) is caused by the SO splitting and hence rests on a correct description of both spin and orbital polarisation. It is analysed in this work as well. Several ways to include relativistic effects into DFT have been derived since the 1970s. For this purpose the quantum field theoretical variant of the Hohenberg and Kohn principle was applied [17]. The result was a theory based on the four-*current-density functional* (CDFT), which was pointed out to include magnetism in a very natural way. The relativistic version of the Hohenberg and Kohn variational principle leads to the Kohn-Sham-Dirac equation [13, 18]. Approximate variants kept the spin current, including its XC spin polarisation, and neglected the exchange and correlation contribution of orbital currents [19, 20]. OP results from the interplay of SP and SO coupling and is not caused by correlation effects. However, these two couplings break time-reversal symmetry leading

to a non-zero orbital current density. Orbital moments of d and f metals are calculated which are smaller by a factor of two than the related experimental orbital moments [16]. Another scheme, in which the "paramagnetic" current density and the spin density are considered independently in the non-relativistic limit [21–23], is suitable for systems in very high magnetic fields. It also allows to calculate ground-state properties of very light open-shell atoms since SO interaction is not taken into account. However, this method is not a good starting point for $3d$ metals, in which OP is caused by SO coupling, and for f shells, in which OP energies and SO energies are of comparable size [24]. The systematic underestimation of orbital moments in d and f metals leads to the conclusion that the inclusion of an XC enhancement of the OP is needed, this is what we will call *OP corrections* (OPC). In practise an orbital dependent functional is added to the energy functional [25], which shows similarities to the LSDA+U approach [26].

Many different band structure approaches have been developed during past decades. Until the early 1990s shape restrictions (muffin-tin based methods) had to be taken into account to the periodic potential due to the limitation in computer power. This restriction is nowadays obsolete and full-potential methods have become the rule. A lot of different methods had been suggested, which for instance differ in the used basis sets or the used potentials. The main methods are the *linear muffin-tin orbital* (LMTO) [27], the *Korringa-Kohn-Rostocker* (KKR) [28, 29], the *augmented spherical waves* (ASW) [30], the *augmented plane waves* (APW) [31], the *linearised augmented plane waves* (LAPW) approach [27, 32]. An example for the KKR method is the *spin polarised relativistic* (SPR)-KKR [33] code, an example for the LAPW method is the Wien2k [1] code. Another approach is the *linear combination of atomic orbitals* (LCAO) method [34] which yields the basic principles for the *full potential nonorthogonal local orbital band structure scheme* (FPLO) [2]. Full potential means that no shape restriction is implemented anymore. This work was done using the FPLO package [35]. Anyhow, there are many different codes available, some of them provide an accuracy in the range of mHartree for the total energy and hence these codes yield comparable results, e.g. SPR-KKR, Wien2k and FPLO.

In this thesis, magnetic properties under three different OP schemes are analysed by DFT calculations using LSDA and GGA. This thesis is organised as follows: The theoretical background of non-relativistic and relativistic DFT is presented in Chapter 2, also including a brief overview of the used band structure program. Chapter 3 addresses the technical realisation of OPC within the band structure package. A first application of OPC can be found in Chapter 4, in which $3d$ transition metals and alloys are investigated. In Chapter 5 uranium compounds are considered, in which SO coupling becomes more important. This chapter covers the question how OP evolves in systems which have $5f$ character. Finally, a short summary as well as an outlook is presented in Chapter 6.

---

[1] http://wien2k.at
[2] http://www.fplo.de

2

Theoretical Considerations

DFT provides a powerful tool to calculate many measurable properties of solids, e.g. magnetism, stress, crystal structure etc. In this way DFT supplies the theoretical foundation of all the electronic structure calculations done in this work bearing in mind that DFT is a mathematically exact formulation of the many-body problem for the electronic ground-state. Therein, the Schrödinger equation is mapped onto an effective one-particle equation, which can be solved numerically.

In the 1960s two basic theorems were established by Hohenberg and Kohn [7], and Kohn and Sham [8]. Hohenberg and Kohn formulated a variational principle, in which the ground-state energy of N_e interacting electrons moving in an external potential $\nu(\mathbf{r})$ can be represented as the minimum of energy with respect to the electron density. Later on, Kohn and Sham presented an effective one-particle formalism. A mathematical more rigorous formulation of the problem has been worked out by Levy [36] and Lieb [37], which is briefly discussed in this context.

Section 2.1 begins with a short presentation of the basic Hamiltonian considered in many particle physics. In Section 2.2 the focus changes from non-relativistic DFT to relativistic DFT. Section 2.3 presents the used band structure package [35], which is used during the this work. Section 2.4 introduces the concept of MCA and explains how MCA energies are calculated within DFT. Finally, Section 2.5 presents several used possibilities of describing disorder in DFT. The textbooks [13, 38, 39] are suggested for further reading. The outline of the section considering DFT was motivated in particular by the book of Eschrig [40] in which more details can be found.

All the following chapters apply *atomic units* (*a.u*). They are tabulated in the Eqns. (2.1), (2.2) and (2.3). Planck's constant is denoted as $\hbar$, m_e signifies the electron mass and the electrostatic electron charge is labelled with $\epsilon = e/\sqrt{4\pi\,\epsilon_0}$, the electrodynamic electron charge is characterised by $e = \sqrt{4\pi\,\epsilon_0}\epsilon$, and ϵ_0, μ_0 represents the vacuum permittivity and the vacuum permeability, respectively. Typical energies are given in eV and typical lengths are characterised in Å. The velocity of light in the vacuum is $c = 137.03599\,a.u.$

$$1\,a.u. \;\;=\;\; \hbar = m_e = \epsilon^2 = 2\,\mu_B \tag{2.1}$$

$$1\,\text{Ha} \;\;=\;\; 2\,\text{Ry} = 27.2113845\,\text{eV} \tag{2.2}$$

$$1\,a_\text{B} \;\;=\;\; 5.291772108 \cdot 10^{-11}\,\text{m} = 0.5291772108\,\text{Å} \tag{2.3}$$

2.1   Quantum Mechanics Applied to Solids

The stationary Schrödinger equation is analytically solvable for certain potentials up to the two and the three body problem, Eqns. (2.4) - (2.8), with $N_e + N_e$ = 2, 3. So, numerical solutions have to be obtained in case of larger systems. In (2.4), $\hat{\mathcal{H}}$ is called the Hamilton operator, containing the information for a particular problem. If Eqn. (2.4) is fulfilled, then $|\Psi_m\rangle$ is called eigenfunction, and E_m is the eigenenergy. The index m counts the eigenfunctions.

$$\hat{\mathcal{H}}\,|\Psi_m\rangle = E_m\,|\Psi_m\rangle \tag{2.4}$$

The aim in many-particle physics is to formulate problem (2.4) for solids with N_e electrons and N_n nuclei. The many body state for N_e electrons $|\Psi_{N_e}\rangle$ obeys the fermionic symmetry and is written in the Schrödinger representation $\Psi_{N_e}(\{x_k\}) \equiv \Psi(x_1, \ldots, x_{N_e}) = \langle x_1, \ldots, x_{N_e}|\Psi_{N_e}\rangle$, which is a projection of the abstract Hilbert vector Ψ_{N_e} into the $\mathbf{r}$- and the spin space and is usually called a wave function. For further notation the variable x combines space variable $\mathbf{r}$ and spin variable s. The Hamilton operator $\hat{\mathcal{H}}$ of an interacting many-body system with N_e interacting electrons and N_n interacting nuclei is given by

$$\hat{\mathcal{H}} = \hat{\mathcal{H}}_e + \hat{\mathcal{H}}_n + \hat{\mathcal{H}}_{e-n} + \hat{\mathcal{H}}_{ext}, \tag{2.5}$$

in which

$$\hat{\mathcal{H}}_e = \sum_k^{N_e} \frac{\hat{\mathbf{p}}_k^2}{2} + \frac{1}{2}\sum_{k \neq k'}^{N_e} \frac{1}{|\mathbf{r}_k - \mathbf{r}_{k'}|} \tag{2.6}$$

$$\hat{\mathcal{H}}_n = \sum_i^{N_n} \frac{\hat{\mathbf{P}}_i}{2M_i} + \frac{1}{2}\sum_{i \neq i'}^{N_n} \frac{Z_i Z_{i'}}{|\mathbf{R}_i - \mathbf{R}_{i'}|} \tag{2.7}$$

$$\hat{\mathcal{H}}_{e-n} = -\sum_k^{N_e}\sum_i^{N_n} \frac{Z_i}{|\mathbf{r}_k - \mathbf{R}_i|}. \tag{2.8}$$

$\hat{\mathcal{H}}_e$, $\hat{\mathcal{H}}_n$, and $\hat{\mathcal{H}}_{e-n}$ are the electron-electron, nuclei-nuclei, and the electron-nuclei interaction, respectively. $\hat{\mathcal{H}}_e$ and $\hat{\mathcal{H}}_n$ are split into an kinetic and a Coulomb part. $\hat{\mathcal{H}}_{ext}$ describes a coupling between the charge density or magnetisation density with a corresponding external electric or magnetic field. The nomenclature used above is defined as follows, M_i is the static mass of ion i, $\hat{P}_i$, and $\hat{p}_k$ are the momentum operators of ion i and electron k, Z_i denotes the nuclear charge of ion i, $\mathbf{R}_i$ and $\mathbf{r}_k$ label the positions of ion i and electron k.

The typical magnitude of N_e and of N_n is of the order of the Avogadro constant N_A [1]. Eqn. (2.5) inserted into the eigenvalue problem (2.4) discloses that no computer is able to solve this many body problem without simplifications. The adiabatic approximation (AD) avails itself of the mean ratio between

---

[1] $N_A = 6.02214179(30) \cdot 10^{23}\,mol^{-1}$

m_e and M_i [2]. Consequently, it is justified to argue that at any time the electrons feel a static potential caused by the nuclei at rest. As a result of this static potential the motion of the electrons and the motion of the nuclei can be separately treated [3]. As far as only the electrons are concerned the Hamilton operator (2.5) can be written in the following form,

$$\hat{\mathcal{H}}_e^{AD}\left(\mathbf{R}_i,\,Z_i\right) = \hat{\mathcal{H}}_e + \sum_k^{N_e}\sum_i^{N_n}\frac{Z_i}{|\mathbf{r}_k-\mathbf{R}_i|} + const.\left(\mathbf{R}_i\right) \quad (2.9)$$

$$\hat{\mathcal{H}}_e^{AD}\left(\mathbf{R}_i,\,Z_i\right)\Psi_{N_e}\left(\{x_k\}\right) = E_e\left(\mathbf{R}_i,\,Z_i\right)\Psi_{N_e}\left(\{x_k\}\right). \quad (2.10)$$

The eigenvalue equation (2.10) can be solved with respect to the static configuration ($\{\mathbf{R}_i\}$) of the ions. One selected eigenenergy of Eqn. (2.10) is then inserted in the Hamilton operator of the ions, and the corresponding eigenvalue problem $\mathcal{H}_n + E_e$ has to be tackled.

The result of the AD is that the number of equations of the original problem (2.5) is reduced to the number of electrons N_e only and to fermionic symmetry. Nevertheless, the remaining degrees of freedom in (2.9) are still too many to solve them exactly. The following sections describe a way of using the density instead of using the many body wavefunction to solve the many body problem.

2.2 Density Functional Theory

2.2.1 non-Relativistic DFT

2.2.1.1 Hohenberg and Kohn

We are left with solving the problem (2.10). We rewrite the many-body problem, omitting the index AD, in its spin dependent formalism (2.11),

$$\hat{\mathcal{H}}_e\left[\nu,N_e\right] = \hat{\mathcal{H}}_e + \nu. \quad (2.11)$$

Here $\hat{\mathcal{H}}_e\left[\nu,\,N_e\right]$ is now written as a functional of the electron number N_e and any external spin dependent potential ν. The external potential ν is build as the sum of the electron-nuclei potential $\hat{\mathcal{H}}_{e-n}$ and possibly an applied electromagnetic field. The spin density[4] is defined as,

$$n_{ss'}\left(\mathbf{r}\right) = \int \Psi_{N_e}\left(\mathbf{r}s,\,x_2,\,\ldots\right)\Psi_{N_e}^*\left(\mathbf{r}s',\,x_2,\,\ldots\right)dx_2\,\ldots\,dx_{N_e}. \quad (2.12)$$

Here, $\int dx$ means integration over $\mathbf{r}$ and summation over s. In what follows we assume spin collinearity, $n_{ss'} = \delta_{ss'}n\left(\mathbf{r},\,s\right)$. If $n\left(\mathbf{r},\,\uparrow\right) = n\left(\mathbf{r},\,\downarrow\right)$ a first Theorem by Hohenberg and Kohn holds:

---

[2] $\frac{m_e}{M_i} \approx 10^{-3}\ldots 10^{-5}$

[3] The adiabatic approach rests on the smallness of ω_{ph}/ϵ_f, where ω_{ph} is the maximum phonon energy and ϵ_f is the Fermi energy measured from the next van Hove singularity of the electronic density of states.

[4] The spin appears naturally in the non-relativistic limit out of the relativistic formulation of the Schrödinger equation, it will be introduced in Section 2.2.2

Theorem 1 $\nu\left(\mathbf{r}\right) \in \mathcal{V}_{N_e}$ *is up to an* $\mathbf{r}$*-independent constant a unique function of the ground-state density* $n\left(\mathbf{r}\right)$*.*

The potentials $\nu\left(\mathbf{r}\right)$ are restricted on the set $\mathcal{V}_{N_e}$, which admits only p-integrable potentials, in particular $\nu\left(\mathbf{r}\right) \in \mathbf{L}^p$ satisfies the condition of the p-norm: $\|\nu\|_p = \left|\int d^3\mathbf{r}\,|\nu\left(\mathbf{r}\right)|^p\right|^{\frac{1}{p}} < \infty$ for $1 \leq p < \infty$. It is further necessary that $\hat{\mathcal{H}}_e\left[\nu, N_e\right]$ has a ground-state for these particular potentials. Originally, the theorem was formulated for non-degerenate ground-states as a one-one mapping between $\nu\left(\mathbf{r}\right)$ and ground-state density $n\left(\mathbf{r}\right)$. Indepently, Levy and Lieb extended the density functional theory for degenerate ground-states and to ensemble states. The properties of ensemble states are briefly summarised. The admission of ensemble states is motivated by the idea that increasing the the variational freedom increases the set of ground-states eventually. Now, let $\hat{\gamma}$ be the statistical operator for ensemble states,

$$\hat{\gamma} = \sum_K |\Psi_K\rangle\, g_K\, \langle\Psi_K|; \qquad 0 \leq g_K \leq 1; \qquad \sum_K g_K = 1. \qquad (2.13)$$

The $|\Psi_K\rangle$ are normalised pure states possessing a statistical probability g_K and a corresponding particle number N_K. The $|\Psi_K\rangle$ are expanded into an orthonormal set of eigenstates of the particle number operator $\hat{N}_e$. The total electron number N_e is obtained as expectation value of the particle number operator $\hat{N}_e$, via

$$N_e = \mathrm{Tr}\left(\hat{\gamma}\,\hat{N}_e\right) = \sum_K g_K N_K \qquad (2.14)$$

and being non-negative and real. The expectation value of the Hamiltonian $\hat{\mathcal{H}}_e$ (2.11), being a functional of the total particle Number N_e and of the external potentials ν, supplies the total energy of the system: $E_{total} = \mathrm{Tr}\left(\hat{\gamma}\,\hat{\mathcal{H}}_e\right)$. The ground-state energy E is obtained by taking the infimimum over the admissible density operators $\hat{\gamma}$ under the constraint of keeping the particle number N_e fixed,

$$E\left[\nu,\, N_e\right] \equiv \inf_{\hat{\gamma}}\left\{\mathrm{Tr}\left(\hat{\gamma}\hat{\mathcal{H}}_e\right) \mid \mathrm{Tr}\left(\hat{\gamma}\,\hat{N}_e\right) = N_e\right\}. \qquad (2.15)$$

The principle advantage of taking mixed states as compared to the expansion of a pure state into a basis, is now the linear dependence of Eqn. (2.15) on the mixing coefficient g_K. This linear dependence confines the search of the minimum on the boundary of the domain spanned by the g_K. In this way degenerate ground-states may be included in DFT. It is easily verified, that $E\left[\nu,\, N_e\right]$ has the following properties [40].

Property 1 $\quad E\left[\nu + c,\, N_e\right] = E\left[\nu,\, N_e\right] + N_e\, c$: gauge invariance with respect to a constant potential shift c

Property 2 $\quad E\left[\nu,\, c\, N_{e,1} + \left(1 - c\right) N_{e,2}\right] \leq c\, E\left[\nu,\, N_{e,1}\right] + \left(1 - c\right) E\left[\nu,\, N_{e,2}\right]$: convexity in N_e for fixed ν

Property 3 $E\left[c\,\nu_1 + (1-c)\,\nu_2,\, N_e\right] \geq c\,E\left[\nu_1,\, N_e\right] + (1-c)\,E\left[\nu_2,\, N_e\right]$: concavity in ν for fixed N_e

Convexity of $E\left[\nu,\, N_e\right]$ in N_e is guaranteed by property 2, which allows to define a Legendre transformed functional $\tilde{G}\left[\nu,\, \mu\right]$ with respect to the total particle number N_e of the ground-state energy $E\left[\nu,\, N_e\right]$ (2.15).

$$\tilde{G}\left[\nu,\, \mu\right] \equiv \sup_{N_e} \left\{\mu N_e - E\left[\nu,\, N_e\right]\right\} \tag{2.16}$$

$$\tilde{G}\left[\nu,\, \mu\right] = \tilde{G}\left[\nu - \mu,\, 0\right] \equiv G\left[\nu - \mu\right] \tag{2.17}$$

$$G\left[\nu - \mu\right] = -\inf_{N_e} \left\{E\left[\nu - \mu,\, N_e\right]\right\} \tag{2.18}$$

$$E\left[\nu,\, N_e\right] = \sup_{\mu} \left\{N_e \mu - G\left[\nu - \mu\right]\right\} \tag{2.19}$$

The variable μ represents the chemical potential of the system. Making use of gauge property 1, one derives at a functional $G\left[\nu - \mu\right]$ which is dependent on $\nu - \mu$ only, Eqn. (2.17). Further on, we put $\mu = 0$ and write the Legendre transformed functional as $G\left[\nu\right]$. $G\left[\nu\right]$ is convex in ν, as $-E\left[\nu,\, N_e\right]$ is.

Now we return to the collinear spin case: $\nu\left(x\right) = \left(\nu\left(\mathbf{r},\, \uparrow\right),\, \nu\left(\mathbf{r},\, \downarrow\right)\right)$, $n\left(x\right) = \left(n\left(\mathbf{r},\, \uparrow\right),\, n\left(\mathbf{r},\, \downarrow\right)\right)$. Introducing $-n$ as a variable dual to ν with $\langle -n | \nu \rangle = -\sum_s \int n\left(\mathbf{r},\, s\right) \nu\left(\mathbf{r},\, s\right)\, d^3r$, the above considerations allow to define a density functional $H\left[n\right]$ as the Legendre transformation of $G\left[\nu\right]$, with the conjugate pair $(\nu,\, -n)$. See next page for the functional spaces X and X^*.

$$\tilde{H}\left[-n\right] \equiv \sup_{\nu \in X^*} \left\{\langle -n | \nu \rangle - G\left[\nu\right]\right\} \equiv H\left[n\right] \tag{2.20}$$

$$G\left[\nu\right] = \sup_{n \in X} \left\{\langle \nu | -n \rangle - H\left[n\right]\right\}$$

$$= -\inf_{n \in X} \left\{H\left[n\right] + \langle \nu | n \rangle\right\} \tag{2.21}$$

Applying (2.16) into Eqn. (2.20), one gets

$$H\left[n\right] \equiv \sup_{\nu \in X^*} \left\{- \langle n | \nu \rangle + \inf_{N_e} E\left[\nu,\, N_e\right]\right\} \tag{2.22}$$

$$\leq \inf_{N_e} \sup_{\nu \in X^*} \left\{E\left[\nu,\, N_e\right] - \langle n | \nu \rangle\right\}^5 \tag{2.23}$$

$$= \inf_{N_e} F\left[n,\, N_e\right], \tag{2.24}$$

in which $F\left[n,\, N_e\right] \equiv \sup \left\{E\left[\nu,\, N_e\right] - \langle n | \nu \rangle \mid \nu \in X^*\right\}$ is defined as a density functional that was first introduced by Lieb [37]. Originally, the density functional $F\left[n\right]$ was defined as $F\left[n\right]_{HK} \equiv E\left[\nu\left[n\right]\right] - \langle \nu\left(n\right) | n \rangle$ by Hohenberg and Kohn. In their work the density was restricted to come from an N_e-particle ground-state. The principle advantage by introducing $F\left[n,\, N_e\right]$ as seen above is that $F\left[n,\, N_e\right]$ is defined on the whole linear space X as compared to $F\left[n\right]_{HK}$,

---

[5]here we used the general rule sup inf $\leq$ inf sup

which is not. A further gain is that it yields $F\left[n\right]_{HK} = F\left[n, N_e\right]$ supporting an equal solution for (2.24). Finally, the variational principle by Hohenberg and Kohn is obtained by inserting Eqn. (2.21) into Eqn. (2.19).

$$E\left[\nu, N_e\right] \;=\; \sup_{\mu}\left\{N_e\mu \;+\; \inf_{n \in X}\left\{H\left[n\right] \;+\; \langle\nu - \mu|\,n\rangle\right\}\right\} \tag{2.25}$$

$$\leq \;\; \inf_{n \in X}\left\{H\left[n\right] \;+\; \langle\nu|\,n\rangle \;+\; \sup_{\mu}\left[N_e - \langle1|\,n\rangle\right]\mu\right\}^{5} \tag{2.26}$$

$$= \;\; \inf_{n \in X}\left\{H\left[n\right] \;+\; \langle\nu|\,n\rangle \;\middle|\; \langle1|\,n\rangle = N_e\right\} \tag{2.27}$$

Since,

$$\sup_{\mu}\left[N_e - \langle1|\,\mu\rangle\right]\mu = \begin{cases}+\infty \\ 0\end{cases} \qquad\qquad \text{for } \langle1|\,n\rangle \overset{\neq}{=} N_e, \tag{2.28}$$

the total infimum can only be obtained for $\langle1|\,N\rangle = N_e$.

At the end of this section we want to stress that by definition only p-integrable densities on the topological space X are admitted. In particular, in the non-relativistic limit holds $p = 3$, $X = \mathbf{L}^3\left(\mathcal{R}^3\right)$. Periodic boundary conditions in $\mathcal{R}$-space can be introduced. This has a rigorous consequence on the above presented Eqns. (2.25) - (2.27). A substitution of the infinite $\mathcal{R}^3$-space of electron coordinates by a torus $\mathcal{T}^3$ with finite measure is allowed, yielding $X = \mathbf{L}^3\left(\mathcal{T}^3\right)$. The space X^* on which the potentials are defined is called the dual space to X. A further study leads to $X^* = \mathbf{L}^{\frac{3}{2}}\left(\mathcal{T}^3\right)$ and $\left(X^*\right)^* = X^{**} = X$ meaning X is reflexive. The fact that X is defined on the torus $\mathcal{T}^3$ admits a replacement of the infimum into a minimum, specifically in Eqn. (2.26). This leads to the famous Hohenberg-Kohn principle: $E\left[\nu, N_e\right] = \min_{n \in X}\left\{H\left[n\right] + \langle\nu|\,n\rangle \;\middle|\; \langle1|\,n\rangle = N_e\right\}$. The advantage of the preceding procedures is a replacement of the variational problem (2.15), in which the variation is examined over the states $\hat{\gamma}$, by a variation over the density n in the Hohenberg-Kohn principle (2.27). Unfortunately, the unknown functional $H\left[n\right]$ had to be introduced, for which a constructive expression has to be found.

2.2.1.2   Kohn-Sham Equations

We are left with choosing an appropriate expression for $H\left[n\right]$. For that purpose the functional $H\left[n\right]$ is split into an orbital variation part $K\left[n\right]$ and a density integral $L\left[n\right]$.

$$H\left[n\right] \;=\; K\left[n\right] + L\left[n\right] \tag{2.29}$$

$$K\left[n\right] \;=\; \min_{\phi_l,\, n_l}\left\{k\left[\phi_l, n_l\right]\right.$$

$$\left.\middle|\; \sum_l \phi_l^* n_l \phi_l = n,\; 0 \leq n_l \leq 1,\; \langle\phi_i|\,\phi_j\rangle = \delta_{ij}\right\} \tag{2.30}$$

$$L\left[n\right] \;=\; \int d^3\mathbf{r}\, n\left(\mathbf{r}\right) l\left(n_{ss'}\left(\mathbf{r}\right), \boldsymbol{\nabla}n_{ss'}\left(\mathbf{r}\right), \ldots\right) \tag{2.31}$$

Where we used $n_{ss'}(\mathbf{r}) = \sum_l \phi_l^*(\mathbf{r}s) n_l \phi_l(\mathbf{r}s')$ as the spin density matrix, the ϕ_l are the single-particle Kohn-Sham orbitals, and n_l label the occupation numbers. Further it is assumed that the functional derivative $\frac{\delta H[n]}{\delta n} \in X^*$ exists and is unique[6]

$$\frac{\delta H[n]}{\delta n} = \mu - \nu, \tag{2.32}$$

In order to find the minimum of $H[n]$ one must vary Eqn. (2.29) with respect to the Kohn-Sham orbitals $\phi_l^*(x)$, $x \in \mathcal{T}^3$. One arrives at Kohn-Sham type equations.

$$\left(\hat{k} + \nu(x) + \nu_L(x)\right)\phi_l(x) \qquad = \qquad \phi_l(x)\epsilon_l \tag{2.33}$$

$$\text{orbital operator } \hat{k}: \qquad \frac{\delta k}{\delta \phi_l^*(x)} \quad = \quad \hat{k}\phi_l(x)n_l \tag{2.34}$$

$$\text{local Kohn-Sham potential}: \qquad \nu_L(x) \quad = \quad \frac{\delta L[n]}{\delta n(x)} \tag{2.35}$$

The idea of Kohn-Sham was now to calculate $H[n]$ of N_e electrons in the following splitting.

$$H[n] \quad = \quad T[n] + E_h[n] + E_{xc}[n] \tag{2.36}$$

$$T[n] \quad = \quad \min_{\phi_l,\, n_l} \left\{ -\frac{1}{2} \sum_l n_l \langle \phi_l | \boldsymbol{\nabla}^2 | \phi_l \rangle \right. \tag{2.37}$$

$$\left. \left| \sum_l \phi_l^* n_l \phi_l = n,\, 0 \leq n_l \leq 1,\, \langle \phi_i | \phi_j \rangle = \delta_{ij} \right\} \tag{2.38} \right.$$

$$E_h[n] \quad = \quad \frac{1}{2} \int d^3\mathbf{r} \int d^3\mathbf{r}'\, \frac{n(\mathbf{r})n(\mathbf{r}')}{|\mathbf{r} - \mathbf{r}'|} \tag{2.39}$$

$T[n]$ represents the kinetic energy of an interaction-free ground-state with density $n(\mathbf{r})$, $E_h[n]$ is the Hartree energy for any density $n(\mathbf{r})$, including self-interaction. What is left is the so-called XC energy $E_{xc}[n]$. It contains the change in kinetic energy due to interaction. The final Kohn-Sham equations are derived under minimisation of Eqn. (2.36) with respect to Kohn-Sham orbitals ϕ_l^* and the particular side condition, that the orbitals ϕ_l are orthonormal. The Lagrange multipliers ϵ_l, which were introduced on the basis of the side condition, depict the Kohn-Sham eigenenergies of the system. The Kohn-Sham equations are:

$$\left(-\frac{\boldsymbol{\nabla}^2}{2} + \nu_{eff}(x)\right)\phi_l(x) = \phi_l(x)\epsilon_l, \qquad \nu_{eff} \equiv \nu + \nu_h + \nu_{xc} \tag{2.40}$$

The external potential ν, the Hartree potential ν_h and the Kohn-Sham XC potential ν_{xc} are defined as follows.

---

[6] A rigorous analysis can be found in [40].

$$\nu_h(x) \equiv \frac{\delta E_h[n]}{\delta n(x)} \tag{2.41}$$

$$\nu_{xc}(x) \equiv \frac{\delta E_{xc}[n]}{\delta n(x)} \tag{2.42}$$

If $E[\nu, N_e]$, Eqn. (2.27), is varied under the orbital occupation numbers n_l one finds,

$$\frac{\partial E[\nu, N_e]}{\partial n_l} = \epsilon_l, \tag{2.43}$$

which is known as Janak's theorem [41]. The fundamental aufbau-principle can be gained together with the constraints to the n_l in Eqn. (2.38). Only the lowest one-particle energies ϵ_l will be occupied.

$$n_l = 1, \qquad\qquad \epsilon_l < \epsilon_{N_e} \tag{2.44}$$

$$0 \le n_l \le 1, \qquad\qquad \epsilon_l = \epsilon_{N_e} \tag{2.45}$$

$$n_l = 0, \qquad\qquad \epsilon_l < \epsilon_{N_e} \tag{2.46}$$

The ground-state energy of the system may now be expressed via the one-particle eigenenergies ϵ_l.

$$E[\nu, N_e] = \sum_l^{occ} \epsilon_l - E_h - \int \nu_{xc}(x)\, n(x)\, dx + E_{xc}[n] \tag{2.47}$$

2.2.1.3   Local Density Approximation and more

In the following a practical expression for ν_{xc} will be given, which was missing in the previous subsection. The homogeneous electron liquid is a sufficiently simple model system for which the XC energy per particle $\epsilon_{xc} = \epsilon_{xc}^{hom}$ can be estimated with any accuracy. Kohn and Sham suggested replacing the XC energy density of the inhomogeneous system with the XC energy density of the homogeneous electron liquid. This is what in literature is called LDA [8]. The XC energy is then obtained as an integral over ϵ_{xc}^{hom} at position x and the density $n(x)$.

$$E_{xc}[n] \approx E_{xc}^{LSDA}[n] = \int \epsilon_{xc}(n(x))\, n(x)\, dx \tag{2.48}$$

$$\nu_{xc}^{LSDA}(x) = \epsilon_{xc}(n(x)) + n(x)\, \frac{\partial \epsilon_{xc}(n(x))}{n(x)} \tag{2.49}$$

The XC-potential ν_{xc} is the functional derivative of Eqn. (2.48) with respect to $n(x)$, Eqn. (2.49). The XC energy density of the homogeneous electron gas has been determined very accurately for some limiting densities $n(x)$ [7] [42] by

---

[7]Two regions are distinguished in those calculations, namely the high density limit and the low density limit.

using a quantum Monte-Carlo method. The spin dependence of $\epsilon_{xc} = \epsilon_{xc}(n, \xi)$ is included by introducing the spin polarisation $\xi(\mathbf{r}) = (n(\mathbf{r}, \uparrow) - n(\mathbf{r}, \downarrow)) / (n(\mathbf{r}, \uparrow) + n(\mathbf{r}, \downarrow))$ (LSDA). The non-spin polarised state $\epsilon_{xc}(n, \xi = 0)$ and fully-polarised state $\epsilon_{xc}(n, \xi = 1)$ were exactly calculated. The intermediate XC energy density $\epsilon_{xc}(n, \xi)$ is then interpolated between the paramagnetic ($\xi = 0$) and the saturated ferromagnetic ($\xi = 1$) cases [9]. There are currently different interpolations based on these exact quantum Monte-Carlo results [43–45]. In this thesis the parameterisation according to Perdew and Wang [45] is applied, which is presently known to be the most accurate.

$$\epsilon_{xc}(r_s, \xi) = \epsilon_x(r_s, \xi) + \epsilon_c(r_s, \xi) \tag{2.50}$$

$$\epsilon_x(r_s, \xi) = -\frac{3}{4\pi r_s}\left(\frac{9\pi}{4}\right)^{\frac{1}{3}}\frac{(1+\xi)^{\frac{4}{3}} + (1-\xi)^{\frac{4}{3}}}{2} \tag{2.51}$$

$$\epsilon_c(r_s, \xi) = \epsilon_c(r_s, 0) + \alpha_c\frac{f(\xi)}{f''(0)}\left(1 - \xi^4\right)$$
$$+ \left[\epsilon_c(r_s, 0) - \epsilon_c(r_s, 1)\right]f(\xi)\left(1 - \xi^4\right) \tag{2.52}$$

Where we used $r_s = [3/(4\pi(n(\mathbf{r}, \uparrow) + n(\mathbf{r}, \downarrow)))]^{1/3}$ as the density parameter and the spin stiffness $\alpha_c(r_s) = \partial^2\epsilon_c(r_s, \xi = 0)/\partial\xi^2$. Despite its success LSDA is well-known to overbind, and to underestimate experimental lattice parameters by about $1 - 2\%$ [46]. This problem can partly be remedied when applying the generalised gradient approximation, in which a gradient term of the density $\partial n(x)/\partial\mathbf{r}$ is included in the XC energy density $\epsilon_{xc} = \epsilon_{xc}(n(x), \partial n(x)/\partial\mathbf{r})$. In this thesis the parameterisation proposed by Perdew, Burke, and Ernzerhof [47] is used.

Both parameterisations of the XC energy used here work well for weakly correlated systems, nevertheless they are a crude approximation of the true XC energy, e.g. the theoretical calculated band gap in semi conductor is smaller than its measured value. Furthermore, the self-interaction is not compensated completely, as it would be for the true XC energy. Therefore, a self-interaction correction (SIC) is proposed, e.g. the description of the localised $4f$-electrons is improved [44, 48]. On-site-Coulomb interaction can be applied with the so-called LSDA+U method [14, 15, 49], in which an orbital dependent Coulomb interaction is added to Eqn. (2.36).

2.2.2 Relativistic DFT

The derivation of the relativistic Kohn-Sham-Dirac equation will be discussed in this section. A detailed discussion can be found in [40, 50]. In order to describe interacting relativistic electrons properly, one must adopt the formalism of quantum electrodynamics (QED). For this reason we will substitute the non-relativistic quantities with their corresponding four-covariant ones. Accordingly, the many-particle wave function $\Psi_{N_e}(\{x_k\})$ is replaced by the four-component operator-valued electron-positron field $\hat{\Psi}(x^\sigma)$ [8], in which $x^\sigma = (ct, \mathbf{r})$ and $x_\sigma = (ct, -\mathbf{r})$[9]. Interactions are described with operator-valued

---

[8]The corresponding Fock state reads $|\Psi\rangle$.
[9]Latin symbols pass through the vector components $1 - 3$, Greek symbols pass through $0 - 3$.

four-potentials. Thereby, the electrons interact with photon fields $\hat{A}^\mu(x^\sigma)$. A static external potential is added by means of $A^\mu(x^\sigma)$ (without a hat!). The Hamiltonian of interest is

$$\hat{H}_A = \int d^r \left(c : \hat{\bar{\Psi}}(-i\boldsymbol{\gamma} \cdot \boldsymbol{\nabla} + c)\hat{\Psi} : -\hat{j}^\mu \hat{A}_\mu + \right.$$
$$\left. + \frac{1}{2} : \left(\epsilon_0 \hat{\mathbf{E}}^2 + \mu_0 \hat{\mathbf{H}}^2\right) : -e\hat{j}^\mu A_\mu \right). \quad (2.53)$$

Here, it is the four-current density operator $\hat{j}^\mu = c : \hat{\bar{\Psi}}\gamma^\mu\hat{\Psi} :$, the Dirac matrices $\boldsymbol{\gamma} = (\gamma^1, \gamma^2, \gamma^3)$, the electric component $\hat{\mathbf{E}}$ and the magnetic component $\hat{\mathbf{H}}$ of the electron-electron interaction field $\hat{A}^\mu$. The dots ":" represent the normal order, so that creation- and annihilation-operators are in normal order with respect to the creation and annihilation operators of the renormalised asymptotic fields, i.e. zero external four-potential A^μ [10]. The expectation values of all observables are assumed to be stationary, i.e. $\langle\Psi|\hat{j}^\mu|\Psi\rangle = J^\mu$. Contrary to the non-relativistic procedure, only the charge Q is fixed,

$$Q = -\frac{1}{c}\int d^3r J^0(\mathbf{r}), \qquad (2.54)$$

and searching for the ground-state of the quantum field that forms the minimum of $E[A, Q]$,

$$E[A, Q] \equiv \min_\Psi \left\{ \langle\Psi|\hat{H}_A|\Psi\rangle \; \middle| \; -\frac{1}{c}\int d^3r \langle\Psi|\hat{j}^0|\Psi\rangle = Q \right\}. \qquad (2.55)$$

As in the non-relativistic case, the minimum condition is warranted by the restriction on a finite torus. Unfortunately, the quantum fields $\hat{A}^\mu$ and $\hat{j}^\mu$ have to be renormalised [51], due to an anomalous behaviour for non-zero J^μ. The result is an effective Hamiltonian $\hat{H}^{eff}_{A,Q}$ with currents split into conducted and fluctuating parts as $\hat{j}^\mu = \hat{J}^\mu + J^\mu$, which will not be discussed here. The main gain by defining such a $\hat{H}^{eff}_{A,Q}$ is that one can define with this effective Hamiltonian a new functional $E[A, Q]$ that is convex in Q for constant four-potential A^μ. Furthermore $E[A, Q]$ behaves concavely in A^μ for constant Q.

$$E[A, Q] \equiv \min_\Psi \left\{ \langle\Psi|\hat{H}^{eff}_{AQ}|\Psi\rangle \; \middle| \; \langle\Psi|\hat{J}^\mu|\Psi\rangle = 0 \right\} \qquad (2.56)$$

Analogous to the non-relativistic case, one may now define a current-density functional $H[J]$,

$$H[J] \equiv \inf_{Q \le 0} \sup_{A \in X^*} \left\{ E[A, Q] + e\int d^3r J^\mu A_\mu \right\}. \qquad (2.57)$$

---

[10]The definition of renormalised fields can be found in [51]

The Hohenberg-Kohn variational principle in its relativistic version reads:

$$E\left[A, Q\right] = \inf_{J \in X} \left\{ H\left[J\right] - e \int d^3 r J^\mu A_\mu \;\middle|\; -\frac{e}{c} \int d^3 r J^0 = Q \right\}. \quad (2.58)$$

We demand that $J^\mu \in X = \mathbf{L}^3\left(\mathcal{T}^3\right)$, and that $A^\mu \in X^* = \mathbf{L}^{\frac{3}{2}}\left(\mathcal{T}^3\right)$ on the corresponding spaces, in which the variation takes place. The same splitting as in Eqn. (2.36) leads to:

$$H\left[J\right] = T\left[J\right] - \frac{1}{2} \int d^3 r J^\mu a_\mu + E_{xc}\left[J\right]. \quad (2.59)$$

Recall that we replaced the original electron-electron photon field $\hat{A}^\mu$ with the renormalised photon field a^μ. The minimisation of (2.58) yields the most general Kohn-Sham-Dirac equation [18]:

$$\left[-ic\boldsymbol{\alpha} \cdot \boldsymbol{\nabla} + \beta m_0 c^2 - ec\beta\gamma^\mu \left(A_\mu + a_\mu + a_\mu^{xc} \right) \right] \Psi_k = \Psi_k \epsilon_k, \quad (2.60)$$

in which β and α^i are 4×4 matrices and they are defined in appendix A. The Kohn-Sham XC four-potential is defined as:

$$-ea_\mu^{xc} = \frac{\delta E_{xc}\left[J\right]}{\delta J^\mu}. \quad (2.61)$$

In order to eliminate the far ranging vector potential A_μ it is necessary to apply the Gordon decomposition [52] on the four current density J^μ. The resulting three-current density $\mathbf{J}\left(\mathbf{r}\right)$ is written as,

$$\mathbf{J}\left(\mathbf{r}\right) = \mathbf{I}\left(\mathbf{r}\right) + \frac{1}{m}\boldsymbol{\nabla} \times \mathbf{S}\left(\mathbf{r}\right) + \frac{\partial \mathbf{G}\left(\mathbf{r}\right)}{\partial t}, \quad (2.62)$$

with an orbital current density $\mathbf{I}\left(\mathbf{r}\right)$, a spin density $\mathbf{S}\left(\mathbf{r}\right)$, and a relativistic correction term $\mathbf{G}\left(\mathbf{r}\right)$, which disappears in stationary cases such as ours. The spin current density is by definition the curl of the spin density $\mathbf{S}\left(\mathbf{r}\right)$. The spin density is obtained as expectation value of the spin operator $\hat{\boldsymbol{\Sigma}}$: $\mathbf{S}\left(\mathbf{r}\right) = \frac{1}{2}\bar{\Psi}\hat{\boldsymbol{\Sigma}}\Psi$[11]. We demand that $\boldsymbol{\nabla} \cdot \mathbf{J}\left(\mathbf{r}\right) \equiv 0$, due to charge conservation. The divergence of the spin current density vanishes because $\boldsymbol{\nabla} \cdot \left(\boldsymbol{\nabla} \times \mathbf{S}\left(\mathbf{r}\right)\right) \equiv 0$ thus the orbital current density must also be divergence-free $\boldsymbol{\nabla} \cdot \mathbf{I}\left(\mathbf{r}\right) \equiv 0$. Analogous to the curl of $\mathbf{S}\left(\mathbf{r}\right)$ in (2.62), the orbital current density $\mathbf{I}\left(\mathbf{r}\right)$ is expressed as a curl of some vector field $\mathbf{L}\left(\mathbf{r}\right)$, which is called "angular momentum density". Namely, it is $\mathbf{I}\left(\mathbf{r}\right) = \frac{1}{2m}\left(\boldsymbol{\nabla} \times \mathbf{L}\left(\mathbf{r}\right)\right)$. However, the definition of an "angular momentum density" violates Heisenberg's uncertainty principle with simultaneous sharp values for position and momentum. By construction $\mathbf{L}\left(\mathbf{r}\right)$ is defined up to an arbitrary additive gradient term. A "magnetisation" density $\mathbf{M}\left(\mathbf{r}\right)$ is introduced in the following manner:

$$-e\mathbf{J}\left(\mathbf{r}\right) = \boldsymbol{\nabla} \times \mathbf{M}\left(\mathbf{r}\right) = -\frac{e}{2m}\boldsymbol{\nabla} \times \left(\mathbf{L}\left(\mathbf{r}\right) + 2\mathbf{S}\left(\mathbf{r}\right)\right). \quad (2.63)$$

---

[11] $\hat{\boldsymbol{\Sigma}} = \mathbb{1}_2 \otimes \boldsymbol{\sigma}$. $\boldsymbol{\sigma}$ are the Pauli matrices which are defined in appendix A.2.

Using the expression of the three-current density (2.63) in the variational principle (2.58) one arrives at the final Kohn-Sham-Dirac equation, which reads as

$$
\begin{aligned}
\left[-ic\boldsymbol{\alpha}\cdot\boldsymbol{\nabla} + \beta mc^2 + \nu\left(\mathbf{r}\right) + \nu^h\left(\mathbf{r}\right) + \nu^{xc}\left(\mathbf{r}\right)\right]\Psi_k\left(\mathbf{r}\right) - \\
- \mu_0\beta\int d^3r'\left(\mathbf{h}\left(\mathbf{r}'\right) + \mathbf{h}^h\left(\mathbf{r}'\right) + \mathbf{h}^{xc}\left(\mathbf{r}'\right)\right)\cdot\frac{\delta\mathbf{M}\left(\mathbf{r}'\right)}{\delta\bar{\Psi}_k\left(\mathbf{r}\right)} = \Psi_k\left(\mathbf{r}\right)\epsilon_k.
\end{aligned}
\tag{2.64}
$$

We denote $\nu\left(\mathbf{r}\right)$ as the mechanical potential, $\nu^h\left(\mathbf{r}\right)$ as the hartree potential, $\nu^{xc}\left(\mathbf{r}\right)$ as the XC potential, $\mathbf{h}\left(\mathbf{r}'\right)$ as the magnetic field, $\mathbf{h}^h\left(\mathbf{r}'\right)$ as the hartree field, and $\mathbf{h}^{xc}\left(\mathbf{r}'\right)$ as the XC field. In practise, $\mathbf{h}^h\left(\mathbf{r}'\right)$ is $2\ldots3$ orders of magnitude smaller than $\mathbf{h}^{xc}\left(\mathbf{r}'\right)$, and is thus left out in (2.64). Our final concern is the non-local character in $\delta\mathbf{M}\left(\mathbf{r}'\right)/\delta\Psi_k\left(\mathbf{r}\right)$, especially in $\delta\mathbf{L}\left(\mathbf{r}'\right)$. Hence, the remaining task is to find an appropriate expression for $\delta\mathbf{L}\left(\mathbf{r}'\right)/\delta\Psi_k\left(\mathbf{r}\right)$ [40]. A practical way doing away with the non-locality of $\delta\mathbf{M}\left(\mathbf{r}'\right)/\delta\Psi_k\left(\mathbf{r}\right)$ in $E_{xc}\left[J\right]$ is to neglect $\mathbf{L}\left(\mathbf{r}\right)$ (2.65).

$$
E_{xc}\left[J\right] = E_{xc}\left[cn, \boldsymbol{\nabla}\times\left(\mathbf{L}\left(\mathbf{r}\right) + 2\mathbf{S}\left(\mathbf{r}\right)\right)\right] \approx E_{xc}^{LSDA}\left[n, 2\mathbf{S}\left(\mathbf{r}\right)\right]
\tag{2.65}
$$

To that effect the basic equation that needs to be solved is Eqn. (2.64) making use of Eqn. (2.65). In that way full-relativistic calculations were performed in this work. Additionally, so-called scalar relativistic calculations were performed, in which the SO is missing [16]. We bear in mind that in $3d$-elements the energies of Hund's first rule are larger than those of Hund's second rule. Thus, the neglect of the orbital current density in Eqn. (2.63) seems justified when describing the total magnetisation. In contrast to systems in which the energies of Hund's first and second rule are comparable, in particular systems involving $5f$ elements [53], the validity of Eqn. (2.65) may change. Here the neglect of the orbital current density is no longer justified, and the calculated orbital magnetic moment μ_l is too small. A practical way to circumvent this problem is to introduce OPC, which will be discussed in Chapter 3.

2.3 Full Potential non-Orthogonal Local Orbital Minimum Basis Band Structure Scheme

In this thesis all calculations were done with the FPLO band structure scheme [35]. Accordingly, the main features of FPLO are presented briefly. We want to mention that in this work the FPLO versions 5, 8, and 9 were used. The version 5 is presented here. The main difference among the different version is the treatment of the basis states.

    FPLO is a full-potential scheme, which means there is no shape restriction to the potential, as in muffin-tin based methods. It is based on the LCAO [34] method, in which the Kohn-Sham orbitals (2.40) or (2.64) are projected on local atomic states $|\mathbf{R}sv\rangle$ [12]. Here, $\mathbf{R}$ denotes a Bravais vector, $\mathbf{s}$ a site vector

---

[12]The corresponding wave function is $\varphi_{\mathbf{s}v}\left(\mathbf{r}-\mathbf{R}-\mathbf{s}\right) = \langle\mathbf{r}|\mathbf{R}sv\rangle$.

in the unit cell, and υ is a multi-index, which used either the full relativistic or the non-relativistic notation [13]. These local atomic orbitals are written in terms of radial functions $\psi_{\mathbf{s}}^{\upsilon}\left(|\mathbf{r} - \mathbf{R} - \mathbf{s}|\right)$ [14] and spherical harmonics, [15].

$$\varphi_{\mathbf{s}\upsilon}\left(\mathbf{r} - \mathbf{R} - \mathbf{s}\right) = \psi_{\mathbf{s}}^{\upsilon}\left(|\mathbf{r} - \mathbf{R} - \mathbf{s}|\right)\mathcal{Y}_{\upsilon}\left(\mathbf{r} - \mathbf{R} - \mathbf{s}\right). \tag{2.66}$$

The periodic boundary conditions, Section 2.2, grant that the Bloch functions $\Phi_{\mathbf{k}n}$ are eigenfunctions of the Kohn-Sham Hamiltonian,

$$\Phi_{\mathbf{k}n} = \sum_{\mathbf{R},\,\mathbf{s},\,\upsilon} c_{\mathbf{s}\upsilon}^{\mathbf{k}n}\varphi_{\mathbf{s}\upsilon}\left(\mathbf{r} - \mathbf{R} - \mathbf{s}\right)e^{i\mathbf{k}(\mathbf{R}+\mathbf{s})}. \tag{2.67}$$

These Bloch functions are now used as an ansatz for the self-consistent Kohn-Sham problem. This leads to a matrix equation for the eigenvalue problem (2.40) or (2.64). The diagonalisation effort is reduced due to a distinction between core, semi-core, valence, and polarisation states. If the basis is too small, completeness of the basis is achieved by adding more states to the basis. The core states are assumed to already be orthogonal to each other, so the overlap between core states of distinct sites is neglected. Semi-core, valence, and polarisation states may have a non-zero overlap. Recall that the diagonalisation of a matrix scales with the cube of its size. In comparison with plane-wave based codes, which use a high number of plane waves to achieve high accuracy, this method relies on a relatively small number of basis states. The notation used in this thesis is defined as following,

$$\text{element}: \quad core \quad :: \quad semi-core \quad / \quad valence \quad + \quad polarisation. \tag{2.68}$$

All non-core orbitals are compressed by adding a confining potential, $\nu^{conf} = (\mathbf{r}/r_0)^4$, with $r_0 = (x_0 r_{\mathrm{NN}}/2)^{3/2}$ to the site-spherical average of the crystal potential. Here, r_{NN} denotes the nearest neighbour distance, and x_0 is the parameter which is optimised in every iteration step[16]. These compressed orbitals are better suited to construct the extended wave functions than more extended free atom functions.

The summation over all occupied states yields the total electron density $n\left(\mathbf{r}\right)$, which contains on-site $\mathbf{R} - \mathbf{s} = \mathbf{R}' - \mathbf{s}'$ and off-site $\mathbf{R} - \mathbf{s} \neq \mathbf{R}' - \mathbf{s}'$ terms.

---

[13] $\upsilon = (n, l, m_l)$ for the non-relativistic case, and $\upsilon = (n, \kappa, \mu)$ in the relativistic case. Where (n, l, m_l) denote the non-relativistic quantum numbers, and (n, κ, μ) the relativistic [54].

[14] The $\psi_{\mathbf{s}}^{\upsilon}\left(|\mathbf{r} - \mathbf{R} - \mathbf{s}|\right)$ are solutions of the radial Schrödinger or the radial Dirac equation for a suitable spherical potential.

[15] A definition can be found in section A.1, in the non-relativistic case $\mathcal{Y}_{\nu} = \mathcal{Y}_L$ ($L = l, m_l$) and for the relativistic situation $\mathcal{Y}_{\nu} = \chi_{\kappa\mu}$.

[16] Since FPLO6, a fixed basis is implemented. The code is faster and more accurate, but the *coherent potential approximation* (CPA) [55] is not yet available.

$$n\left(\mathbf{r}\right) \;=\; \sum_{\mathbf{k},\,n}^{occ.} \Phi_{\mathbf{k}n}^{*}\left(\mathbf{r}\right)\Phi_{\mathbf{k}n}\left(\mathbf{r}\right) \tag{2.69}$$

$$= \sum_{\mathbf{k},\,n}^{occ.} \sum_{\mathbf{R}+\mathbf{s},\,\upsilon} \sum_{\mathbf{R}'+\mathbf{s}',\,\upsilon'} \left(c_{\mathbf{s}\upsilon}^{\mathbf{k}n}\right)^{*} c_{\mathbf{s}'\upsilon'}^{\mathbf{k}n} \;\; \varphi_{\mathbf{s}\upsilon}^{*}\left(\mathbf{r}-\mathbf{R}-\mathbf{s}\right)$$

$$\varphi_{\mathbf{s}'\upsilon'}\left(\mathbf{r}-\mathbf{R}'-\mathbf{s}'\right)e^{i\mathbf{k}\left(\left(\mathbf{R}'-\mathbf{R}\right)+\left(\mathbf{s}'-\mathbf{s}\right)\right)} \tag{2.70}$$

Finally, the density and the potential are expanded in spherical harmonics at each lattice site $\mathbf{s}$.

$$n\left(\mathbf{r}\right) \;=\; \sum_{\mathbf{R}+\mathbf{s},\,\upsilon} n_{\mathbf{s}\upsilon}\left(\left|\mathbf{r}-\mathbf{R}-\mathbf{s}\right|\right)\mathcal{Y}_{\upsilon}\left(\mathbf{r}-\mathbf{R}-\mathbf{s}\right) \tag{2.71}$$

$$\nu\left(\mathbf{r}\right) \;=\; \sum_{\mathbf{R}+\mathbf{s},\,\upsilon} \nu_{\mathbf{s}\upsilon}\left(\left|\mathbf{r}-\mathbf{R}-\mathbf{s}\right|\right)\mathcal{Y}_{\upsilon}\left(\mathbf{r}-\mathbf{R}-\mathbf{s}\right) \tag{2.72}$$

The resulting total potential is obtained with these densities. FPLO is making use of Ewald's method [56] to cope with the long-range tails of the Coulomb potential. In addition, the shape function technique is used to achieve a locally finite lattice sum for the Hartree and XC potential. This shape function $f_{\mathbf{s}}$ is subject to the condition $\sum_{\mathbf{R}+\mathbf{s}} f_{\mathbf{s}}\left(\mathbf{r}-\mathbf{R}-\mathbf{s}\right) \equiv 1$. The potentials are then inserted into the Kohn-Sham equation, and this routine is iterated until convergence is reached.

The linear tetrahedron method [57], including the Blöchl correction [58], has been employed in all calculations for the k-space integrations.

2.4 Magneto-Crystalline Anisotropy Energy

The concept of MCA energy was introduced to describe magnetic effects in a phenomenological model using thermodynamic quantities. Basically, the MCA is the energy difference between two directions of the magnetisation density. A significant point is that the magnitude of the magnetisation varies little while rotating the magnetisation. The progress in a quantitative description of anisotropy energies of transition metals was very slow until the beginning of the 1990s. Due to the recent accuracy in DFT codes [17], realistic predictions can be made for those systems [59–61]. A detailed introduction into magnetic anisotropy may be found in [62].

Theoreticians started exploring phenomena about the magnetic anisotropy in the 1930s. It was van Vleck who pointed 1937 out that relativistic corrections are essential to qualitatively characterise the magnetic anisotropy while describing the magnetisation non-relativistically [63]. The two sources of MCA are the *classical dipole dipole interaction* and the *SO interaction*. For this purpose let us define the Gibbs free energy density $g\left(h,\hat{\mathbf{m}}\right)$, dependent on the external magnetic field h and on the magnetisation direction $\hat{\mathbf{m}}$. We assume constant

---

[17]Anisotropy energies often are calculated as total energy differences, thus numerical accuracy in the total energy of μeV/atom is demanded.
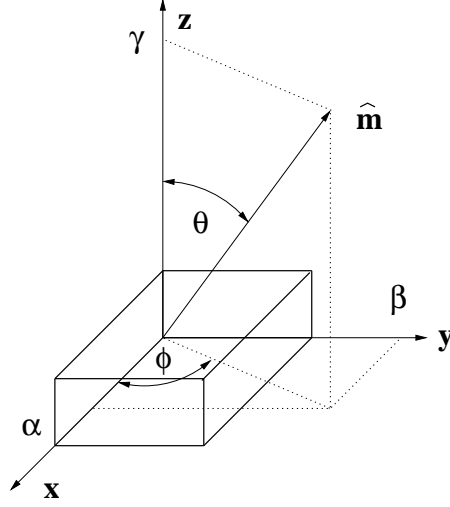
Figure 2.1: Coordinate system used.

temperature T as well as constant stress $\boldsymbol{\sigma}$[18]. Here, h denotes the external magnetic field projected in the direction of the magnetisation $\hat{\mathbf{m}}$. This energy density is split into two main contributions and a contribution, which is only dependent on the amount of magnetisation $|\hat{\mathbf{m}}|$: $g_0\left(|\hat{\mathbf{m}}|\right)$. $g_0\left(|\hat{\mathbf{m}}|\right)$ is fixed to zero in our considerations. . The *shape anisotropy*, due to dipole-dipole interaction, and the intrinsic *magneto-crystalline anisotropy*, which is dominated by the SO interaction and has dipolar contributions in higher order. In the absence of an external field,

$$g\left(\hat{\mathbf{m}}\right) \,=\, g_{shape}\left(\hat{\mathbf{m}}\right) \,+\, g_{crystal}\left(\hat{\mathbf{m}}\right) \,+\, g_0\left(|\hat{\mathbf{m}}|\right). \tag{2.73}$$

Further there are contributions arising from the volume (bulk) and from the surface; we omit the surface contribution. It has been shown that the energy density can be expanded in terms of the components $(\alpha,\,\beta,\,\gamma)$ of the magnetisation direction $\hat{\mathbf{m}}$ with respect to the crystal axes $(\mathbf{x},\,\mathbf{y},\,\mathbf{z})$ [64, 65], compare figure 2.1 [19]. For a Cartesian coordinate system we have, $(\alpha,\,\beta,\,\gamma) = (\sin\theta\cos\phi,\,\sin\theta\sin\phi,\,\cos\theta)$. Respectively for cubic, tetragonal, and hexagonal systems it is obtained,

$$\text{cubic}: \quad g_{crystal}\left(\hat{\mathbf{m}}\right) \quad = K_0 \,+\, K_1\left(\alpha^2\beta^2 \,+\, \beta^2\gamma^2 \,+\right.$$
$$\left. +\,\gamma^2\alpha^2\right) \,+\, \dots \tag{2.74}$$
$$\text{tetragonal}: \quad g_{crystal}\left(\hat{\mathbf{m}}\right) \quad = K_0 \,+\, K_1\sin^2\theta \,+\, K_2\sin^4\theta\dots \tag{2.75}$$
$$\text{hexagonal}: \quad g_{crystal}\left(\hat{\mathbf{m}}\right) \quad = K_0 \,+\, K_1\sin^2\theta \,+\, K_2\sin^4\theta\dots \tag{2.76}$$

---

[18]This thermodynamic potential g is in general also temperature and pressure dependent, but we neglect further dependencies in our discussions.

[19]The number of coefficients can be reduced due to symmetry arguments, e.g. crystal symmetry

Recall that for cubic systems the magneto-crystalline energy sets in with a 4th order term, in contrast to the hexagonal and tetragonal case, which are of 2nd order. Thus, we can expect that cubic systems have smaller magneto-crystalline energies than related tetragonal and hexagonal structures. The K_n are called *anisotropy constants* [20]. We keep in mind that the concept of "anisotropy energy" as well as "anisotropy constants" is a theory for macroscopic systems, thus predictions for small objects, such as nanoclusters or single clusters, have to be regarded with caution [66].

It turns out that in most cases of itinerant band magnetism [21] the expansion (2.74)- (2.76) can be truncated after the first non-vanishing term. As a consequence the MCA is often calculated as energy difference:

$$\triangle E_{mca}\left(\hat{\mathbf{n}}_1,\, \hat{\mathbf{n}}_2\right) = g_{crystal}\left(\hat{\mathbf{n}}_1\right) - g_{crystal}\left(\hat{\mathbf{n}}_2\right), \tag{2.77}$$

in which $\hat{\mathbf{n}}_1$ and $\hat{\mathbf{n}}_2$ denote two high-symmetry crystallographic directions. It is important to mention that the ground-state energy obtained within a DFT calculation represents the Gibbs free energy only if the magnetisation direction points along a high-symmetry crystallographic direction. Otherwise this ground-state energy is an approximation to true magnetic energy for those directions. As a result the MCA defined as (2.77) is doubtful [67] if calculated along non-high-symmetry directions.

2.5 Disorder within DFT

The FPLO code provides four distinct methods to simulate disorder, e.g. vacancies, interstitial atoms, or substitutions. The *rigid-band approximation* is the easiest one, but treats the problem crudely. The Fermi level is shifted according to the number of electrons, which are added to or removed from the system. Neither the Hamiltonian nor the wave function is changed. We skip this method to discuss disorder. The most promising scheme to describe disorder is *CPA* [68], which is also more expensive. There, an ensemble of configurations of atoms is used to describe random systems. It is a Green's function method to evaluate an average of all possible configurations. In the end a configurationally averaged single particle observable can be extracted. In this thesis the CPA will not be used to describe disorder since a relativistic version of CPA is not implemented in FPLO. In the *virtual crystal approximation* (VCA) an atom with non-integer atomic number is introduced, for which the number of valence electrons is adapted to the average number of valence electrons of that site [69, 70]. To warrant charge neutrality, the same amount of positive charge is added to the nuclei. This method is used to describe disorder in this thesis. The last possibility is to create *supercells*. The advantages of this method are that different patterns can be compared and local distortions considered. A disadvantage is that we reduce the number of configurations to a finite, and often small, number. In addition to this deficiency, supercell calculations are very time consuming, e.g. if magnetic structures are considered. Convergence

---

[20]The K_n are different for different symmetries, and have no direct physical meaning, but are commonly used to describe anisotropy.

[21]All investigated compounds are assumed to be itinerant, so a discussion about the localised model is not taken into account.

is complicated if we deal with different magnetic solutions, which are almost degenerate. Nevertheless, we treated disorder within a stochastic average of supercells with randomly distributed atoms. The exact procedure for the supercell construction will be discussed in Section 4.2.

3

Orbital Polarisation in DFT

Before discussing the details about including OPC in DFT a short recapitulation of Hund's rules is given. A significant point is that these rules describe the ground-state of atoms. However, conclusions on the corresponding ground-state in solids can be made according to these rules. Hund's rules provide the ground-state of an atomic shell [71], considering incompletely filled shells with a certain number of $2(J+1)$-fold degenerate multiplets. For not too heavy atoms the ground-state is well approximated by a Russel-Saunders state with fixed values of total angular momentum $L = \sum_i l_i$ and total spin $S = \sum_i s_i$[1]. According to Hund's rules the atomic state with the lowest energy has following properties:

Hund's rule 1. The state with largest spin moment S has lowest energy.

Hund's rule 2. The state with largest angular momentum L compatible with maximums S has lowest energy.

Hund's rule 3. S couples anti-parallel to L for less than half-filled shell, S couples parallel to L for more than half-filled shell[2].

Thus, the atomic ground-state with respect to total angular momentum L and total spin S can easily be found by applying all Hund's rules. We turn the subject now from atoms to solids. By considering the experimentally accessible magnetic quantities: the spin magnetic moment μ_s and the orbital magnetic moment μ_l, we want to discuss their description in DFT. Both quantities can be calculated as spatial integral over a certain sample volume $\mathcal{V}$ of the spin density $\mathbf{S}(\mathbf{r})$ and the "angular momentum density" $\mathbf{L}(\mathbf{r})$, respectively.

---

[1] The total momentum J for atoms can be calculated according to Hund's rules, as $J = S \mp L$.

[2] In heavy actinides the *j-j coupling* has to be considered rather than the *Russel-Saunders coupling* due to very large SO coupling, which is for the actinides is of the order of $\sim 1-2$ eV. In the actinides the OP is of comparable magnitude as the SO coupling contrary to the $3d$ and $4f$ shells. The OP energy of actinides is of the order of ~ 1 eV. Typical energy ranges of all three Hund's rules of d- and f-shells can be found in [16]

$$\mu_s = -\mu_B \int_{\mathcal{V}} d^3r\, 2\,\mathbf{S}\left(\mathbf{r}\right),$$ (3.1)

$$\mu_l = -\mu_B \int_{\mathcal{V}} d^3r\, \mathbf{L}\left(\mathbf{r}\right).$$ (3.2)

We recapitulate that on the one hand, in solids the picture of having isolated shells is not any more correct, as a direct consequence the ground-state configuration of atoms obtained with the Hund's rules is not the ground-state configuration observed in solids. On the other hand, OP has obviously been neglected in Eqn. (2.65). In particular, it was found that the SO coupling is not sufficient to describe the OP for $5f$ systems [53]. It turns out that the spin magnetic moment is for the most investigated cases well described within LSDA or GGA. Nevertheless, the description of the orbital magnetic moment is not satisfactory when applying the common approximation as discussed in Section 2.2.2, see Eqn. (2.65). For this reason additional non-local orbital-dependent potentials have to be added to the Kohn-Sham equation to properly account for Hund's second rule.

First of all, we discuss in Section 3.1 the presentation of the three Hund's rules in DFT before introducing the OPC used in this work. The following sections present two different schemes to remedy the neglect of $\mathbf{L}\left(\mathbf{r}\right)$ in Eqn. (2.65).

3.1 Hund's Rules in DFT

A brief review concerning the realisation of Hund's rules in atoms within DFT is given next. For that reason we summarise results of calculations for the SP energy, OP energy, and the SO coupling energy obtained with LSDA. In accordance with Hund's first rule the SP energy can be written as $E_{sp} \sim S\left(S - 1/2\right)$. Doing so the SP energy is fairly well approximated in DFT within LSDA as $E_{sp}^{LSDA} \approx -IS^2$ [12]. Experimentally observed SP energies are well reproduced by LSDA calculations [16]. Nevertheless bear in mind that there arises a self-interaction error for only one electron or one hole in a shell by the approximation of SP energy in LSDA. The parameter I is called Stoner parameter, typically being of the order of $0.4 - 0.7$ eV for d- and f-states.

The OP energy gain E_{op} is roughly proportional to $L\left(L - l\right)$ with $l = 2$, 3, for d- and for f-shells, respectively. The corresponding DFT expression of the OP energy can be, as introduced previously in the case of the SP energy, approximated via $E_{op}^{DFT} \approx -PL^2$, in which the coefficient P is explicitly discussed below. It was shown that E_{op}^{DFT} coincides with experimentally measured OP energies [16]. However keep in mind that by doing so a self-interaction error is also present for the OP energy for one electron or one hole per spin sub-shell, similar to the case of the SP energy.

SO coupling is described with Hund's third rule. The SO coupling energies are fairly well approximated by $E_{so} \approx \xi/2 \sum_i \langle \boldsymbol{\sigma}_i \hat{\mathbf{l}}_i \rangle$, where ξ are radial integrals called SO coupling constants[3], $\boldsymbol{\sigma}$ are the Pauli matrices[4], $\hat{\mathbf{l}}$ is the angular momentum operator, and i counts the electron in the shell. ξ was calculated for $3d$,

---

[3]The ξ can be estimated within $\xi \sim \frac{1}{c^2} \langle \frac{1}{r} \frac{\partial \nu_{eff}}{\partial r} \rangle$.

[4]see Appendix A.2

$4f$, and $5f$ atoms [16], ξ is calculated as $\xi_{3d} \sim 0.01 - 0.1$ eV, $\xi_{4f} \sim 0.1 - 0.4$ eV, and $\xi_{5f} \sim 0.2 - 0.8$ eV. Qualitative and quantitative agreement for the corresponding E_{so} was obtained between full relativistic LSDA calculations and experiments [16].

3.2 An Introduction to OPC and DFT

3.2.1 OPC Brooks

It turns out that the common approximation used in relativistic DFT by neglecting $\mathbf{L}(\mathbf{r})$ and taking only the SO coupling into account is not enough to properly describe Hund's second rule in solids. This section explains one way of getting rid of this lack in theory. Eriksson et al. [25, 72] empirically defined an expression that is intended to describe the OP energy by introducing an expression E_{opb}, which was similar by construction to the SP energy E_{sp}^{LSDA}. Doing so the OP energy $E_{opb} \sim L(L-l)$ is approximated in a mean field manner scaling quadratic in the total angular momentum $L_s = <\hat{\mathbf{L}}_s>$ of a spin sub-shell s. The expectation value of the total angular momentum operator $<\hat{\mathbf{L}}_s>$ is to be taken over the Kohn-Sham-Dirac states. In order to calculate L_s we expanded the Kohn-Sham-Dirac states on appropriate chosen atomic shell angular momentum states. By the reason of assuming a collinear situation, the total angular momentum is then replaced by the z-component of the atomic orbital magnetic moment $M_{ls} = \sum_m \langle m \hat{P}_{ms} \rangle$, where $\hat{P}_{ms}$ is a projector onto the atomic shell orbital with electron spin s and orbital quantum number m. The final expression for the OP energy E_{opb} is given by Eqn. (3.3). The corresponding potential $\nu_{opb,s}$, which needs not to be the same for the two spin channels, is deduced as functional derivative of E_{opb} with respect to the Kohn-Sham-Dirac states $\overline{\Psi}_k$,

$$E_{opb} = -\frac{1}{2}\sum_s B_s M_{ls}^2, \tag{3.3}$$

$$\nu_{opb,s} = \frac{\delta E_{opb}}{\delta \overline{\Psi}_k(\mathbf{r}')} = -B_s \hat{P}_{ms} M_{ls} m. \tag{3.4}$$

The eigenvalue shift caused by the m dependent potential ν_{opb} lifts the orbital degeneracy of a shell l into $(2l + 1)$ levels, if the atomic total angular momentum M_{ls} of the shell is nonzero[5]. The proportionality factor B is the Racah parameter[6]. The Racah parameter is accessible through the so-called Slater integrals F^l [73]. They are calculated as radial integral of radial atomic wave functions $R_{n,l,s}(r)$, where n is the principle quantum number of an atomic shell. We apply the following definition: $r_< = \min(r, r')$ and $r_> = \max(r, r')$.

---

[5]OPC will enhance the OP, but it will not break the symmetry.
[6]In the case of f-shells, the notation will be E^3.

$$B_s = \frac{1}{441}\left(9F_s^2 - 5F_s^4\right) \tag{3.5}$$

$$E_s^3 = \frac{1}{3}\left(\frac{5}{225}F_s^2 + \frac{6}{1089}F_s^4 - \frac{91}{7361.64}F_s^6\right) \tag{3.6}$$

$$F_s^{n,l} = \int\int dr\,dr'\,\left(rR_{n,l,s}\left(r\right)\right)^2 \frac{r_<^l}{r_>^{l+1}}\left(r'R_{n,l,s}\left(r'\right)\right)^2 \tag{3.7}$$

It should be noticed that the Racah parameter depends on the choice of the orbitals. In order to test the dependence of the Racah parameter on the chosen orbitals, three different SR calculations each time using different orbitals were performed. At first, self-consistent bulk DFT calculations using FPLO9.00-35 were applied which shall simulate the atom in a proper chemical environment, see Appendix B for the chosen input parameters. The results obtained for the atom in the bulk using FPLO were compared with calculations for a single free atom and for a single free ion. For that purpose the program DIRAC9.00-35 was used. We solved the Kohn-Sham-Dirac equation by assuming 2^+-ions (d-shells) and 3^+-ions (f-shells), in the latter case. The main difference between these two calculations for free atoms is the contraction of the non-core states in FPLO. The Racah parameter was accessible for the $5f$ shell only up to Uranium when calculating self-consistently using FPLO.

Figure 3.1 shows the results for the three different basis sets used. As a conclusion it is seen that, if orbitals are taken from a free atom calculation instead of the free ion calculation, the Racah parameter was lowered by about 7%, 8%, 10% ($3d$, $4d$, and $5d$-shells) or 9%, 6% ($4f$, and $5f$-shells). Furthermore, the bulk DFT calculations yielded Racah parameters being mostly located in between those Racah parameters obtained from atomic and ionic calculations (except for the $4f$ shell). However, the bulk parameters were much closer to the atomic parameters than to the ionic parameters. We conclude that calculations assuming 2^+-ions (d-shells) and 3^+-ions (f-shells) describe bulk properties rather well than atomic calculations. However, ionic calculations were used in the next section by reason of comparability to the previous work [74]. The obtained Racah parameters for d- and f-shells can be found in Table 3.2.

In the applications described in Chapters 4 and 5 the Racah parameter was calculated at each iteration step by using optimised atomic orbitals evaluated in the crystal potential of the system.

3.2.2 OPC Eschrig

The semi-empirical ansatz in Section 3.2.1 was introduced ad hoc. Many attempts were done to explain the proper inclusion of OP and the L^2 shape in Eqn. (3.3), e.g. see [26]. In this thesis we will follow the idea given in [74], in which a mathematical justification for the L^2 shape of E_{opb} was discussed. For further reading we refer to [75]. The authors defined the OP energy as difference of an orbitally polarised ground-state which is obtained by anisotropic full-potential calculations and the energy of an orbitally unpolarised (meaning $M_l = 0$) and spherically averaged reference state. As in the previous investigations the main interest related to OP is focussed only on contributions of zeroth order in $1/c$. Hence, the OPC are considered only in the Russel-Saunders

(a) d-shell
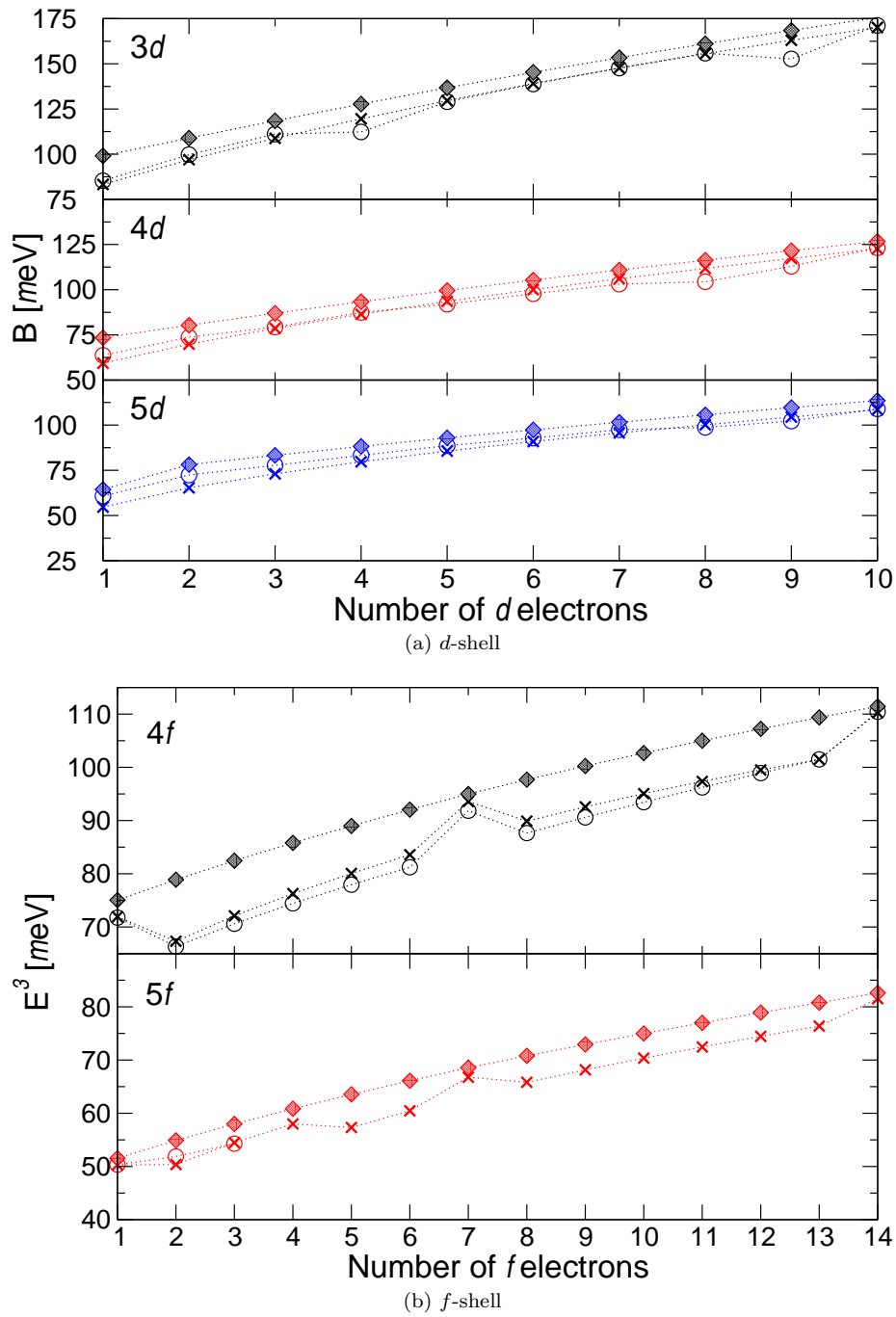
(b) f-shell

Figure 3.1: The typical energy range of Racah parameters [16] for d- and f-shells obtained using bulk calculations, atomic calculations, and ionic calculations. Isolated 2^+-ions and 3^+-ions were assumed in the latter case. The following notation is used: $\bigcirc\cdots\bigcirc$ - bulk calculation, $\times\cdots\times$ - atomic calculation, and $\diamond\cdots\diamond$ - ionic calculation. Different colours are used in order to distinguish the different shells.

limit. In order to account for a reasonable atomic configuration in a chemical bond, atomic calculations would be a suitable choice, as seen in the previous subsection. However by the reason of comparability with previous studies ionic calculations assuming 2^+-ions (d-shells) and 3^+-ions (f-shells) were performed. We applied *non-relativistic* (NR) and additional *scalar relativistic* (SR) ionic calculations (discussion below) to obtain the OP energies. It turns out that the final expression for the OP energy is split into a sum of three leading contributions, originating from exchange effects, correlation effects, and a *double-counting* (DC) term. The three terms are going to be discussed in more detail next.

We consider OP as a direct consequence of exchange interaction by calculating ground-state HF energies. For that reason HF energies of orbitally polarised and orbitally non-polarised ground-states were compared. The HF OP energy is defined as $E_{op}^{hf} = E^{hf} - E_{l=0}^{hf}$. In that sense, OP can be understood as a contribution of the asphericity of the charge density of an open shell. The final expression used in our calculations for a given spin sub-shell with N_s electrons is [76, 77]:

$$
E_{op}^{hf,l} = \sum_{k=1}^{l} F^{2k} \bigg(\frac{N_s(N_s - 1)}{2} \bar{a}_k^l +
$$
$$
\sum_{m_l,m_{l'}} \frac{2\pi}{(2k+1)} \Big((Y_{lm_l}|Y_{2k,0}|Y_{lm_l})(Y_{lm_{l'}}|Y_{2k,0}|Y_{lm_{l'}}) -
$$
$$
(-1)^{m_l - m_l'} (Y_{lm_l}|Y_{2k,m_l - m_l'}|Y_{lm_{l'}})(Y_{lm_{l'}}|Y_{2k,m_l' - m_l}|Y_{lm_l}) \Big) \bigg), \quad (3.8)
$$

where $(Y_{l_1 m_{l_1}}|Y_{l_2,m_{l_2}}|Y_{l_3 m_{l_3}})$ are the Gaunt coefficients [78] and F^{2k} are the Slater integrals which have already been defined in Eqn. (3.7). The Slater integrals were obtained using either the radial part of NR local orbitals or the radial part of SR local orbitals, whereas for the spherical part only the expression as shown in Eqn. (3.8) was used. In that sense, either a NR or a SR $E_{op}^{hf,l}$ was defined. The coefficients $\bar{a}_k^l$ for the d- and f-shells are tabulated in Appendix A.2.

The second important contribution to OP is attributed to correlation [74, 75]. In order to account for OP caused from orbital correlation effects, one has to use the local XC field $\mathbf{h}^{xc}(\mathbf{r})$ from Eqn. (2.64). Let us for the moment neglect the exchange part of this local field, and investigate OP based on correlations effects: $\mathbf{h}^{xc}(\mathbf{r}) = \mathbf{h}^x(\mathbf{r}) + \mathbf{h}^c(\mathbf{r})$. A further approximation in the sense of CDFT is a splitting of the correlation field $\mathbf{h}^c(\mathbf{r})$ into a spin correlation field $\mathbf{h}^{c,s}(\mathbf{r})$ and an orbital correlation field $\mathbf{h}^{c,l}(\mathbf{r})$. We consider OP generated by $\mathbf{h}^{c,l}(\mathbf{r})$.

$$
\mathbf{h}_{lsda}^{c,s}(\mathbf{r}) = F(\rho(\mathbf{r})) \, 2\mathbf{S}(\mathbf{r}) \tag{3.9}
$$
$$
\mathbf{h}_{lsda}^{c,l}(\mathbf{r}) = F(\rho(\mathbf{r})) \, \mathbf{L}(\mathbf{r}) \tag{3.10}
$$
$$
\mathbf{h}^{c,l} = \mathbf{h}_{lsda}^{c,l} - \mathbf{h}_{lsda}^{c,s} \frac{(\mathbf{S}(\mathbf{r})|F|\mathbf{L}(\mathbf{r}))_{lsda}}{(\mathbf{S}(\mathbf{r})|F|\mathbf{S}(\mathbf{r}))_{lsda}}. \tag{3.11}
$$

The function $F(\rho)$ was assumed to point in z-direction also using the collinear approximation. $F(\rho)$ were chosen as $F(\rho) = 2(\epsilon_c(\rho, 1) - \epsilon_c(\rho, 0))/\rho$. The von Barth-Hedin spin polarisation function $f(\xi)$ [9] was approximated as $f(\xi) = 0.855 \cdot \xi^2$. We remark that the last expression fits the true spin polarisation function only for $|\xi| \leq 0.4$ (2 % accuracy in the relevant range). However, the largest observed spin polarisations in condensed matter for atoms are well below 0.5 leading to the conclusion that the last approximation should be well justified. By choosing a proper symmetric gauge for the vector potential $\mathbf{A}(\rho, \phi, z) = \mathbf{e}_\phi A(\rho, z)$ and projecting the Kohn-Sham-Dirac orbitals Ψ_k onto the local basis functions $\phi_{ms} \sim e^{im\phi}$,[7] one derives the expression for $L(\mathbf{r})$ used in this work, Eqn. (3.12). The orbital correlation energy to the OP energy $E_{op}^{c,l}$ was then written for this special choice of the vector field $L(\mathbf{r})$ in leading order [75]:[8]

$$L(\mathbf{r}', z) = 2\sum_k n_k \int_{\rho'}^{\infty} d\rho'' \Big(\sum_{ms} \frac{m}{\rho''} |\phi_{ms}(\mathbf{r}'')\langle\phi_{ms}|\Psi_k\rangle|^2$$
$$+ A(\mathbf{r}'')\overline{\Psi}_k(\mathbf{r}'')\Psi_k(\mathbf{r}'')\Big) \tag{3.12}$$

$$E_{op}^{c,l} = -\frac{\mu_B}{2}\int d^3 r h^{c,l}(\mathbf{r}) L(\mathbf{r}, z). \tag{3.13}$$

A DC correction has to be introduced by the reason that OP is already present in ν^h and ν^{xc}, compare Eqn. (2.64). For that reason self-consistent LSDA ground-state calculations for isolated ions with integer orbital occupation numbers and spherical potential were applied to evaluate Kohn-Sham orbitals. By using the Kohn-Sham orbitals we constructed all non-spherical configurations for all admissible values L with maximum S. The corresponding energy was calculated in a perturbative (single step) treatment. The OP energy of the non-spherical configuration (Hund's rule state: $\nu_{h,xc}^{hund,l}$) was obtained by subtracting the average energy for all admissible configurations $\binom{l}{N_s}$ of a spin sub-shell l occupied with N_s electrons, see Eqn. (3.14). The OP already included in LSDA $E_{op}^{lsda,dc}$ was estimated as energy difference, see Eqn. (3.15).

$$\langle\bar{\nu}_{h,xc}^l\rangle = \frac{1}{\binom{l}{N_s}}\sum_{i=0}^{\binom{l}{N_s}}\langle\nu_{h,xc}^i\rangle \tag{3.14}$$

$$E_{op}^{lsda,dc} = \langle\nu_h^{hund,l}\rangle - \langle\bar{\nu}_h^l+\rangle + \langle\nu_{xc}^{hund,l}\rangle - \langle\bar{\nu}_{xc}^l\rangle \tag{3.15}$$

Here, ν_h^i and ν_{xc}^i denote the Hartree- and XC-potential for the actual configuration. The DC expression (3.15) calculated also for both, NR and SR local orbitals, respectively. The final expression for the OP energy used in this work is written in the following manner:

---

[7]Projection is done either onto local NR orbitals or local SR orbitals.
[8]The orbital correlation field $\mathbf{h}^{c,l}(\mathbf{r})$ was calculated in the collinear approximation ($\mathbf{h} = \mathbf{e_z}h$, $\mathbf{S} = \mathbf{e_z}S$, $\mathbf{L} = \mathbf{e_z}L$) using LSDA.

$$
\begin{aligned}
E_{opxc} &= E_{op}^{hf} + E_{op}^{c,l} - E_{op}^{lsda,dc}, & (3.16) \\
E_{opx} &= E_{op}^{hf} - E_{op}^{lsda,dc}. & (3.17) \\
& & (3.18)
\end{aligned}
$$

The OP energy including correlation effects, Eqn. (3.16), will be called E_{opxc}, the expression in which $E_{op}^{c,l}$ is explicitly excluded, Eqn. (3.17), is called E_{opx}. The last scheme may be seen as an exchange-only variant of this particular OPC scheme. This ansatz was motivated by the fact that the correlation contribution to OP is not well-known.

As next we discuss the obtained OP energies, see Eqn. (3.3) and Eqns. (3.16, 3.17). Further we will analyse the different contribution and their individual weight. Figures 3.2 and 3.3 display numerical results of the OP energies calculated using NR and SR orbitals, respectively. We recognised that the shape and the amount of $E_{opxc,opx}$ and E_{opb} was very similar. The last statement was substantiated by the reason that OP apparently is mainly based on exchange effects. Our results showed that E_{op}^{hf} yielded the largest amount among all contributions to $E_{opxc,opx}$. Nevertheless, minor differences were found between the distinct OPC schemes. As opposed to E_{op}^{hf}, non-vanishing contributions at a band filling of 1, $2l$, $2l + 2$, and $4l + 1$ developed for E_{opb}, E_{opxc}, and E_{opx}. Non-vanishing energies for one hole or electron per spin sub-shell are physically not correct and are due to self-interaction. The self-interaction error for E_{opxc} is driven by $E_{op}^{c,l}$ and partly remedied by $E_{op}^{lsda,dc}$. If $E_{op}^{c,l}$ is not considered as for E_{opx}, the self-interaction error is caused solely by $E_{op}^{lsda,dc}$.

We proceed with comparing the OP energies on the one hand obtained with local NR orbitals and on the other hand obtained with local SR orbitals. By taking the average deviation per shell between OP energies obtained either by using local NR orbitals or using local SR orbitals, we found: $0.26\,\%$, $0.68\,\%$, $3.42\,\%$, $2.80\,\%$, and $4.22\,\%$ for E_{opxc} ($3d$, $4d$, $5d$, $4f$, and $5f$-shell, respectively). In the same way we got for E_{opx} an average deviation per shell of: $0.32\,\%$, $0.08\,\%$, $2.06\,\%$, $3.90\,\%$, and $7.06\,\%$. As seen previously, we observed the largest differences in the f-shells due to relativistic effects.

The obtained $E_{opxc,opc}$ will be interpolated as in Eqns. (3.19, 3.20) presented. The coefficients P_i^l are parameterised as following $P_i^l\,(N_s) = p_i^l\,N_s$ $((2l + 1) - N_s)\,/\,2$.[9] Projection of the Kohn-Sham states Ψ_k onto NR or SR local ionic orbitals ϕ_{ms} was applied to evaluate the electron number N_s and the ionic orbital moment M_{ls},

$$
\begin{aligned}
E_{opxc}^{fit} &= -\frac{1}{2} \sum_s P_{opxc}\,(N_s)\,M_{l,s}^2, & (3.19) \\[2mm]
E_{opx}^{fit} &= -\frac{1}{2} \sum_s P_{opx}\,(N_s)\,M_{l,s}^2, & (3.20) \\[2mm]
N_s &= \sum_k n_k \sum_m |\langle \Psi_k | \phi_{ms} \rangle|^2, & (3.21) \\[2mm]
M_{ls} &= \sum_k n_k \sum_m \langle \Psi_k | \phi_{ms} \rangle m \langle \phi_{ms} | \Psi_k \rangle. & (3.22)
\end{aligned}
$$

---

[9]Here, i stands either for *opxc* or *opx*.

(a) *d*-shells (NR)

(b) *f*-shells (NR)
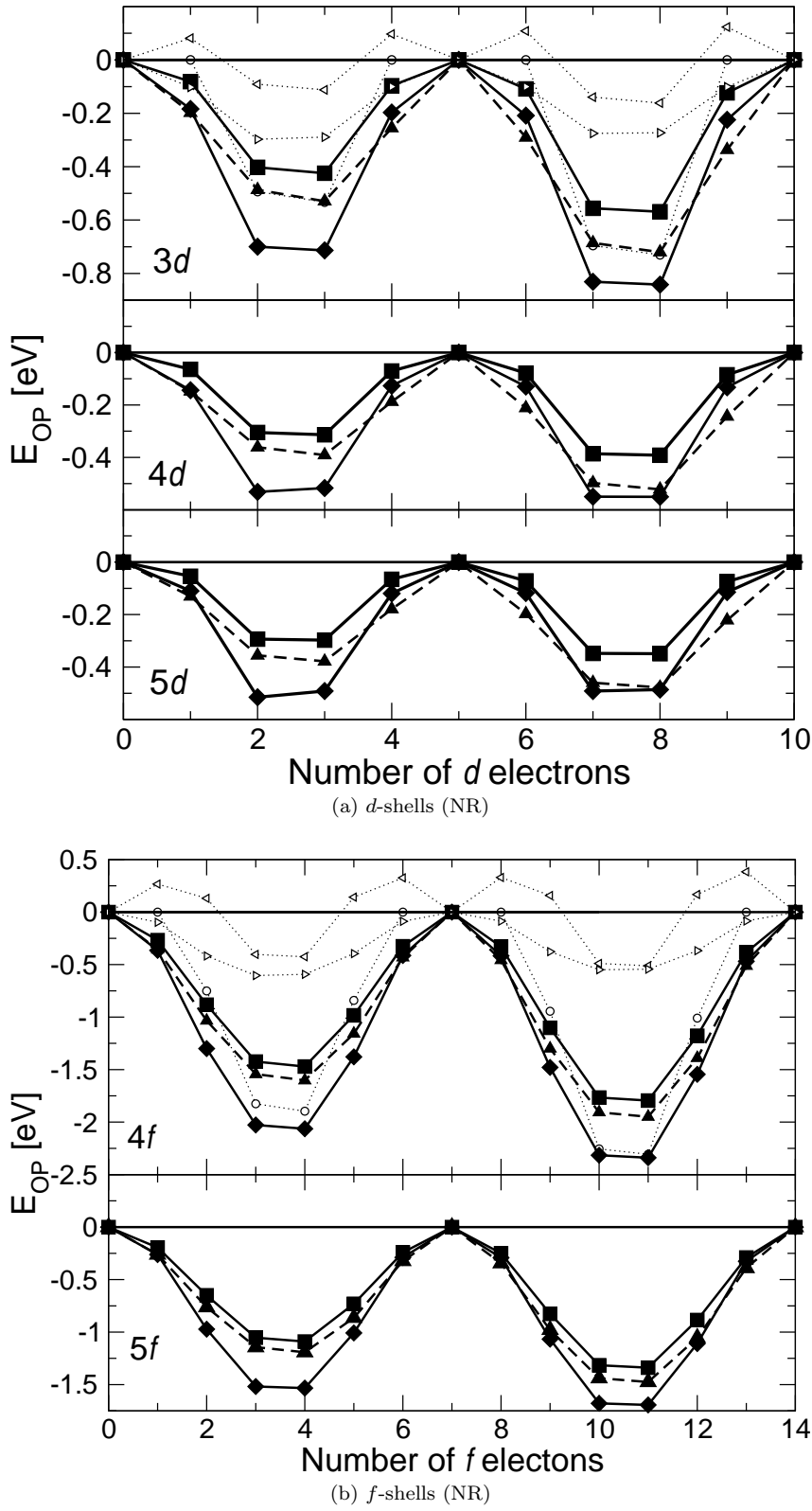
Figure 3.2: Numerical Results for OP energies by using local NR orbitals. Notation as following: ◁··◁ - $E_{op}^{c,l}$, ○··○ - E_{op}^{hf}, ▷··▷ - $E_{op}^{lsda,dc}$, ▲--▲ - E_{opb}, ◆——◆ - E_{opxc}, or ■——■ - E_{opx}. The energies are given in eV.

(a) d-shells (SR)

(b) f-shells (SR)
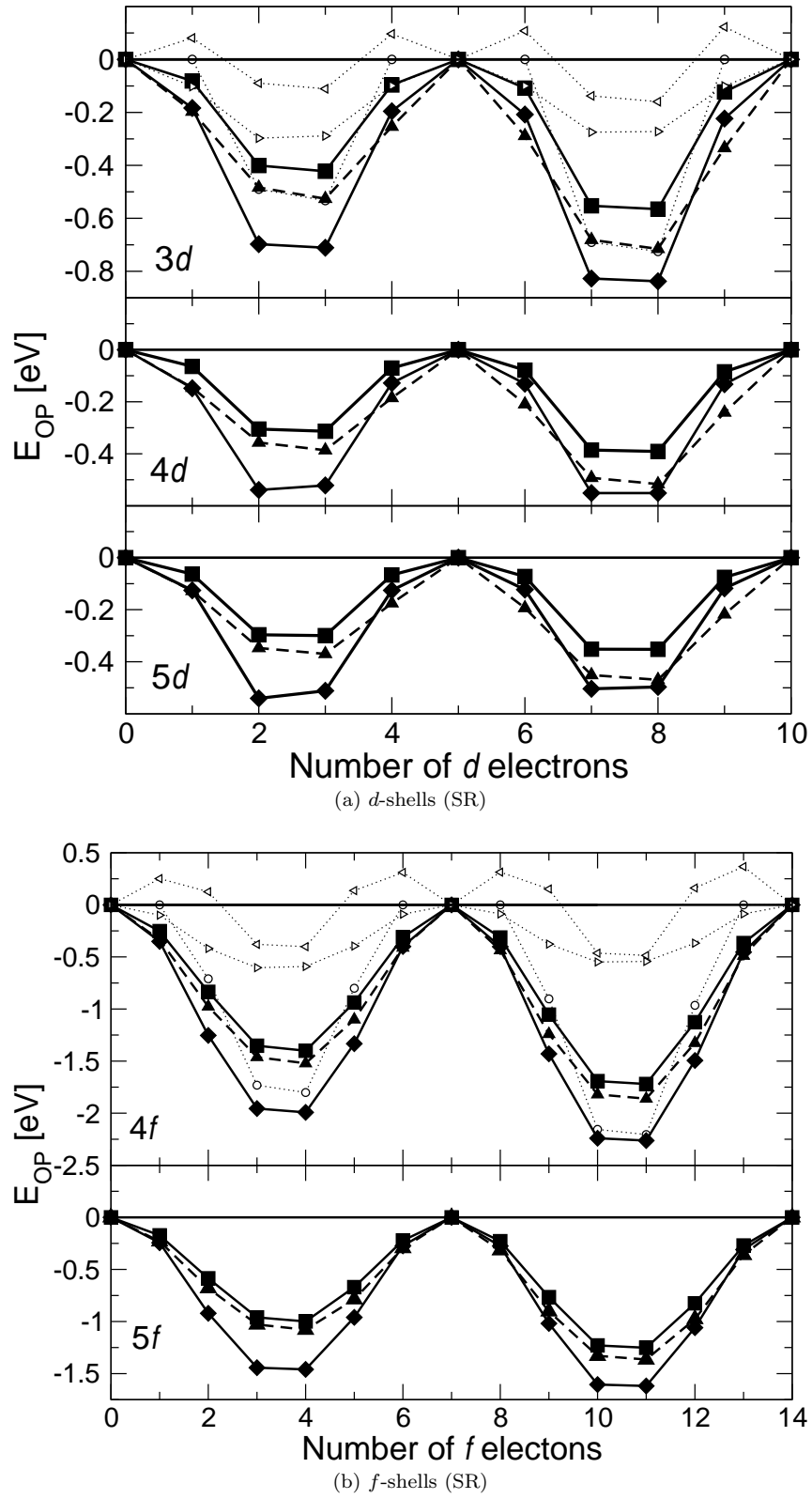
Figure 3.3: Numerical results for OP energies by using local SR orbitals. The same notation as in Figure 3.2 is applied.

(a) d-shell
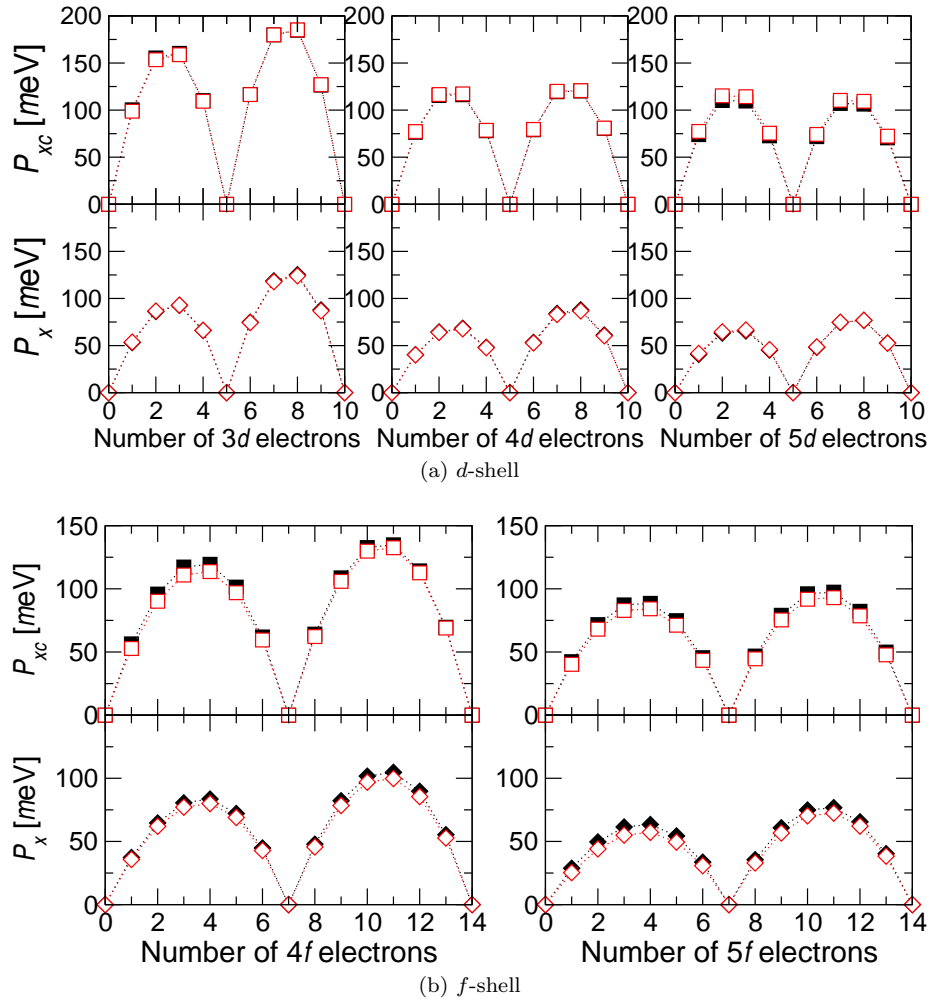
(b) f-shell

Figure 3.4: Energy range of the P_{xc} coefficients (squares) and the P_x coefficients (diamonds) for d- and f-shells calculated for corresponding 2^+-ions and 3^+-ions. The coefficients P_i were obtained by either taking local NR orbitals (■··■ , or ◆··◆) or taking local SR orbitals (□··□ , or ◇··◇), see text. The energies are given meV.

Table 3.1: Average deviation per shell l for the Racah parameters, the P_i^l coefficients, and the p_i^l coefficients, respectively. The deviation was obtained using NR and SR orbitals and is presented in percentage: $\Delta f = 1 - (f_{sr}/f_{nr})$.

| Shell	ΔB [%]	ΔP_{xc}^l [%]	ΔP_x^l [%]	Δp_{xc}^l [%]	Δp_x^l [%]
$3d$	0.62	0.48	0.50	0.76	0.79
$4d$	1.16	0.44	0.82	0.60	1.11
$5d$	2.27	2.56	1.52	3.51	1.15
$4f$	5.11	2.95	3.75	3.73	4.68
$5f$	9.73	3.95	7.05	4.95	8.90

Figure 3.4 presents the resulting coefficients P_i^l. By construction the coefficients P_i^l are zero for $N = 0$, $2l$, and $2(2l + 1)$. In addition it is seen that the coefficients P_i^l have their maximum at a band filling of $1/4$ and $3/4$. When considering the d shells (Figure 3.4a) we observed no evident difference between the coefficients obtained for the NR and the SR orbitals. As opposed for the f-shells, see Figure 3.4b. Here, a significant reduction of the coefficients either obtained with the SR orbitals or obtained with the NR orbitals is recognised.

Table 3.1 presents the average deviation per shell of the obtained coefficients between both orbitals used, for the Racah parameters, P_i^l, and p_i^l respectively. Firstly, we recognised that the most pronounced deviation is obtained for $5f$ orbitals. Secondly, the deviation found for the Racah parameters was of comparable amount as the deviation found for the parameters P_x^l and p_x^l. Finally, the deviation obtained for the coefficients P_{xc}^l and the coefficients p_{xc}^l was substantially lower than for the other coefficients.

We constructed the coefficients p_i^l in such a way, that they showed a linear dependence on the nuclear charge Z, see Figure 3.5. Consequently, a similar behaviour as compared to the Racah parameters is observed when going through a shell. We note that our chosen shape of the parameterisation differs from the OPB parameterisation [25, 72] in the N_s dependence of P_i^l. This choice yielded a *root mean square* (RMS) deviation between the calculated E_i, see Eqns. (3.16, 3.17), and the fitted $E_{opxc,\,opx}^{fit}$, see Eqns. (3.19, 3.20), of only about 5% for one particular shell l and scheme i, see Table 3.2.

By comparing the coefficients $P_{opxc,\,opx}$ it was found that $P_{opxc}^l \geq P_{opx}^l$. The last statement is caused by rather larger E_{opxc} than E_{opx}. We conjecture that the correlation contribution to OPC will be overestimated by this approach. As opposed to the Racah parameters, which are re-calculated in each iteration step (see discussion in Section 3.2.1), the parameters given in Table 3.2 are used in the self-consistent cycle in order to reduce the unavoidable basis set dependence.

Numerical implementation was done for the coefficients p_i^l, for NR or SR case, respectively. OP arises as a consequence of SO coupling, which is a relativistic effect. This fact calls for a full-relativistic treatment of a magnetic ion during the whole self-consistent cycle. This is done by retaining the NR or SR results for E_i^{fit} from Eqns. (3.19, 3.20), but replace the projector by a full-relativistic one. Hence, now the Kohn-Sham-Dirac orbitals Ψ_k are bispinors. N_s and M_{ls} are now to be obtained as:

(a) d-shell

(b) f-shell

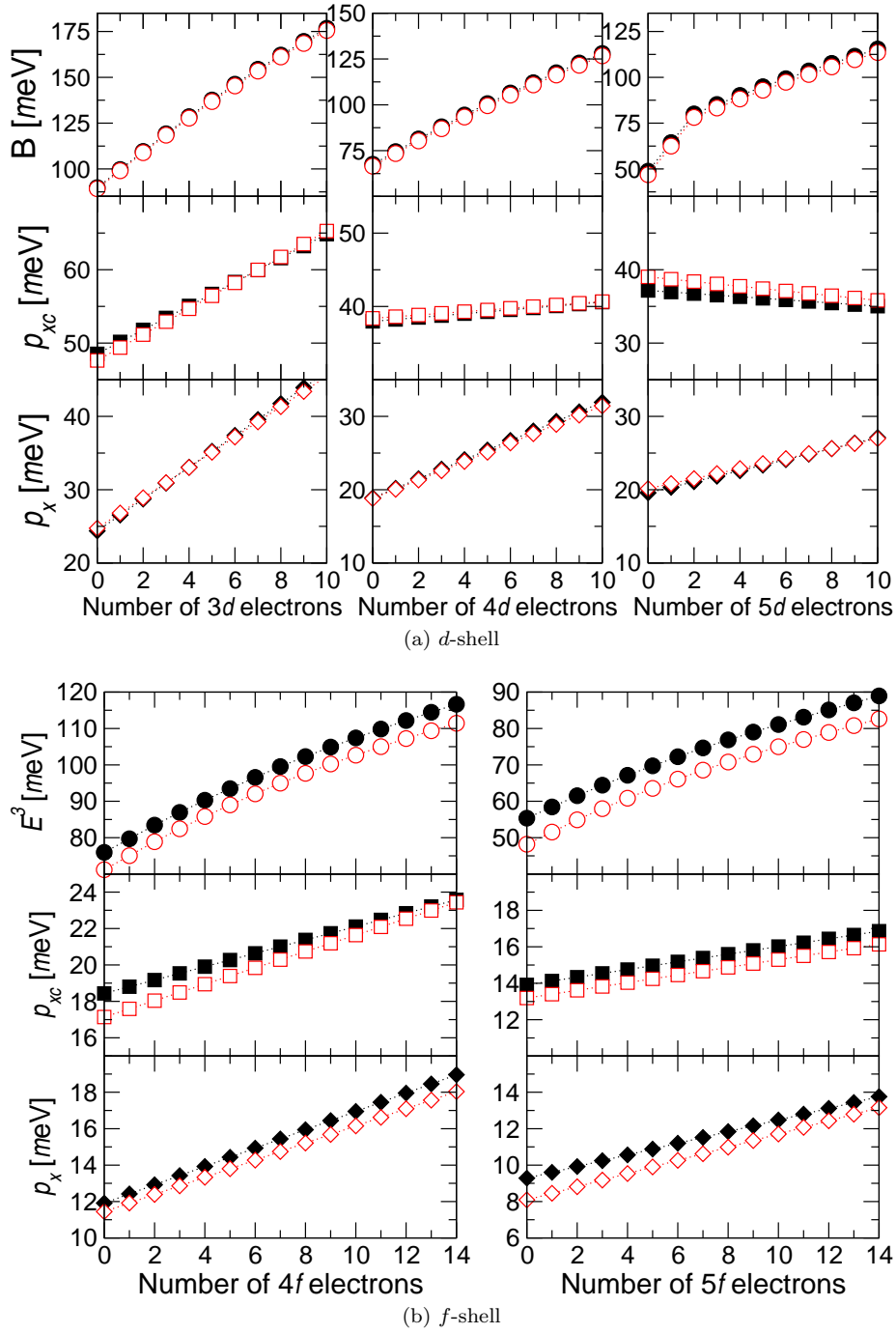Figure 3.5: Energy range of the Racah parameters [16] (circles), the p_{xc} coefficients (squares), and the p_x coefficients (diamonds) for d- and f-shells calculated for corresponding 2^+-ions and 3^+-ions. The results were obtained by using either local NR orbitals (●···●, ■···■, or ◆···◆) or using local SR orbitals (○···○, □···□, or ◇···◇), see text. The energies are given in meV.

$$N_s = \sum_{k\mu\nu} n_k \langle \Psi_k | \phi_\mu \rangle \tag{3.23}$$

$$\langle \phi_\mu | (1 + s\beta s_z) | \phi_\nu \rangle \langle \phi_\nu | \Psi_k \rangle / 2, \tag{3.24}$$

$$M_{ls} = \sum_{k\mu\nu} n_k \langle \Psi_k | \phi_\mu \rangle \tag{3.25}$$

$$\langle \phi_\mu | (1 + s\beta s_z) \hat{l}_z | \phi_\nu \rangle \langle \phi_\nu | \Psi_k \rangle / 2, \tag{3.26}$$

where ϕ_ν, ϕ_μ denote suitable defined orthonormal local bispinors of the magnetic ion shells with relativistic quantum numbers ν, μ. $(1 + s\beta s_z)$ will project on the electron state with spin s, with $s = \pm 1$, s_z is the z-component of the spin density matrix, and $\hat{l}_z$ is the orbital angular momentum operator related to the nuclear position of the magnetic ion.

Table 3.2: Energy range of the Racah parameters [16], $P_{xc,x}$ parameters, $p_{xc,x}$ parameters, and respective RMS deviation for d- and f-shells calculated for corresponding 2^+-ions and 3^+-ions. The RMS is taken for a certain shell nl between the calculated E_i and the fitted E_i^{fit} (see text). Values listed in black are derived using NR local orbitals, values tabulated in red are derived using SR local orbitals. All energies are given in meV.

Shell	B	P_{xc}^l	rms_{xc}^l	P_x^l	rms_x^l
3d	$90 - 177$	$100.3 - 184.8$	16	$53.1 - 125.3$	25
	$89 - 176$	$99.8 - 185.2$	16	$53.6 - 124.0$	25
4d	$68 - 128$	$76.5 - 120.2$	17	$40.4 - 87.9$	18
	$67 - 127$	$77.2 - 120.6$	17	$40.1 - 86.7$	18
5d	$49 - 115$	$70.5 - 110.2$	19	$40.7 - 76.8$	17
	$47 - 114$	$72.3 - 115.2$	18	$41.7 - 76.8$	16
4f	$76 - 117$	$56.4 - 132.6$	100	$37.3 - 104.7$	78
	$71 - 111$	$52.8 - 132.5$	98	$35.8 - 99.7$	73
5f	$55 - 89$	$42.4 - 97.4$	66	$18.8 - 76.8$	59
	$48 - 83$	$40.2 - 93.0$	62	$25.4 - 72.4$	53

Finally, the resulting OP potential entering the Kohn-Sham-Dirac equation is shortly discussed. The Kohn-Sham-Dirac orbitals were expanded into a non-orthogonal basis for the whole arrangement of ions. As a result a basis overlap matrix appears. In order to account for a local ansatz, the projection onto the local orbitals ϕ_μ, ϕ_ν is defined with respect to the contragredient basis. Technical details can be found in [75]. As can be seen, the overlap matrix drops out from the final expression (3.27). The corresponding potentials entering the Kohn-Sham-Dirac equation were obtained as functional derivative with respect to the Kohn-Sham-Dirac states $\overline{\Psi}_k$.

$$
\begin{aligned}
\nu_{i,\,s} \;&=\; \frac{\delta\, E_i}{\delta\, \overline{\Psi}_k\,(\mathbf{r}')} \\[2ex]
&=\; -\sum_{\mu,\,\nu} |\phi_\mu\rangle \left(P_i\,(N_s)\, M_{l\,s}\langle\phi_\mu \left|\hat{l}_z\right| \phi_\nu\rangle + \right. \\[2ex]
&\qquad \left. M_{l\,s}^2\, \frac{\delta\, P_i\,(N_s)}{\delta\, \overline{\Psi}_k\,(\mathbf{r}')}\delta_{\mu\,\nu} \right) \langle\phi_\nu|
\end{aligned}
\tag{3.27}
$$

In summary, three different OPC schemes were presented in this chapter, which differ mainly in the definition of their coefficients (B - OPB, P_{xc} - OPXC, and P_x - OPX). The OP energies were numerically studied by using either or local NR orbitals or local SR orbitals. All obtained parameters were implemented in the FPLO code. In the following chapters these OPC schemes will be applied on several $3d$ and $5f$ compounds, having a closer look on their magnetic ground-state properties.

4

Transition Metals

This chapter begins with a discussion of magnetic moments and MCA energies $\triangle E_{mca}$ of Fe, Co, and Ni. Their magnetic moments have been theoretically reproduced already close to experiments [79]. However, the evaluation of their MCA energies is problematic. Nowadays the MCA is calculated as total energy difference, keep in mind that such calculations require an accuracy of about $\sim 10^{-7}\,eV$[1] (with a fixed structure). At the same time the total energy is of the order $10^5\,eV/atom$ demanding high precision and high accuracy on the numerical calculations. In the last 15 years a qualitatively correct description between experiment and simulations could be achieved, nevertheless the calculated values scatter by usually a factor of 2. Even nowadays usual calculations can not reproduce the correctly measured sign of the MCA for Ni (FCC). The adjacent discussion in Section 4.1 shows the influence of different methods to calculate the MCA using DFT and results available in the literature are compared.

In Section 4.2 we turn the focus on the binary $Fe_{1-x}Co_x$ alloys. These alloys are interesting due to their application in computer storage devices. Published results of calculations using the FP-LMTO method [80] analysed the magnetic properties for certain tetragonal distortions and for certain Co concentrations while assuming constant volume [81]. The authors demonstrated that a perturbative treatment of the SO interaction leads to an inverse dependency of the MCA on the energy difference between the occupied and the unoccupied states. They clearly showed that a huge MCA is found for certain composition x and certain tetragonal distortion [82, 83]. Nevertheless, volume relaxation obviously was neglected in their calculations. However, it is present in epitaxial grown layers. Secondly, disorder was considered only by using the VCA method. Our calculations simulate these tetragonal distortions by making use of the so-called *epitaxial Bain path* (EBP) [84] which accounts for a geometrical relaxation of the particular structure of these alloys. Additionally, disorder was described using two different methods, firstly the VCA was applied in order to control the previously obtained results, and secondly a stochastic average of supercells with randomly distributed atoms was taken into account. Finally, a comparison of the disordered phases with the ordered structures of $L1_0$-type and $L1_2$-type phases revealed the impact of disorder on the magnetic properties.

---

[1]The calculated MCA in this thesis is order of magnitude up to some meV/atom.

4.1 Fe, Co, and Ni

4.1.1   Calculational Details

The $3d$ transition metals Fe (BCC), Co (FCC), Co (HCP), and Ni (FCC) were studied using FPLO in its version 8.65. The presented results were calculated using the experimental lattice constants [85], as summarised in Table 4.1. The cut-off angular momentum $l_{max} = 4$ was used for the expansion of the potentials and densities into spherical harmonics. We systematically increased the number of k-points from 12^3, 24^3, 48^3, to 96^3 in the Brillouin zone (BZ). In order to achieve an accuracy by about $1\,\mu eV/atom$ in the total energy, one has to use 96^3 k-points in case of the cubic structures (Fe (BCC), Co (FCC), and Ni (FCC)), and in case of hexagonal Co (HCP) 48^3 k-points are sufficient (see discussion in Subsection 4.1.2). Orbital moments were calculated as discussed in Chapter 3. The OPC were applied in the non-relativistic (basis mapping) limit. LSDA as well as GGA were taken into account in order to analyse the dependence on the XC-potential.

Three different schemes were applied to evaluate the MCA. The first method defines the MCA as the energy difference of two distinct spin quantisation axes $\hat{\mathbf{n}}_i$, Eqn. (4.1). This method gives the most accurate results, if the total energy supplies sufficient accuracy. The second method made use of the *force theorem* (FT) [86]. There, a SR[2] calculation was converged self-consistently. Followed by a non self-consistently single-step calculation including SO interaction and appropriate chosen quantisation axis $\hat{\mathbf{n}}_i$. This was done by a full relativistic calculation. The MCA was then estimated as the difference of the sum of the occupied band energies $\epsilon_n\,(\hat{\mathbf{n}}_i)$, Eqn. (4.2). A number of k-points is needed in both, the SR and the full relativistic cycle, to ensure sufficient accuracy in the total energy in order to estimate the MCA. The third method picks up the idea of Bruno [87]. It was shown by him that by using the perturbation theory the anisotropy constants K_n scale as $(\xi_{nl}/\triangle)^n$, in which $\triangle$ is the characteristic band splitting[3] and ξ_{nl} is the SO coupling constant. Typically, this ratio is for d-shells very small, and the expansion in Eqn. (2.74) - Eqn. (2.76) can be truncated after the first non-vanishing term. It turned out, that the MCA can be approximated via the difference of the magnetic orbital moments $\mu_l\,(\hat{\mathbf{n}}_i)$ of the two quantisation axes and then multiplied with the corresponding ξ_{nl}, Eqn. (4.3). When including OPC in the Hamiltonian, the last formula has to be generalised to Eqn. (4.4) [88].

We remark, that the ansatz of Bruno is applicable only for systems with more than half filled shells, which holds for the elements Fe, Co, and Ni. We approximated ξ_{nl} as difference the of one-particle energies, Eqn. (4.5), which were taken from the solution of atomic Kohn-Sham-Dirac equation. The resulting values are tabulated in Table 4.1. The quantisation axes were taken in analogy to Trygg et al. [61].

---

[2]The SR ansatz disregards the SO coupling, thus a wave function with non relativistic symmetry can be used.

[3]$\triangle \sim 1\,eV$

Table 4.1: Input parameters for Fe, Co, and Ni in our DFT calculations.

	Fe (BCC)	Co (FCC)	Co (HCP)	Ni (FCC)
Spacegroup	229	225	194	225
Wyckoff Position	(0, 0, 0)	(0, 0, 0)	$\left(\frac{1}{3}, \frac{2}{3}, \frac{1}{4}\right)$	(0, 0, 0)
a [Å]	2.867	3.569	2.507	3.524
c [Å]	2.867	3.569	4.070	3.524
$\xi_{3d, lsda}$ [meV/atom]	62.2	78.4	78.4	97.2
$\xi_{3d, gga}$ [meV/atom]	61.6	77.9	78.0	96.7
$\hat{\mathbf{n}}_1$	001	001	001	001
$\hat{\mathbf{n}}_2$	111	111	100	111

$$\triangle E_{mca} = E^{total}(\hat{\mathbf{n}}_1) - E^{total}(\hat{\mathbf{n}}_2) \tag{4.1}$$

$$\triangle E_{mca}^{ft} = \sum_i^{occ.} \epsilon_i(\hat{\mathbf{n}}_1) - \sum_i^{occ.} \epsilon_i(\hat{\mathbf{n}}_2) \tag{4.2}$$

$$\triangle E_{mca}^{Bruno} = -\frac{\xi_{nl}}{4\mu_B}(\mu_l(\hat{\mathbf{n}}_1) - \mu_l(\hat{\mathbf{n}}_2)) \tag{4.3}$$

$$\triangle E_{mca, op}^{Bruno} = -\frac{1}{2\mu_B}\left(\frac{\xi_{nl}}{2} + \sum_s B_s M_{Ls}\right)(\mu_l(\hat{\mathbf{n}}_1) - \mu_l(\hat{\mathbf{n}}_2)) \tag{4.4}$$

$$\xi_{nl=3d} \approx \frac{2}{5}\left(\epsilon_{d_{\frac{5}{2}}} - \epsilon_{d_{\frac{3}{2}}}\right) \tag{4.5}$$

In the following the density of states (DOS), magnetic moments, and MCA are analysed under the influence of the three OPC schemes (OPB, OPxc, and OPx) for the three transition metals.

4.1.2 Results

We begin with a comparison of the DOS among the studied $3d$ elements. Figure 4.1 presents the calculated DOS for Fe, Co, and Ni in LSDA. The DOS were calculated for a pure full relativistic LSDA+SOC calculation and using several OPC (OPB, OPxc, OPx) applied to the $3d$ states. We found no significant influence of the OPC on the DOS. The DOS is also shown for calculations by Chadov et al. [89]. They used a KKR method using LSDA and using LSDA + *dynamical mean field theory* (DMFT) to account for local correlation effects. Their DMFT results were obtained with the chosen parameters $U_{Fe, BCC} = 1.8\,eV$, $U_{Co, FCC} = 2.3\,eV$, $U_{Co, HCP} = 3.0\,eV$, and $U_{Ni, FCC} = 2.8\,eV$ and $J = 0.9$ (in all cases). The Temperature was adjusted to $400\,K$. The static double counting was subtracted from the self-energy in the so-called "around mean-field limit" (AMF) [90]. The DOS obtained with the KKR method were in good agreement with the DOS obtained using FPLO for all 4 considered cases. The renormalisation of the DOS arising from the DMFT method was already intensively studied by Grechnev et al. [91]. The same input parameters U and

J as defined above were used in there, and the Temperature was the same as used above. Both DMFT calculations showed the same features in the DOS. The authors showed that correlation mainly affects on the majority-spin band resulting in a narrowing of the d-band as compared to calculations using pure LSDA or GGA. In fact, it is well-known that LSDA (GGA) fail in describing the excitation spectra quantitatively for Fe, Co, and Ni. Photoemission spectra [92–94] data show that pure LSDA (GGA) calculations yield too broad majority $3d$ bands and overestimate the spin splitting. A narrowing of the $3d$ majority band was seen by using DMFT, but the $3d$ bands remained broad in the presence of OPC. A recent study of Sánchez-Barriga et al. [95] showed that DMFT based calculations in principal yield good agreement in comparison with experimental spin resolved *angle resolved photoemission spectroscopy* (ARPES) for low binding energies for many of the peak positions. However, a quantitatively agreement was not achieved for higher binding energies. The authors concluded that at least in their calculations the mass renormalisation and scattering rates were underestimated. Nevertheless, Lichtenstein et al. already proposed that DMFT (local approach) shall work better for Ni and Co than for Fe [96]. The non-locality of correlation effects in Fe was shown recently by Schäfer et al. [97] with angle-resolved photoemission experiments. These last remarks suggest that more many-body calculations involving non-local schemes, which consider non-local fluctuations in multi-band systems, are needed.

The spin magnetic moments differed only slightly for LSDA, OPC, and DMFT. The peak in the minority band at about $1.8\,eV$ (Figure 4.1a) was moving to lower energies for Co and Ni (Figure 4.1b, Figure 4.1c, and Figure 4.1d). In fact, this was also seen by comparing the band filling of the corresponding $3d$ elements. The LSDA and GGA calculations showed that Fe (BCC) have 6.5 electrons in the $3d$ shell. The occupation number changed to 7.5 electrons per shell for Co and 8.5 electrons per shell for Ni. The calculated spin moments in LSDA are about $2.2\,\mu_B/(3d \cdot \text{atom})$ for Fe, $1.6\,\mu_B/(3d \cdot \text{atom})$ for Co (FCC and HCP), and $0.6\,\mu_B/(3d \cdot \text{atom})$ for Ni. The obtained spin moments overestimate the experimentally measured quantities slightly, Table 4.6. The spin split was slightly decreased in case of DMFT calculations, but not in the case of applied OPC.

We will discuss the influence of OPC on the orbital magnetic moments next. The fully relativistic calculated orbital moments for LSDA are presented in Table 4.6. The GGA results deviate from the LSDA moments mostly by about $1 - 3$ %, see Table 4.6. An exception are the orbital magnetic moments of Co (FCC, and HCP), where the deviation was about $10 - 15$ %. However, it was found that applied OPC has the same effect on top of either LSDA or GGA.

It turned out, that μ_l was not dependent on the chosen XC-functional (either LSDA or GGA) for a pure SOC calculation. Thence, the same μ_l were obtained for the considered transition metals using either LSDA or GGA. By comparing the calculated μ_l (without OPC) with available experiments[4] one recognises, that the calculated μ_l were substantially lower by about $45 - 65$ % for Fe

---

[4] Neutron scattering data [98–100], *Einstein - de Haas* (EdH) gyro-magnetic ratio measurements [101, 102] and *x-ray magnetic circular dichroism* (XMCD) measurements [103], respectively. Bear in mind that the neutron scattering experiments and the XMCD experiments are sensible to the $3d$ electrons only, despite the EdH experiment accounts for the total gyro-magnetic ratio and yield in combination with e.g. magnetisation measurements the effective μ_s and effective μ_l.
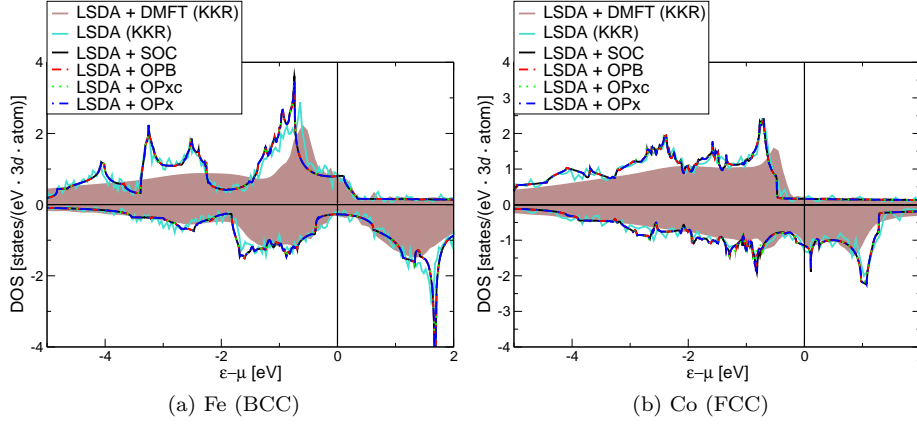
Figure 4.1: DOS for $3d$ elements calculated with FPLO8.65 in LSDA. The DOS is shown for fully relativistic calculations in which only SOC was taken into account (black line). Additionally calculations applying several OPC $3d$ states were performed (OPB - red dashed line, OPxc - green dotted line, OPx - blue dashed line). Results of Chadov et al. [89] using a KKR method using LSDA (turquoise full line) and using LSDA + DMFT are shown (brown background) as well (details text).

(BCC), 50 % for Co (FCC), $40 - 50$ % for Co (HCP), and up to 7 % for Ni (FCC) than the related measured orbital moments.

This fact of underestimating the orbital moment is correlated with the maximum orbital polarisation of atomic shells at quarter and three quarter filling. It was shown by Söderlind et al. that this discrepancy is lifted by applying the OPB [104]. Our results using the OPB, OPxc, and OPx method confirmed this conclusion, Table 4.6. The OPxc approach yielded orbital momenta being by about 33 % − 50 % larger than the experimentally observed quantities. The OPx method were in best agreement compared to the the related experimentally observed quantities of all considered theoretical schemes.

In order to classify the results using the OPC schemes, a comparison with available calculations from literature is presented. The *exact exchange* (EXX) + CDFT calculations belonging to the class of optimised effective potential models provides orbital moments which were by far to small, even smaller than those moments obtained for pure SOC calculations. Solovyev applied the (*constrained*) a parameter-free *random phase approximation* ((c)RPA) method, which makes use of a screened interaction to improve the description of orbital magnetism. The computed orbital moments were substantially lower than the experimental ones for Fe and Co and are equal to experimental moments for Ni. Recent DMFT results [105] slightly overestimate the orbital moments for the parameters which were applied in these calculations. Finally, a *Tight-binding* (TB) + HF as an example for a model Hamiltonian method is presented [106], with the Slater integrals F^l ($l = 0, 2, 4$) as input parameters for the $d - d$ interaction. By taking the optimum screened Slater integrals (F^l)[5] a quantitatively

---

[5]A screening of 30 % for F^2 and F^4, except for Co (FCC), in which only the moments referring to a screening of 20 % are presented. F^0 was then adjusted that the measured $\mu_s +$

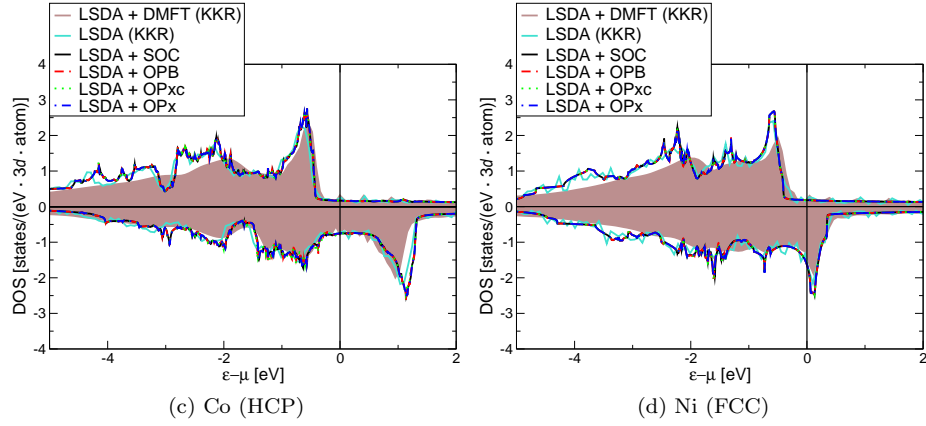(c) Co (HCP)   (d) Ni (FCC)

Figure 4.1: The same notation as in Subfigures 4.1a and 4.1b is used.

good agreement of the orbital moments calculated by TB + HF compared to the related experimentally observed quantities was observed. OP mainly arises in $3d$ metals as a result of SO interaction.

Nevertheless, the results for the orbital moments obtained with EXX + CDFT clearly demonstrate that non-local correlation effects are non-negligible. However, care is needed in the way of taking into account the correlation contribution. The results obtained with OPxc overshoot the experimentally observed quantities by far.

Finally, the results for the MCA obtained using the three methods discussed at the beginning of this section are presented. A number of test calculations for all considered transition metals were made due to two reasons. Firstly, we wanted to assure sufficient accuracy in the total energy of the applied methods. Secondly, we wanted to make sure that no systematic errors were introduced by the reason of using different symmetries. Figure 4.2 shows the convergence of the anisotropy with respect to the number of k-points used. We see here that in order to achieve convergence in the number of k-points we needed about at least 48^3 (24^3) k-points in the BZ for the cubic structures, respectively LSDA (GGA), and we needed at least 24^3 k-points in the BZ for LSDA and GGA in case of Co (HCP). The number of k-points in the irreducible wedge of the BZ were around $\sim$ 60000 for the cubic structures and $\sim$ 5500 for Co (HCP) for the lowest symmetry direction. In comparison with previous calculations the number of k-points used in the irreducible wedge of the BZ were either comparable [61], or even smaller [107] for Co (HCP). In case of the cubic structures 10 times more k-points were used than in [61]. In contrast to previously mentioned calculations we present MCA energies which were obtained using a full-potential method. Thus, we can conclude that we calculated the MCA very accurately compared with previous calculations and that the obtained energies were at the limit of current computer capacities.

As regards the calculated MCA energies for Fe are presented in Table 4.2. Our results confirm the previously obtained energies by Trygg et al. [61]. The correct easy axis was obtained for all applied methods. GGA and LSDA yielded
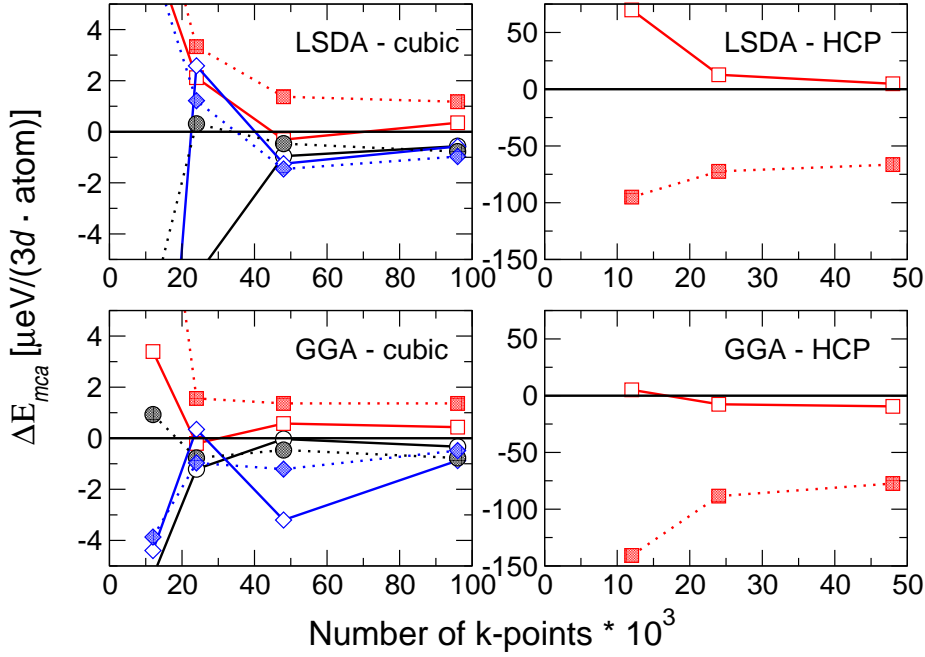

μ_l was reproduced [85].

Figure 4.2: Convergence of the MCA for Fe (BCC), Co (FCC), Co (HCP), and Ni (FCC) as a function of the number of k-points in the BZ for LSDA and GGA. Notation as following: ○—○ - Fe (total energy), ○··○ - Fe (Bruno's formulae), □—□ - Co (total energy), □··□ - Co (Bruno's formulae), ◇—◇ - Ni (total energy) and ◆··◆- Ni (Bruno's formulae). The MCA is given in $\mu eV/(3d \cdot atom)$.

similar results. When comparing the total energy results with experimentally observed, one recognises that pure SOC calculations underestimated the MCA by a factor of $2 - 4$. This quantitatively discrepancy was remedied by applying OPC, as previously concluded [108]. We remark that the MCA energies calculated with the help of the force theorem method were of comparable magnitude as the energies obtained from total energy calculations. Bruno's model yielded values for the MCA which are higher by a factor of 2 than the corresponding total energy calculations. It was found that those energies calculated with the OPx scheme were in best agreement with experimentally observed quantities. OPxc overestimated the MCA by a factor of $3.5 - 7.0$, for total energy calculations or for Bruno's model, respectively.

Analogous conclusions can be made, when looking at Co (FCC), Table 4.3, and Co (HCP), Table 4.4. Minor exceptions were found for Co (HCP), in which the wrong sign for the MCA was obtained for a pure SOC calculation in LSDA for a total energy calculation and a force theorem calculation. Only Bruno's model in LSDA for a pure SOC calculation yielded the correct sign of the MCA.

The situation changed completely, when analysing the results for the MCA of Ni (FCC), Table 4.5. In all but two calculations the wrong easy axis was predicted compared to experiment. The correct easy axis was found for OPB and OPxc, both using GGA and using Bruno's model, see Eqn. (4.3). Hence, in that respect previously conducted investigations were confirmed [61]. Applied

Table 4.2: MCA energies for Fe (BCC) evaluated from total energy differences. The notation is as following: SOC means SO coupling only, OPB, OPxc, and OPx were applied to the 3d-states. The calculations based on the LMTO method are taken from [61]. Experimental values (red marked) can be found in [85]. The units are given in μeV/(3d · atom).

Scheme		LSDA	GGA
Force Theorem	FPLO + SOC	−0.5	−0.5
Bruno	FPLO + SOC	−0.8	−0.8
	FPLO + OPB	−6.2	−5.2
	FPLO + OPxc	−11.3	−9.0
	FPLO + OPx	−3.5	−3.1
Total Energy	FPLO + SOC	−0.6	−0.3
	FPLO + OPB	−2.6	−2.1
	FPLO + OPxc	−4.5	−3.4
	FPLO + OPx	−1.7	−1.3
Trygg	LMTO + SOC	-0.5	
	LMTO + OPB	-1.8	
Experiment		-1.4	

Table 4.3: MCA energies for Co (FCC) evaluated from total energy differences. The notation is as following: SOC means SO coupling only, OPB, OPxc, and OPx were applied to the 3d-states. The calculations based on the LMTO method are taken from [61]. Experimental values (red marked) can be found in [85]. The units are given in μeV/(3d · atom).

Scheme		LSDA	GGA
Force Theorem	FPLO + SOC	0.3	0.6
Bruno	FPLO + SOC	1.2	1.4
	FPLO + OPB	13.1	14.2
	FPLO + OPxc	45.0	51.1
	FPLO + OPx	8.1	8.7
Total Energy	FPLO + SOC	0.4	0.4
	FPLO + OPB	4.2	4.9
	FPLO + OPxc	14.1	15.5
	FPLO + OPx	2.5	3.1
Trygg	LMTO + SOC	0.5	
	LMTO + OPB	2.2	
Experiment		1.8	

Table 4.4: MCA energies for Co (HCP) evaluated from total energy differences. The notation is as following: SOC means SO coupling only, OPB, OPxc, and OPx were applied to the $3d$-states. The calculations based on the LMTO method are taken from [61]. Experimental values (red marked) can be found in [85]. The units are given in $\mu eV/(3d \cdot atom)$.

Scheme		LSDA	GGA
Force Theorem	FPLO + SOC	6.3	−7.6
Bruno	FPLO + SOC	−33.2	−38.7
	FPLO + OPB	−115.1	−143.9
	FPLO + OPxc	−182.2	−233.5
	FPLO + OPx	−89.7	−111.5
Total Energy	FPLO + SOC	4.5	−9.4
	FPLO + OPB	−107.9	−144.8
	FPLO + OPxc	−193.5	−254.0
	FPLO + OPx	−73.0	−102.0
Trygg	LMTO + SOC	−29.0	
	LMTO + OPB	−110.0	
Experiment		−65.0	

OPxc and OPx did not provide the correct easy axis. Enhancement of the MCA for applied OPC was found to be rather small for Ni (FCC). Thus, in almost all studied cases OPC did not change the direction of easy axis in our calculations[6]. Nevertheless, OPC favours larger anisotropy in the orbital moments leading to larger anisotropy energies.

4.1.3 Summary

We demonstrated that OPC is necessary to improve the quantitatively agreement of orbital moments and MCA between theory and experiment. As a result, the most affected quantities by OPC are the orbital magnetic moment and MCA while the change of the spin moment is almost negligible. The OPC has no influence on the DOS. Further DMFT calculations are needed to describe satisfyingly experimentally observed photoemission spectra[7]

We conclude that the spin magnetic moment is already well described by SO coupling. Applied OPC revealed no influence on μ_s. As opposed to this the orbital moment was underestimated by about $40 - 60$ % in a pure SO calculation and the related MCA was underestimated even more without OPC. Overall, we got the general tendency for the corresponding orbital properties, experiment $\approx$ OPx $\leq$ OPB $\leq$ OPxc for the considered $3d$ metals.

---

[6]The only exceptions are the calculations for Ni (FCC) using GGA + (OPB and OPxc) and applying Bruno's formula, see Table 4.5.

[7]Photoemission spectra are related to excitations, while DFT only accounts for the ground-state. Of course, we can consider DFT as a good approximation for the excited states also by considering occupied states above ϵ_f.

Table 4.5: MCA energies for Ni (FCC) evaluated from total energy differences. The notation is as following: SOC means SO coupling only, OPB, OPxc, and OPx were applied to the $3d$-states. The calculations based on the LMTO method are taken from [61]. Experimental values (red marked) can be found in [85]. The units are given in μeV/($3d \cdot$ atom).

Scheme		LSDA	GGA
Force Theorem	FPLO	−0.8	−1.4
Bruno	FPLO + SOC	−1.0	−0.5
	FPLO + OPB	−1.1	0.5
	FPLO + OPxc	−1.1	0.3
	FPLO + OPx	−1.3	−0.3
Total Energy	FPLO + SOC	−0.6	−0.9
	FPLO + OPB	−0.7	−0.8
	FPLO + OPxc	−0.6	−0.8
	FPLO + OPx	−0.6	−0.9
Trygg	LMTO + SOC	−0.5	
	LMTO + OPB	−0.5	
Experiment		2.7	

Comparison of Co (FCC) and Co (HCP) anisotropy energies yielded $\triangle E_{mca}^{fcc}/\triangle E_{mca}^{hcp} \sim 0.033 - 0.100$. The experimentally observed ratio is about 0.028, calculations by Trygg delivered a ratio about $0.020 - 0.016$. The ratios calculated as total energy difference with applied OPx (LSDA and GGA: ≈ 0.037) were in best agreement as compared with the measured ratio. We observed that both LSDA and GGA yielded the same order of magnitude for the MCA. The band anisotropy of cubic systems should roughly be about a factor of $(\xi_{nl}/\triangle)^2$ weaker than the related quantity of uniaxial systems [87, 112]. Generally, for $3d$ elements holds: $\xi_{3d} \sim 0.05 - 0.06$ eV (for Fe and Co, respectively) and $\triangle \sim 1$ eV. This results in $(\xi_{3d}/\triangle)^2 = 36 \cdot 10^{-4}$, and is about 10 times smaller than the previous values. By this example we showed the qualitative character of the last estimation.

Furthermore, it was found that the easy axis can be predicted for that direction with the largest angular momentum. This was verified in all our calculations, e.g. for the pure SO calculations. Thus, the SO interaction already defines the direction of the easy axis and is not only described by OPC. Previous calculation [61, 89, 104, 106, 107, 111] were confirmed, using the full potential approach, LSDA as well as GGA calculations, and another type of OPC schemes. The sign of the MCA for Ni (FCC) remains an open question and could not be solved by means of our calculations, and is not a problem of LSDA solely as previously claimed [61]. Inclusion of spin flip excitations as well as magnetic orbital moments would be a further step to analyse $\triangle E_{mca}$, especially to explain anisotropy of bulk-like thin films.

Table 4.6: The spin magnetic moment μ_s, angular magnetic moment μ_l, and the total magnetic moment using different methods. The magnetic moments were calculated using LSDA (white row) and GGA (grey row), respectively. Experimental values are taken from [85, 98–100, 102, 103]. The (EXX) + CDFT refers to [109, 110]. The TB + HF results are taken from [106]. The RPA and c-RPA results can be found in [111], KKR (+ DMFT) is from [89]. All magnetic moments are given in $\mu eV/(3d \cdot atom)$.

	Fe (BCC)			Co (FCC)			Co (HCP)			Ni (FCC)		
Scheme	μ_s	μ_l	μ_l/μ_s	μ_s	μ_l	μ_l/μ_s	μ_s	μ_l	μ_l/μ_s	μ_s	μ_l	μ_l/μ_s
FPLO + SOC	2.21	0.05	0.02	1.64	0.08	0.05	1.59	0.08	0.05	0.62	0.05	0.08
	2.23	0.05	0.02	1.68	0.08	0.05	1.62	0.08	0.05	0.64	0.05	0.08
FPLO + OPB	2.21	0.10	0.05	1.64	0.16	0.10	1.59	0.16	0.10	0.62	0.08	0.13
	2.23	0.09	0.04	1.68	0.16	0.09	1.62	0.16	0.10	0.64	0.08	0.13
FPLO + OPxc	2.21	0.12	0.05	1.64	0.20	0.12	1.59	0.20	0.13	0.62	0.08	0.13
	2.23	0.05	0.02	1.68	0.22	0.13	1.62	0.23	0.14	0.64	0.08	0.13
FPLO + OPx	2.21	0.08	0.04	1.64	0.14	0.09	1.59	0.13	0.08	0.62	0.07	0.11
	2.23	0.08	0.03	1.68	0.14	0.08	1.62	0.14	0.09	0.64	0.07	0.11
EXX + CDFT	2.71	0.03	0.01	——	——	——	1.77	0.01	0.01	0.50	0.03	0.06
TB + HF[5]	2.10	0.11	0.05	1.52	0.11	0.07	1.56	0.15	0.10	0.56	0.06	0.11
LMTO + RPA	2.21	0.05	0.02	——	——	——	1.59	0.10	0.06	0.60	0.05	0.09
LMTO + c-RPA	2.20	0.06	0.03	——	——	——	1.59	0.11	0.07	0.60	0.06	0.09
KKR + SOC	2.25	0.05	0.02	1.64	0.08	0.05	——	——	——	0.63	0.07	0.11
KKR + DMFT	2.19	0.09	0.04	1.68	0.14	0.08	——	——	——	0.67	0.07	0.10
EXP (Neutrons)	*2.25*	*0.14*	*0.06*	*–*	*–*	*–*	*1.87*	*0.13*	*0.07*	*0.66*	*0.06*	*0.08*
EXP (EdH + magn. measurements)	*2.13*	*0.08*	*0.04*	*1.52*	*0.15*	*0.10*	*–*	*–*	*–*	*0.57*	*0.05*	*0.09*
EXP (XMCD)	*2.00*	*0.09*	*0.05*	*–*	*–*	*–*	*1.63*	*0.15*	*0.09*	*–*	*–*	*–*

4.2 Fe$_{1-x}$Co$_x$

4.2.1 Introduction

The current storage capacity of magnetic perpendicular recording disk devices can be found in the range of $200 - 300$ Gb/in^2 [113]. In order to store more information per unit area the grain number per bit has to be lowered. For yet higher densities, the super-paramagnetic limit [114] make specific demands on new materials, e.g. the general accepted criterion for magnetic data storage devices demands that 95 % of the original written magnetisation have to persist a period over 10 years. In order to avoid thermal instabilities, a minimal stability ratio of stored magnetic energy ($K_U \cdot V$), to thermal energy ($k_B \cdot T$) is required.

A crude appraisal demands on this ratio $K_U \cdot V / k_B \cdot T \approx 50 - 70$ [115], favouring materials with a large anisotropy. At the same time the anisotropy field $\mathbf{H}_K$ is determined by $\mathbf{H}_K = 2 \ K_U / \mathbf{S}$. In order to allow small switching fields this ratio has to be kept small. For that reason, materials combining a large uniaxial anisotropy K_U with a large magnetisation saturation $\mathbf{S}$ are the proper choice. Strained FeCo alloys combine a large uniaxial MCA with a large saturation magnetisation for certain chemical compositions x and certain tetragonal distortions. Table 4.7 gives an overview of currently used materials in hard disc drives (marked red), and shows several interesting alloys for future application. The anisotropy energies are expressed in meV$/(3d \cdot \text{atom})$.

This section begins with the presentation of the methods used to calculate the magnetic properties, Subsections 4.2.2 and 4.2.3. Calculational details can be found in Subsection 4.2.4. In Subsection 4.2.5 a discussion is given in which the results of disordered structures are compared to those of ordered structures. Finally, the influence of the used XC-potential on volume and anisotropy energies is given in Subsection 4.2.6. The section closes with a brief summary and conclusions are given in Subsection 4.2.7.

4.2.2 Fixed Spin Moment Calculations

A powerful tool to study itinerant magnetism is the *fixed spin moment* (FSM) method [125–127]. In this method the total energy E is calculated in dependence on the spin magnetic moment μ_s. Doing so, orbital contributions to magnetism are neglected in this approach. Hence, this approach is appropriate to describe $3d$ elements, for which yield $\mu_l/\mu_s \sim 0.1$, see Section 4.1.2.

Typically, this method is used to discuss meta-magnetic transitions [128]. In order to account for a fixed spin moment μ_s one has to add an additional constraint $h[\int \mathbf{S}(\mathbf{r}) \, d\mathbf{r} - \mu_s]$ into Eqn. (2.29). The magnetisation density $\mathbf{S}(\mathbf{r})$ is defined as $\mathbf{S}(\mathbf{r}) = \xi(\mathbf{r}) n(\mathbf{r})$, see Subsection 2.2.1.3. The Lagrange multiplier h supplies the constraint for a fixed spin moment. The functional derivative $\delta H[n] / \delta n_{\pm} = \mathbf{S}(\mathbf{r}) \pm h$, according to Eqn. (2.32), yields two spin dependent Fermi energies ϵ_f^s.[8] The two Fermi energies ϵ_f^s can be found with the help of

---

[8]The identification of $\epsilon_f \pm h$ as Fermi energy for the two different spins s is only justified, if the two spins are decoupled in the Hamilton matrix. This is not the case when SO coupling is present or when considering non-collinearity [129].

Table 4.7: The table shows a collection of several currently interesting alloys for application in recording disk devices and their related MCA. The MCA is listed either as experimentally observed, or theoretically calculated. The calculations were performed by DFT calculations. Calculations going beyond LDA or GGA are denoted with brackets. Currently used Co-based alloys are marked red [116–118]. Values for CoPd, FePd, CoPt, and FePt are taken from [59, 119, 120], MnAl is taken from [121, 122], YCo_5 and $LaCo_5$ are taken from [88, 123], and $SmCo_5$ is taken from [124]. The MCA is given in $meV/(3d \cdot atom)$.

System	Material	MCA $[meV/(3d \cdot atom)]$	
		experiment	theory
Co-based Alloys	*CoPtCr*	*0.10*	*– (–)*
	CoPtCrB	*0.05*	*– (–)*
	CoPd	0.30	0.40 (1.55)
L1$_0$ Alloys	CoPt	1.00	2.00 (4.00)
	FePd	0.45	0.30 (0.55)
	FePt	1.20	3.30 (3.70)
	MnAl	0.29	0.26
Rare Earth	YCo_5	0.76	0.02 (0.32)
Compounds	$LaCo_5$	1.12	0.07 (0.57)
	$SmCo_5$	3.20	2.24 (4.32)

the corresponding particle numbers N_e^s,

$$N_e^s = \int_{-\infty}^{\epsilon_f^s} D^s(\epsilon) \, d\epsilon, \tag{4.6}$$

where $D^s(\epsilon)$ is the spin dependent DOS. In that sense one may define an imaginary field $\mathbf{H}$ by taking the derivative of $H[n]$ with respect to the spin magnetisation density $\mathbf{S}(\mathbf{r})$,[9]

$$H = \left(\frac{\partial H[n]}{\partial S(\mathbf{r})}\right) = \frac{1}{2\mu_B}\left(\epsilon_f^+ - \epsilon_f^-\right) = \frac{1}{\mu_B}h. \tag{4.7}$$

The origin of two distinct ϵ_f^s has to be distinguished from that in conventional Stoner theory, in which the intra-atomic exchange splitting is responsible for the two ϵ_f^s. We performed scalar relativistic FSM calculations in order to check if the ground-state of $Fe_{1-x}Co_x$ alloys is either magnetic or non-magnetic.

4.2.3 Epitaxial Bain Path

A brief presentation about the Bain transformation is given next. Epitaxy and therewith relaxation processes are discussed as well in this context. Bain was

---

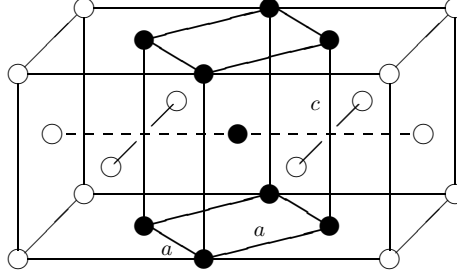[9]In the collinear approximation: $\mathbf{H} = H\mathbf{e_z}$ and $\mathbf{S} = S\mathbf{e_z}$.

Figure 4.3: The Bain transformation between the FCC structure and the BCC structure is shown. We denote the FCC structure by white dots ∘ and the BCC structure by black dots •. Realisation of the Bain transformation from FCC to BCC is done by an out-of-plane lattice distortion along the c-axis. Additionally, a rotation around the c-axis by an angle of $45°$ is needed. Finally, the lattice parameter a is reduced by a factor of $\sqrt{2}$ to obtain the BCC structure.

the first, who pointed out that a crystal can continouesly be transformed from a BCC structure to a FCC structure [84][10]. Figure 4.2.3 displays a transformation between these two cubic structures. It shall give a hint on how this transformation can be realised. More general transformations between two tetragonal phases involving other structures than the FCC structure and the BCC structure are possible as well. But we focus only on those paths between FCC and BCC symmetry, which in literature are summarised under the name Bain path or Bain transformation. Even though, Bain did not mention in his work that the volume has to be kept fixed along the transformation, many numerical studies in the past were made by keeping the volume constant [131].

Volume relaxation naturally takes place when depositing thin films on substrates. Figures 4.4a and 4.4b sketch this situation for a particular thin films on a certain substrate. In doing so, one can conclude that volume relaxation is essential when describing properties of thin films grown on substrates. The first work to our knowledge including relaxation processes while passing along the Bain transformation was done by Milstein et al. [132]. The authors considered transformations along the so-called *uniaxial Bain path*, in which the total energy $E = E(a(c), c)$ is calculated for all lattice parameters c. The in-plane lattice parameter a[11] is relaxed according to the fixed c so that the in-plane stress disappears ($\sigma_1 = \sigma_2 \equiv 0$).

Yet, another proposal was suggested by Marcus et al. [133]. Therein, the EBP was proposed, in which the total energy $E = E(a, c(a))$ is calculated in dependence on the lattice parameter a, which is specified by the substrate and which is assumed to have isotropic in-plane stress ($\sigma_1 = \sigma_2$). The lattice parameter c is calculated in such way that the out-of-plane stress σ_3 vanishes, see Eqns. (4.8, 4.9).

---

[10]Tetragonal deformations of thin films lead to stable or meta-stable phases. A phase corresponds to local minimum of the free energy and is stable under small tetragonal deformations. Usually, metals have two tetragonal phases. For further reading about phase stabilities in DFT we refer [130].

[11]Tetragonal symmetry is assumed to apply to all our calculations, meaning $a = b$.
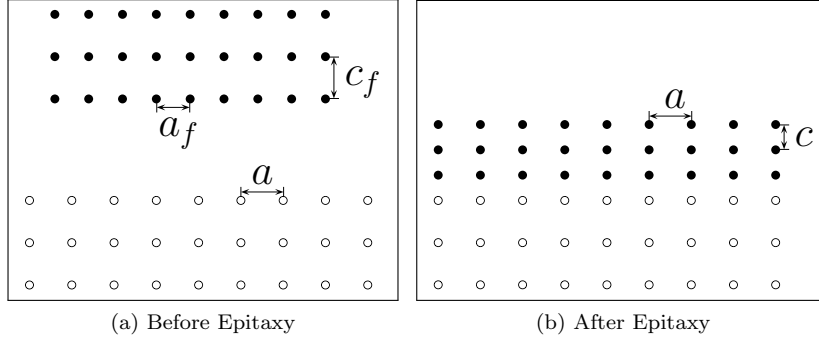
(a) Before Epitaxy   (b) After Epitaxy

Figure 4.4: The effect of volume relaxation of thin films grown on substrates is visualised, before epitaxy (Figure (a)) and after epitaxy (Figure (b)), respectively. We mark the substrate by white dots ○ and the film is represented by black dots ●.

$$\sigma_1 \;=\; \sigma_2 \;=\; \frac{1}{ca}\left(\frac{\partial E\,(a,\,c)}{\partial a}\right)_{a,\,c} \tag{4.8}$$

$$\sigma_3 \;\equiv\; 0 \;=\; \frac{2}{a^2}\left(\frac{\partial E\,(a,\,c)}{\partial c}\right)_{a,\,c} \tag{4.9}$$

There are two symmetry theorems along tetragonal transformations of states with cubic symmetry [133]:

Theorem 2 *The EBP must have an extremum in energy at all structures with cubic symmetry.*

Theorem 3 *On paths in the tetragonal plane on which the volume $V = c\,a^2\,/\,2$ is constant, E as a function of a or $c\,/\,a$ is an extremum at points of cubic symmetry.*

Figure 4.5 shows exemplarily the calculated EBP of Fe_xCo_{1-x} for $x = 0.5000$. The total energy was calculated in dependence on the lattice parameter a. Two substantial minima were recognised, respectively at $a = 2.380$ Å (FCC) and $a = 2.750$ Å (BCC). A zero in-plane stress σ_1 was obtained for both minima. We remark, that there must exist an instable maximum in between the two minima, in this particular case a tetragonal phase around $a \approx 2.556$ Å is found[12]. The in-plane stress σ_1 is vanishing at this maximum like it has been observed for the two minima. However, the maximum represents an instable state, which is not stable against small perturbation, in contradiction to the previous situation at the minimum.

Experimental realisation of this instable state is done by heterogeneous epitaxial growth. On the one hand this instable state is located in a region with

---

[12]Theorem two states that there is an extremum of the energy E at cubic points. This means that not only minima of the E are possible at cubic points, but also instable maxima. Then, the minima of E may be found at a stable or meta-stable BCT phase, in contrast to the situation presented in Figure 4.5
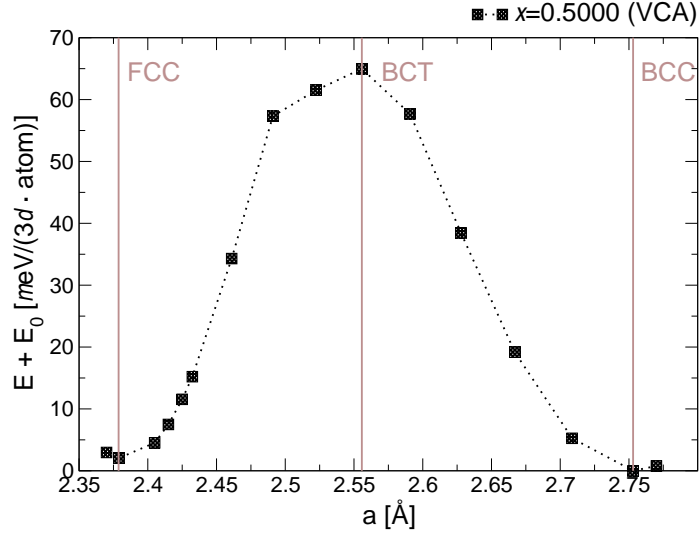
Figure 4.5: The EBP of a FeCo alloy using VCA in dependency on the lattice pa-
            rameter a with respect to LSDA is visualised. The EBP was calculated
            for $x = 0.5000$. The lattice parameter $a = 2.380$ Å designates the FCC
            phase (energy minimum), and $a = 2.750$ Å designates the BCC phase
            (another energy minimum). The maximum in between at $a = 2.556$ Å
            corresponds to an instable *body centered tetragonal* (BCT) state.

almost vanishing stress, which forms a useful condition to stabilise the film on
the substrate. On the other hand the stabilisation of a tetragonal distorted film
always depends on the magnitude of the lattice misfit between substrate and
film.

   In summary, the concept of EBP helps us to identify several phases of
strained materials. We can check quantitatively the elastic behaviour of thin
films, and we can predict stabilised phases on given substrates.

4.2.4   Calculational Details

DFT calculations for $Fe_{1-x}Co_x$ based on four different symmetries were em-
ployed with FPLO, version 8.65. The first scheme was used to describe disor-
der via the VCA method. For that reason a simple cubic BCT unit cell with
one atom per primitive unit cell had to be created, Figure 4.6a. Secondly,
calculations were done for a particularly created supercell (discussion below)
in order to simulate disorder and check the results obtained using VCA, Fig-
ure 4.6b. Thirdly, calculations of L1$_0$-type structure were performed, Figure 4.6c
($x = 0.5000$). Finally, calculations for the L1$_2$-type structure were performed,
Figure 4.6d ($x = 0.7500$). Table 4.8 summarises the input parameters for the
four distinct symmetries used in this work. A tetragonal-like character of the
unit cell was taken into account in all of our calculations. Consequently, this
leads to $c/a = 1$ for the BCC structure and $c/a = \sqrt{2}$ for the FCC structure.

   Previously undertaken investigations [81] assumed constant volume of 11.780

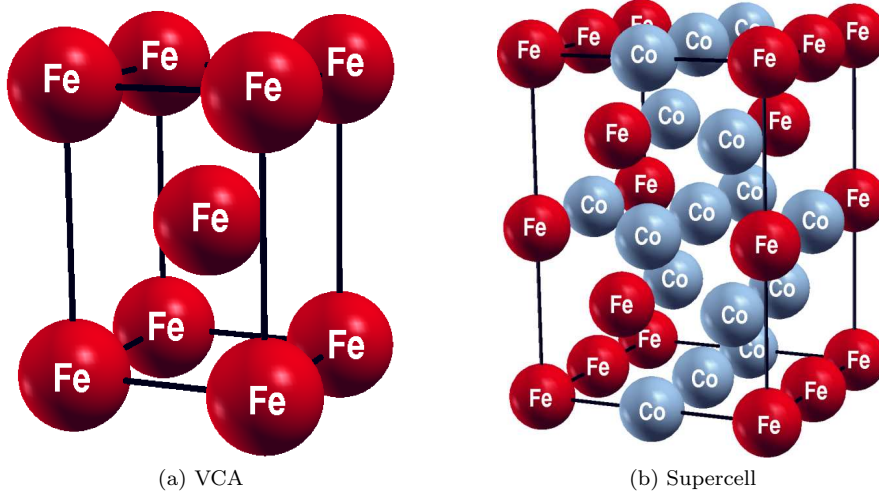(a) VCA   (b) Supercell

Figure 4.6: Different unit cells for FeCo alloys used in our computations. Figure (a)
displays the BCT unit cell for the VCA calculations, Figure (b) visualises
the character of the supercell for particular chosen $x = 0.6250$, Figure (c)
and Figure (d) present the ordered $L1_0$ - type and $L1_2$ - type phases,
respectively.

$Å^3$.[13] We considered volume relaxation along the EBP for every Co concentra-
tion x and every tetragonal distortion c/a for VCA as well as for the ordered
structures, the $L1_0$ structure and the $L1_2$ structure, respectively. Relaxation was
taken into account as discussed in Section 4.2.3. The relaxed lattice parameters
are given in Table 4.9. In case of the supercells the constant volume Bain path
(CVBP) was taken into account because of time and memory limitations. The
fixed volume for the supercells was taken from the optimised VCA structures
for which the largest MCA had been obtained. Table 4.11 presents the used
volumes. The supercell approach has been applied for $x = 0.5000$, and 0.5625
for LSDA and $x = 0.5000, 0.5625, 0.6250, 0.6875$, and 0.7500 for GGA.

The structural relaxation was done in the SR mode, that is, without SO
coupling. The k-point mesh was set to 24^3 to achieve sufficient accuracy. The
MCA was evaluated fully relativistic using 48^3 k-points. We performed total en-
ergy calculations for the MCA and compared these results with Bruno's model.
The quantisation axes were $\hat{\mathbf{n}}_1 = 100$ and $\hat{\mathbf{n}}_2 = 001$. In the case of the super-
cells we applied the force theorem to obtain the MCA. For the self-consistent
SR calculation we used 12^3 k-points. The additional non-self-consistent fully
relativistic one step calculation was done by using 15^3 k-points.

The accuracy of the force theorem method was tested for several k-point
meshes and for a particularly chosen geometry. For that reason a comparison
of anisotropy energies obtained with the force theorem and anisotropy energies
obtained from self-consistent calculations is given. The MCA was calculated as
discussed in Section 4.1.1. Table 4.10 summarises the results for the different
used k-point meshes. The geometry taken into account was spacegroup 123,
Wyckoff position Fe: $(0, 0, 0)$, and Co: $(1/2, 1/2, 1/2)$. The lattice parameters

---

[13]This corresponds to the measured Fe (BCC) volume.
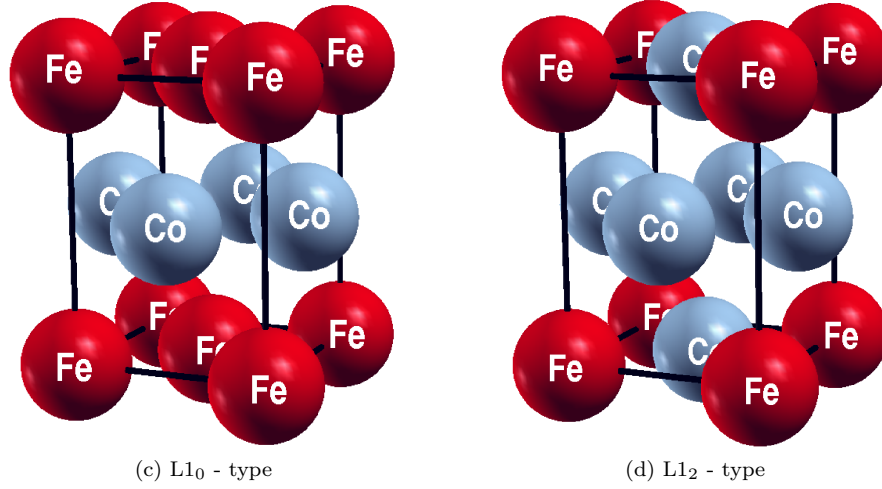
(c) $L1_0$ - type

(d) $L1_2$ - type

Figure 4.6: The same notation as in Subfigures 4.6a and 4.6b is used.

applied were $a = 2.556\,\text{Å}$, and $a = 3.171\,\text{Å}$. The most accurate results obtained with the self-consistent approach differs from the most accurate results obtained with the force theorem approach by about one % (marked red, in Table 4.10). A comparison using the force theorem approach between the most accurately calculated results and those results obtained by the k-point meshes which were used later on yielded an error bar by about $40-50\,\mu\text{eV/atom}$. The dependency on the XC-functional was carefully tested by applying both type of functionals, LSDA and GGA.

In order to test the results of the VCA calculations for the disordered state, we constructed supercells using a stochastic model which accounts for nearest neighbour distances and shall match the disordered state as much as possible, based on an idea given in [134]. The number of atoms per supercell was $2 \cdot 2^3 = 16$. To account for special arrangement of the atomic sites we had to use Spacegroup 1. But we still assumed a tetragonal character of the disordered pattern. The smallest number of different members[14] for the *ensemble average* (EAVG) for the particular applied symmetry was 9.

The 9 different patterns were obtained by firstly rotating the supercell (Figure 4.6b) around the x- or y-axis by $\pi/4$. In that way, three configurations were obtained: an unrotated cell, and two rotated cells. Then for every of the three arrangements three distinct spin quantisation axes can be chosen leading to 9 different patterns. The MCA was evaluated as the EAVG of the patterns: $\triangle \bar{E}^{ft}_{mca} = 1/N \sum_i \triangle \bar{E}^{ft}_{mca,\,i}$, in which $N = 9$ and i run over the different patterns for the supercells. In this particular case the following equations result from the symmetry considerations above:

---

[14]In case of cubic symmetry this the EAVG has to be taken for 48 different configurations, in tetragonal symmetry 16 different configurations remain, further symmetry considerations lead to 9 different configurations for our purpose.

Table 4.8: Input parameters for FeCo alloys in our calculations, VCA, Supercell, L1$_0$, and L1$_2$, respectively. The corresponding unit cells are visualised in Figure 4.6. The Wyckoff positions of the supercells are distributed to a certain number Fe atoms and a certain number of Co atoms in dependence on the Co concentration x and particular chosen member of the EAVG (see text).

	Spacegroup	Wyckoff Positions	
		Fe	Co
VCA	139	$(0, 0, 0)$	
Supercell	1	$(0, 0, 0)$ $(\frac{1}{4}, \frac{1}{4}, \frac{1}{4})$ $(0, 0, \frac{1}{2})$ $(\frac{1}{4}, \frac{1}{4}, \frac{3}{4})$ $(0, \frac{1}{2}, 0)$ $(\frac{1}{4}, \frac{3}{4}, \frac{1}{4})$ $(\frac{3}{4}, \frac{3}{4}, \frac{3}{4})$ $(0, \frac{1}{2}, \frac{1}{2})$ $(\frac{1}{4}, \frac{3}{4}, \frac{3}{4})$ $(\frac{1}{2}, 0, 0)$ $(\frac{3}{4}, \frac{1}{4}, \frac{1}{4})$ $(\frac{1}{2}, 0, \frac{1}{2})$ $(\frac{3}{4}, \frac{1}{4}, \frac{3}{4})$ $(\frac{1}{2}, \frac{1}{2}, 0)$ $(\frac{3}{4}, \frac{3}{4}, \frac{1}{4})$ $(\frac{1}{2}, \frac{1}{2}, \frac{1}{2})$	
L1$_0$	123	$(0, 0, 0)$	$(\frac{1}{2}, \frac{1}{2}, \frac{1}{2})$
L1$_2$	123	$(0, 0, 0)$	$(\frac{1}{2}, \frac{1}{2}, \frac{1}{2})$ $(\frac{1}{2}, \frac{1}{2}, 0)$

Table 4.9: Relaxed cubic lattice parameters of FeCo alloys in our calculations (along the EBP), rescaled to the BCT primitive unit cell. Deviation from the CVBP is given as: $f_{a_{fcc}/a_{bcc}} = 1 - (\sqrt{2})^{1/3} \cdot a_{fcc} / a_{bcc}$. For the CVBP holds: $a_{fcc} = a_{bcc} / (\sqrt{2})^{1/3}$. Deviation from the ideal ratio $a_{fcc} = \sqrt{2} \, c_{fcc}$ is found to be at most 1.4 % and due to relaxation. Here, it is defined: $f_{c_{fcc}/a_{fcc}} = 1 - \sqrt{2} \cdot a_{fcc} / c_{fcc}$. Both f functions are given in %.

	VCA		Supercell		L1$_0$		L1$_2$	
	LSDA	GGA	LSDA	GGA	LSDA	GGA	LSDA	GGA
a_{bcc} [Å]	2.752	2.825	2.746	2.817	2.775	2.850	2.750	2.815
a_{fcc} [Å]	2.378	2.466	2.447	2.510	2.382	2.512	2.421	2.500
c_{fcc} [Å]	3.390	3.494	3.460	3.550	3.415	3.563	3.431	3.565
$f_{a_{fcc}/a_{bcc}}$	3.0	2.0	0.0	0.0	3.7	1.1	1.2	0.3
$f_{c_{fcc}/a_{fcc}}$	0.8	0.2	0.0	0.0	1.4	0.3	-0.5	0.8

Table 4.10: MCA energies of a FeCo alloy calculated for the two quantisation axes, $\hat{\mathbf{n}}_1 = 100$ and $\hat{\mathbf{n}}_2 = 001$, respectively. The MCA was calculated for the following chosen input parameters using LSDA: the spacegroup was 123, the two Wyckoff positions were Fe (0, 0, 0) and Co (1/2, 1/2, 1/2), and the lattice parameters were $a = 2.556$ Å and $c = 3.171$ Å. Full relativistic self-consistent calculations were applied by using 12^3, 24^3, and 48^3 k-points. In case of the force theorem method we applied 12^3, 18^3, 24^3, and 48^3 k-points for the self-consistent SR calculation (left column) and then a full relativistic one-step calculation for 12^3, 18^3, 24^3, and 48^3 k-points (middle horizontal row) to estimate the accuracy of the force theorem method. The most accurate and the most inaccurate results are marked red.

Self-Consistent			
Full Relativistic K-Points	MCA [μeV/(3d · atom)]		
12^3	−78.0		
24^3	−124.9		
48^3	−124.9		

Force Theorem			
Scalar Relativistic K-Points	MCA [μeV/(3d · atom)] Full Relativistic K-Points		
	12^3	18^3	24^3	48^3
12^3	−72.5	−81.2	−85.7	−81.2
18^3	−118.9	−123.3	−123.7	−124.2
24^3	−106.7	−114.7	−116.3	−117.0
48^3	−117.7	−122.9	−123.0	−123.7

$$E_{\hat{\mathbf{n}}_l}^{band,\,cell} = \sum_i^{occ.} \epsilon_i^{cell}\left(\hat{\mathbf{n}}_l\right), \tag{4.10}$$

$$\bar{E}_{\hat{\mathbf{n}}_l}^{band} = \frac{E_{\hat{\mathbf{n}}_l}^{band,\,xyz} + E_{\hat{\mathbf{n}}_l}^{band,\,-zyx} + E_{\hat{\mathbf{n}}_l}^{band,\,x-zy}}{3}, \tag{4.11}$$

$$\triangle\bar{E}_{mca}^{ft} = \frac{\bar{E}_{100}^{band} - \bar{E}_{010}^{band}}{2} - \bar{E}_{001}^{band}. \tag{4.12}$$

Here, "xyz" denotes an unrotated cell, "$-zyx$" a rotation of $\pi/4$ about y-axis (or the [010] direction), and "$x - zy$" a rotation of $\pi/4$ about x-axis (or the [100] direction). We chose the three quantisation axes $\hat{\mathbf{n}}_l$ as: [100]-, [010]-, and [001]-direction, respectively.

Table 4.11: Volume V per formula unit of FeCo alloys used in the calculations for the supercells. The volume was taken from relaxed VCA calculations of certain Co concentrations x for which we obtained the largest MCA.

	LSDA	GGA
x	0.5000, 0.5625	0.5000, 0.5625, 0.6250, 0.6875, 0.7500
V [Å^3 / f.u.]	10.355	11.059

4.2.5 Results

Right at the outset we present the results obtained using VCA. Calculations were performed for 12 distinct Co concentrations $x \in [0.0000, 1.0000]$ and about $12 - 15$ points along the Bain path realising certain tetragonal distortions. The Bain path was considered in between the c/a ratio of 1.0 (corresponding to the BCC phase) and the c/a ratio of about $\sqrt{2}$ (FCC phase). Firstly, calculations along the CVBP were conducted to check previous results. The same results as obtained in the previous publications [81, 82] were obtained that is why we do not present them. Furthermore, we conclude that our results are reliable, since the same results were obtained with different codes (either using FP-LMTO or using FPLO).

Secondly, calculations along the EBP were applied in order to account for relaxation. The results for the EBP will be discussed now. Figures 4.7, 4.10, and 4.12 display the VCA results for the total energy E, spin magnetic moment μ_s, MCA, respectively. Additional calculations including OPB applied to the $3d$ states were done to get an upper limit for the MCA using both LSDA and GGA, respectively. The individual figures are discussed in more detail below. As a result we calculated in total about $140 - 150$ points for each figure. We interpolated these points using a usual spline method for our two dimensional data on a 1000×1000 grid. We applied two different orders for the spline method. Firstly, the spline was chosen to be of cubic order so as to account for a two times continuously differentiable function for total energy. The MCA is the difference of total energies. Hence, we used the same order for the spline as taken for the total energy. And secondly, in case of the spin magnetisation we used a linear spline. This idea was motivated to account for the rapid magnetic transition seen in LSDA ($x = 0.0000 - 0.5000$ and $a = 2.450 - 2.550$ Å), Figure 4.10a.

The normalised total energies of the optimised structures using the scalar-relativistic scheme can be found in the Figure 4.7a and Figure 4.7b (contour plots), for LSDA and for GGA, respectively. By comparing the results obtained with respect to LSDA and GGA, we conclude that both functionals qualitatively agree for large x. Differences in the energy landscape were seen for low x. However, there is found a very plane energy region for both functionals used for slightly different x. Before discussing the energy landscape in more detail, we again present the calculated normalised total energies in another way:

Figures 4.8a and 4.8b show the normalised total energy in dependence of the in-plane lattice parameter a for a certainly chosen Co concentration x. We found that in LSDA the FCC phase ($a \approx 2.450$ Å) is the lowest for almost all
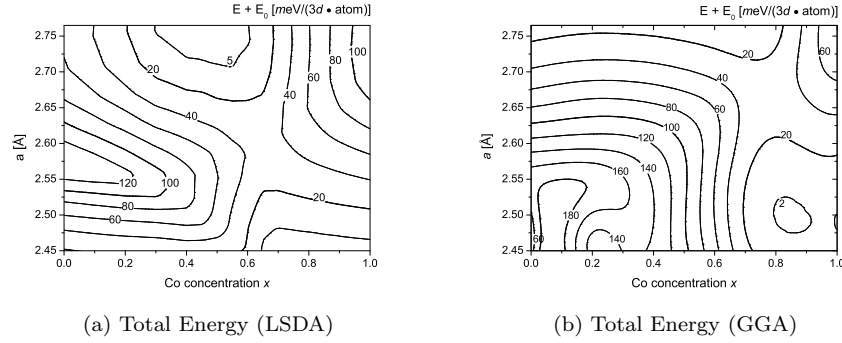
(a) Total Energy (LSDA)

(b) Total Energy (GGA)

Figure 4.7: Total energies of FeCo alloys with respect to Co concentration x using a cubic spline (see text), obtained with LSDA (Figure (a)) and GGA (Figure (b)). The total energies were calculated for relaxed unit cells with VCA and were normalised according to the lowest observed total energy E_0 obtained along the EBP for every particular Co concentration x. The contour line represent lines of constant total energy. The energies are given in meV/$(3d \cdot$ atom$)$.

(a) Energy Barrier - VCA (LSDA)
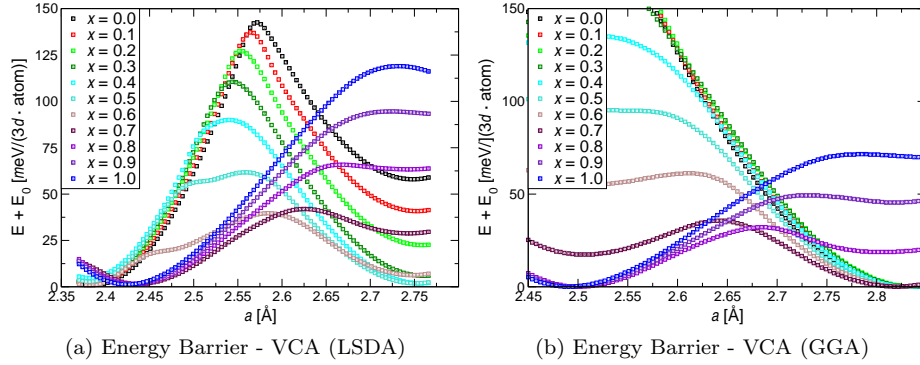
(b) Energy Barrier - VCA (GGA)

Figure 4.8: Normalised total energies of FeCo alloys with respect to lattice parameter a, obtained with LSDA (Figure (a)) and GGA (Figure (b)). The total energies were calculated for relaxed unit cells with VCA and were normalised according to the lowest observed total energy E_0 obtained along the EBP for every particular Co concentration x. The energies are given in meV/$(3d \cdot$ atom$)$. The most plane curves are found for $x \in [0.6000, 0.7000]$ and $x \in [0.7000, 0.8000]$, in LSDA and in GGA, respectively.

concentrations x, Figure 4.8a. For $x = 0.4000$, 0.5000, and 0.6000 we found nearly the same energies for FCC and BCC phase, with an energy difference lower than 5 meV/$(3d \cdot$ atom$)$. This was not the case in GGA. We observed that in GGA a change of the ground-state phase from FCC ($a \approx 2.500$ Å) to BCC ($a \approx 2.820$ Å) when going from $x = 1.0000$ to $x = 0.0000$, see Figure 4.8b. At very low concentrations the energy barrier between the cubic phases is about 130 meV/$(3d \cdot$ atom$)$ for LSDA and 190 meV/$(3d \cdot$ atom$)$ for GGA. At very high concentrations the energy barrier between the cubic

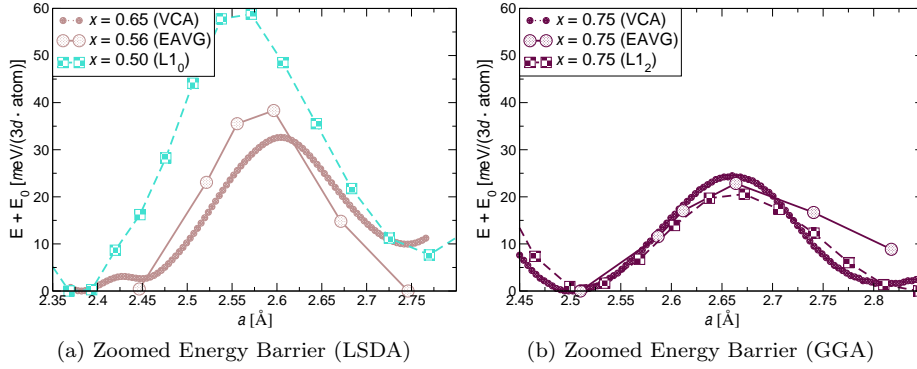(a) Zoomed Energy Barrier (LSDA) (b) Zoomed Energy Barrier (GGA)

Figure 4.9: Normalised total energy of FeCo alloys in dependency on the substrate
lattice parameter a obtained in LSDA (Figure (a)) and GGA (Figure (b)).
The total energies were calculated using VCA, EAVG, and for the $L1_0$-
type and the $L1_2$-type structures. In Figure (a) the VCA calculations were
performed for $x = 0.6500$, EAVG for $x = 0.5600$, and $L1_0$ for $x = 0.5000$.
In Figure (b) all results shown, use $x = 0.7500$. The energies are given in
meV/$(3d \cdot$ atom).

phases is about 100 meV/$(3d \cdot$ atom) for LSDA and 70 meV/$(3d \cdot$ atom) for
GGA. But for intermediate x a flat region of the total energy is observed being
highly interesting for experimental hetero-epitaxial growth of FeCo films grown
on specific substrates. This region is about $x \approx 0.5000 - 0.7000$ in LSDA and
shifted to slightly higher concentrations $x \approx 0.6000 - 0.8000$ in GGA.

As next the VCA results are compared with the results obtained from the
supercell calculations and with the results obtained for the corresponding or-
dered structures. For that reason the lowest obtained energy barrier in VCA
was estimated. In order to make a well justified comparison between the EAVG
and the ordered structures, only the closest fitting concentrations x were taken
into consideration. Figures 4.9a and 4.9b present the total energies for the
concentrations $x = 0.6500, 0.5625$, and 0.5000 (VCA, EAVG, and $L1_0$ struc-
ture, respectively) obtained with LSDA and for $x = 0.7500$ (VCA, EAVG, and
$L1_2$ structure) obtained with GGA. In LSDA, the flat energy region was pre-
dicted according to the results obtained with VCA at concentrations by about
$x \approx 0.6500$. An instable BCT state was seen (also for EAVG) at a substrate
lattice parameter $a = 2.604$ Å (EAVG: $a = 2.596$ Å). The energy barrier
between the two cubic phases was calculated to be about 35 meV/$(3d \cdot$ atom)
(VCA). The energy barrier as well as the position was confirmed by the calcu-
lations according to EAVG. The comparison with the $L1_0$ phase confirms the
position of the lattice parameter ($a = 2.571$ Å). But here the energy barrier
was found to be slightly higher of about 60 meV/$(3d \cdot$ atom). We remark that
in VCA there were two more meta-stable phases obtained for this particular x.
Additionally, a maximum of the total energy can be found around $a = 2.420$ Å
and a minimum was located around $a = 2.450$ Å. This was neither seen from
the EAVG nor from the $L1_0$ results.

In GGA, the instable BCT phase was shifted to larger substrate lattice
parameters: $a = 2.664$ Å, 2.664 Å, and 2.672 Å (for VCA, EAVG, and $L1_2$, re-

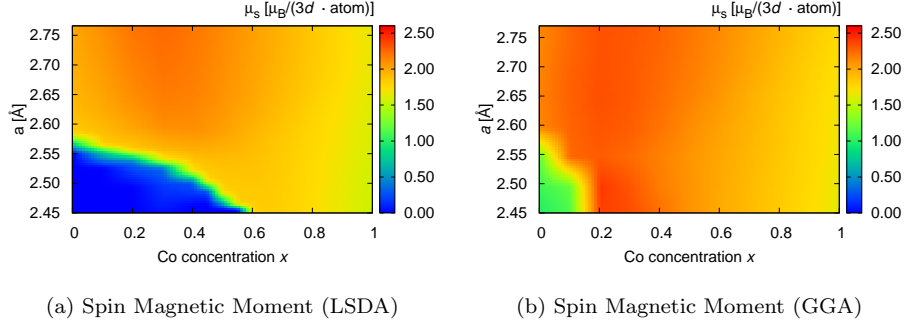(a) Spin Magnetic Moment (LSDA)   (b) Spin Magnetic Moment (GGA)

Figure 4.10: Spin magnetic moment μ_s of FeCo alloys with respect to Co concentration x and lattice parameter a using VCA, obtained with LSDA (Figure (a)) and GGA (Figure (b)). The quantisation axis was chosen to align along the [001]-direction. The spin magnetic moment is given in $\mu_B/(3d \cdot \text{atom})$.

spectively) and a larger Co concentration: $x \approx 0.7500$. The energy barrier was slightly smaller than obtained with LSDA by about 25 $meV/(3d \cdot \text{atom})$ using VCA. The ordered L1$_2$ phase yielded an energy barrier of about 21 $meV/(3d \cdot \text{atom})$, and the EAVG was in between according 23 $meV/(3d \cdot \text{atom})$. The two additional meta-stable phases obtained in LSDA (VCA) were not seen in any results obtained by GGA.

In order to find the magnetic ground-state FSM calculations were done at each point in the in the phase space (a, x). Figures 4.10a and 4.10b display the obtained spin magnetic moments of the ground-state in VCA in dependency on a and x, in LSDA and in GGA, respectively. A spin magnetisation collapse in LSDA for the FCC phase was found at concentrations around $x \approx 0.0000 - 0.6000$. We observed three different magnetic states for these concentrations along the EBP. A *high magnetic state* (HMS) with $\mu_s \approx 2.0 - 2.5 \, \mu_B/(3d \cdot \text{atom})$ for high parameters a, a *non-magnetic state* (NMS) for low parameters a, and a *low magnetic state* (LMS) $\mu_s \approx 1.0 \, \mu_B/(3d \cdot \text{atom})$ in between, Figure 4.10a. In case of higher concentrations there was found only one magnetic phase, and the spin magnetic moment adjusts to that of pure Co: $\mu_s = 1.59 \, \mu_B/(3d \cdot \text{atom})$. In GGA, the spin magnetic moment μ_s was found to be more stable in the whole phase space (a, x) as observed with LSDA, see Figure 4.10b. In Figure 4.10b only two magnetic phases were observed at low concentrations $x \approx 0.0000 - 0.2000$, the HMS and the LMS. This difference between LSDA and GGA had already been discussed in the case of pure Fe (BCC and FCC) [135].

Our calculations confirm previously obtained results [135] and extend the phasespace to FeCo alloys. As it was the case for LSDA a HMS was found for large x. The calculated spin magnetic moments in GGA were slightly larger than the corresponding LSDA moments for the same a and the same x. We mention that the HMS was obtained in that (a, x)-region which was previously predicted to be very suitable for hetero-epitaxial growth. Figure 4.11 displays μ_s in dependence on a for the chosen concentrations $x = 0.5000$, and 0.7500 obtained in LSDA, see Figure 4.11a and 4.11b, respectively. In both figures a comparison of the calculated spin magnetic moment between several applied
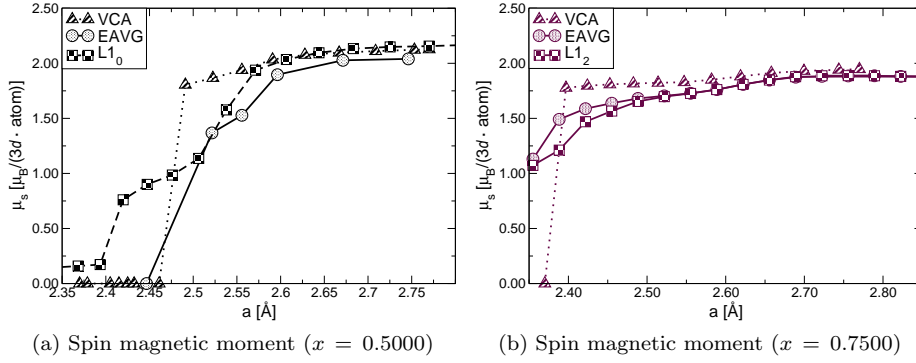
(a) Spin magnetic moment ($x = 0.5000$) (b) Spin magnetic moment ($x = 0.7500$)

Figure 4.11: Spin magnetic moment μ_s of FeCo alloys with respect to the lattice parameter a, obtained with LSDA. The spin magnetic moment was calculated using VCA, EAVG, and for the $L1_0$-type (Figure (a)) and the $L1_2$-type (Figure (b)) structures, respectively. The quantisation axis was chosen to align along the [001]-direction. The magnetic moment is given in $\mu_B/(3d \cdot \text{atom})$.

methods (VCA, EAVG, and $L1_0$ structure or $L1_2$ structure, respectively) is shown. In Figure 4.11a we recognise that the magnetic collapse was observed at $x = 0.5000$ and $a = 2.470$ Å in VCA. The magnetic collapse was confirmed by the results obtained with EAVG. The results obtained using the $L1_0$ structure yielded a much more broad range for a in which the magnetic collapse occurs. In contrast to VCA and EAVG, the $L1_0$ structure yielded non-vanishing spin magnetic moments for small a. At $x = 0.7500$ there was no magnetic collapse seen for EAVG and for $L1_2$, as previously obtained using VCA.

By analysing the magnetic properties we turn the focus now on the MCA of FeCo alloys. The Figures 4.12a, 4.12b, 4.12e, and 4.12f present the MCA calculated as total energy difference for the quantisation axes [100]-direction and [001]-direction, for LSDA, for GGA, for LSDA + OPB, and for GGA + OPB, respectively. *Perpendicular magnetic anisotropy* (PMA) was predicted using VCA around $x \approx 0.3000 - 0.6000$ and $a \approx 2.500 - 2.600$ Å for LSDA, in case of GGA we found $x \approx 0.4000 - 0.7000$ and $a \approx 2.550 - 2.650$ Å (red marked area in Figures 4.12a - 4.12f). The largest PMA obtained in our calculations are around $600\ \mu\text{eV}/(3d \cdot \text{atom})$ for both XC-potentials, LSDA and GGA, respectively. In-plane anisotropy (blue area) was found at the concentrations $x \approx 0.0000 - 0.4000$ and $x \approx 0.8000 - 1.0000$ in LSDA. We observed the same tendency in GGA. The in-plane anisotropy scales as half of the magnitude of the largest PMA.

In order to compare the MCA energies obtained from total energy differences, we additionally calculated the MCA energies with the help of Bruno's model, see Figures 4.12c and 4.12d. For that reason the SO coupling constant was linearly interpolated $\xi_{3d,xc}^{vca} = (1 - x)\,\xi_{3d,xc}^{Fe(bcc)} + x\,\xi_{3d,xc}^{Co(fcc)}$ in dependency on the chosen XC-potential and for a particular chosen concentration x. The MCA energies obtained using Bruno's model yielded the same order of magnitude as the MCA energies obtained by total energy differences.

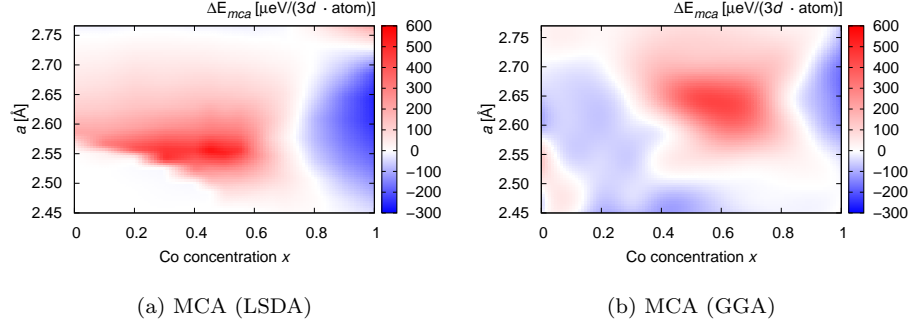Furthermore, the MCA was evaluated with additionally applied OPB to the

(a) MCA (LSDA)

(b) MCA (GGA)

Figure 4.12: MCA energies of FeCo alloys with respect to Co concentration x and lattice parameter a using VCA, obtained with LSDA and GGA, respectively. The MCA was calculated by VCA (Figures (a) and (b)), by Bruno's model (Figures (c) and (d)), and by additionally applied OPC on top of SOC (Figures (e) and (f)). The two quantisation axes were chosen to be the [001]-direction and the [100]-direction (see text). The MCA is given in μeV/(3d · atom).

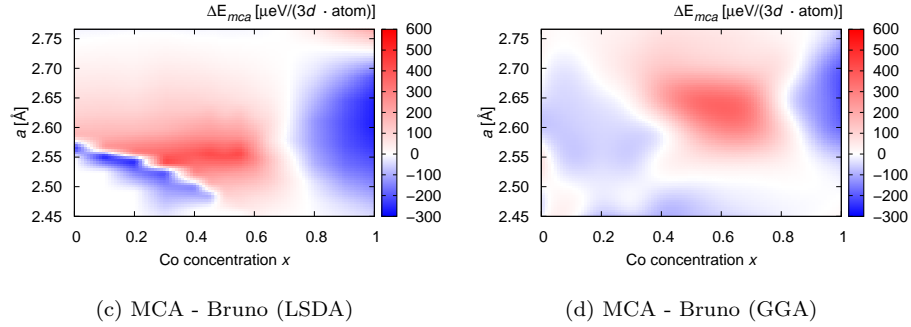(c) MCA - Bruno (LSDA)

(d) MCA - Bruno (GGA)

Figure 4.12: The same notation as in Subfigures 4.12a and 4.12b is used.

3d states, Figures 4.12e and 4.12f. No qualitatively change was seen as compared to the results obtained without OPB seen. However, we recognised an increasing of the MCA by a factor of 2 when additionally applying OPB.

Next the anisotropy energies obtained using the EAVG are compared with the VCA results as well as the corresponding ordered structures. Figure 4.13 presents the anisotropy energies for $x = 0.5000$, and $x = 0.5625$ using LSDA, see Figures 4.13a and 4.13b, respectively. We want briefly discuss the LSDA results before going to the GGA results. For $x = 0.5000$ it is recognised that order reduces the MCA by a factor of three to an amount about $\Delta E_{mca} \approx 200$ μeV/(3d · atom) (for the L1$_0$ structure) as compared to the results obtained with VCA, see Figure 4.13. However, the position of the peak for the largest MCA (L1$_0$: $a = 2.571$ Å) coincides with the position of the peak observed with VCA ($a = 2.556$ Å). The EAVG revealed the same order of magnitude for the MCA as observed for the L1$_0$ structure, but the peak was shifted to slightly

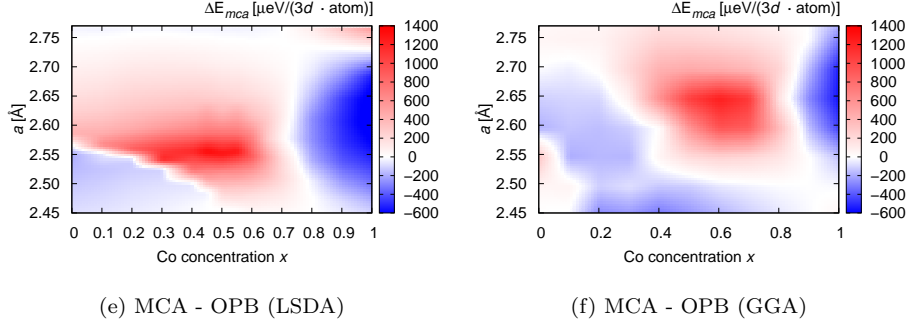(e) MCA - OPB (LSDA) (f) MCA - OPB (GGA)

Figure 4.12: The same notation as in Subfigures 4.12a and 4.12b is used.
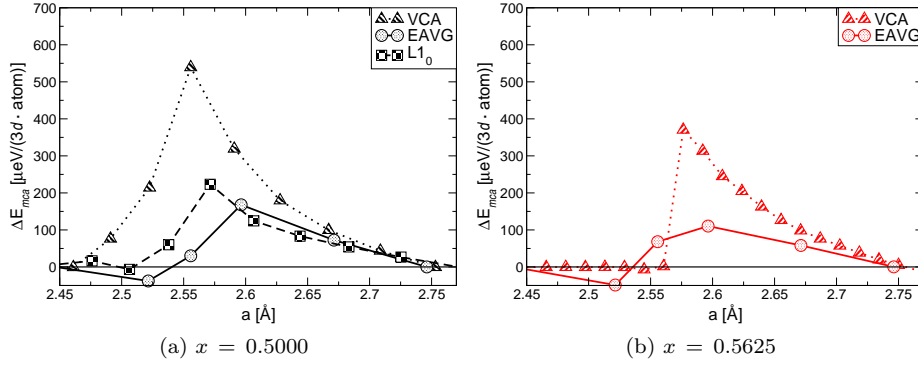

(a) $x = 0.5000$ (b) $x = 0.5625$

Figure 4.13: The MCA of FeCo alloys with respect to the lattice parameter a, obtained with LSDA. The MCA was calculated for $x = 0.5000$ by VCA, by EAVG, and L1$_0$-type structure (Figure (a)) and for $x = 0.5625$ by VCA, and by EAVG (Figure (b)). The MCA is given in μeV/(3$d \cdot$ atom).

higher parameters $a = 2.596$ Å. For $x = 0.5625$ a reduction from $\Delta E_{mca} \approx 400$ μeV/(3$d \cdot$ atom) (VCA) to $\Delta E_{mca} \approx 120$ μeV/(3$d \cdot$ atom) (EAVG) was recognised, see Figure 4.13b.

The anisotropy energies were calculated in GGA for the 5 concentrations: $x = 0.5000, 0.5626, 0.6250, 0.6875$, and 0.7500. The MCA was observed using VCA, EAVG, and L1$_0$ structure or L1$_2$ structure (for the respective x), see Figure 4.14. Figure 4.14a visualises that the L1$_0$ structure ($x = 0.5000$) yielded anisotropy energies of 500 μeV/(3$d \cdot$ atom) being larger than the related anisotropy energies obtained using VCA and EAVG, as opposed to LSDA. In VCA one finds the MCA about 400 μeV/atom and for EAVG 170 μeV/(3$d \cdot$ atom). The peak position of the largest MCA were in best agreement for the EAVG ($a = 2.639$ Å) and VCA with ($a = 2.650$ Å). For the L1$_0$ phase the peak was lowered to $a = 2.600$ Å. Similar conclusions for the MCA are drawn for $x \in (0.5625, 0.6250, 0.6875$, and $0.7500)$, see Figures 4.14e - 4.14d, respectively. We observed the general tendency that the MCA was lowered by a factor of three for the EAVG as compared to the MCA results obtained with VCA, which was to that respect also seen in LSDA.
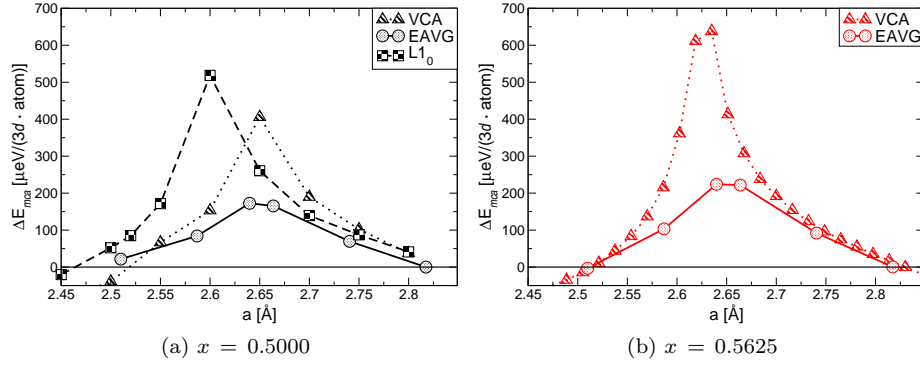
(a) $x = 0.5000$

(b) $x = 0.5625$

Figure 4.14: The MCA of FeCo alloys with respect to the lattice parameter a, obtained using GGA. The MCA was calculated for $x = 0.5000$ by VCA, by EAVG, and L1$_0$-type structure (Figure (a)), for $x = 0.7500$ by VCA, by EAVG, and L1$_2$-type structure (Figure (e)), for $x \in (0.5625, 0.6250, 0.6875)$ by VCA, and by EAVG (Figures (b), (c), and (d), respectively). The MCA is given in μeV/($3d \cdot$ atom).

(c) $x = 0.6250$

(d) $x = 0.6875$
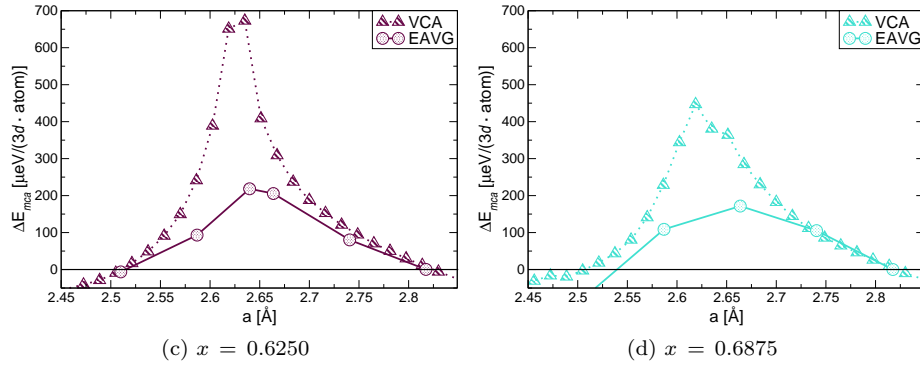
Figure 4.14: The same notation as in Subfigures 4.14a and 4.14b is used.

We remark, that for a concentration of $x = 0.7500$ the L1$_2$ phase yielded slightly smaller MCA energies than the corresponding values in VCA. However, both energies were of the same order of magnitude. The lowest anisotropy energies were found for EAVG. We recognised two maxima of the MCA in Figure 4.14e, obtained by using VCA. The first maximum was at $a = 2.619$ Å ($a = 2.586$ Å) and the second was located at $a = 2.667$ Å ($a = 2.741$ Å), where the values without brackets correspond belong to VCA and the values inside the brackets belong to EAVG. The first maxima was confirmed by the results obtained using L1$_2$ structure, but the second was not verified for the ordered structure.

On the basis of the total energy data obtained using VCA (Figures 4.7a and 4.7b) the in-plane stress σ_1 was calculated applying Eqn. (4.8). Figures 4.15a and 4.15b present the obtained values, in LSDA and in GGA, respectively. In order to minimise amount of the presented data, only the lowest
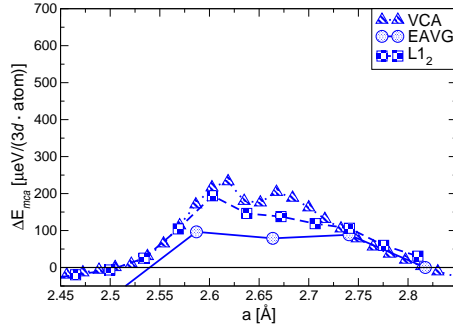
(e) $x = 0.7500$

Figure 4.14: The same notation as in Subfigures 4.14a and 4.14b is used.
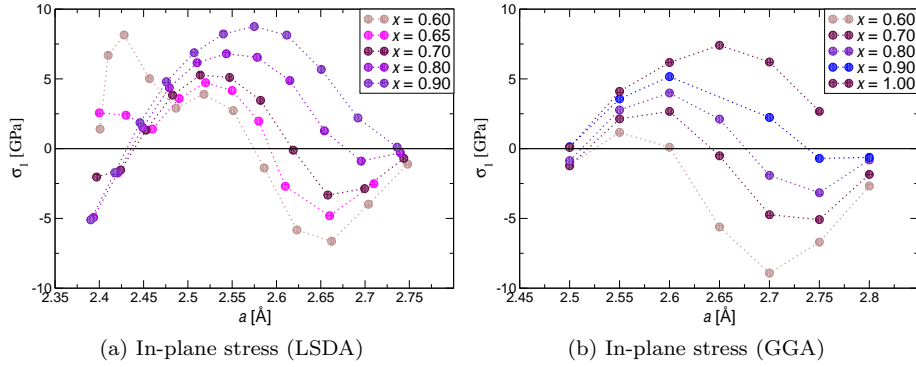
(a) In-plane stress (LSDA)

(b) In-plane stress (GGA)

Figure 4.15: In-plane stress σ_1 of FeCo alloys with respect to the lattice parameter a for Co concentrations $x \geq 0.6000$. The in-plane stress σ_1 was calculated according to Eqn. (4.8), obtained with LSDA (Figure (a)) and GGA (Figure (b)), respectively. Both used XC-potentials yielded vanishing in-plane stress by about $a = 2.600$ Å for a concentration $x = 0.6000$ accompanied by a large MCA (Figure 4.12).

obtained σ_1 for LSDA and for GGA are shown. In case of LSDA the stress for $x = 0.6000, 0.6500, 0.7000, 0.8000$ and 0.9000 was calculated. For large concentrations, $x \geq 0.9000$, we recognised two regions with vanishing in-plane stress. The two regions correspond to the FCC phase ($a \approx 2.450$ Å) and the BCC phase ($a = 2.750$ Å. For lower concentrations there was found a third region with zero stress. The zero-crossing was depending on the x, we found for the confining cases: $a = 2.680$ Å (for $x = 0.8000$), and $a = 2.580$ Å (for $x = 0.6000$). This stress-free region corresponds to the instable BCT state. The largest stress σ_1 was found in the lattice parameter range of $a = 2.550 - 2.600$ Å in dependency on x.

The situation was qualitatively the same for GGA. However, the first meta-stable phase ($\sigma_1 = 0$) was found at already $x = 0.9000$, see Figure 4.7b. The stresses σ_1 for $x = 0.6000$ obtained with GGA are smaller than the corresponding values obtained with LSDA. We conclude that the instable BCT state (zero in-plane stress) was strongly depending on the concentration x, in LSDA and

Table 4.12: Suggested parameter-space of FeCo alloys. The parameter range was cho-
sen such that the MCA shows huge PMA and a large saturation magneti-
sation **S** accompanied by an almost vanishing in-plane stress σ_1.

	LSDA	GGA
a [Å]	$2.530 - 2.570$	$2.570 - 2.670$
x [%]	$40 - 60$	$50 - 70$

GGA. Slightly larger lattice parameters a were observed using GGA as compared
to LSDA, for which vanishing in-plane stress σ_1 was found. Furthermore, we
emphasise that the observed region, which revealed a flat total energy (almost
vanishing in-plane stress σ_1), shows also a very large anisotropy energy ΔE_{mca}
(see previous discussion). Table 4.12 summarises the interesting parameters in
the (a, x)-space of FeCo alloys.

Experimental growth on this particular a and x area could be feasible due
to the very small in-plane stress. Table 4.13 provides the lattice mismatch for
experimentally accessible substrates. Experiments on Cu and Rh deliver the
largest lattice mismatch of $7.054 - 9.681\%$ and $2.182 - 4.982\%$, respectively.
Experiments on Pd(001), Ru(001), and Rh(001) have already been done [136–
140]. Luo et al. measured by means of magnetisation experiments for Fe$_{0.4}$Co$_{0.6}$
alloys grown on Pd(001) a MCA of $\triangle E_{mca} = 108$ μeV/($3d \cdot$ atom) [137]. The
comparison of the experimentally observed MCA with our obtained results at
$x = 0.6000$ and corresponding lattice parameter a with respect to LSDA or
GGA using VCA, EAVG, and ordered L1$_0$-type and ordered L1$_2$-type structures
yielded the same order of magnitude for the MCA. The MCA obtained with
respect to VCA does not reproduce previously applied calculations [82, 83] for
this choice of x and lattice parameter a.

The authors predicted for this x and a a MCA of about $300 - 400$ μeV/($3d$
$\cdot$ atom), which is $3 - 4$ times larger than the experimentally observed. The in-
clusion of relaxation yields MCA energies closer to the experimentally measured
(LSDA: 0 μeV/($3d \cdot$ atom), and GGA: 82 μeV/($3d \cdot$ atom)) results of the MCA
in comparison with calculations which neglect relaxation.

Magnetisation experiments as discussed above were already applied on sub-
strates with smaller lattice parameters a than for Pd, e.g. on Ir and on Ru. It
was shown that the anisotropy energies exceed the amount observed for Pd, but
an exact quantification of the MCA was not feasible due to the fact that the
experimental arrangement did not allow a fully magnetisation of the sample.
For a quantification of the anisotropy, experiments involving stronger magnets
than presently have been used are needed. Based on the results for the in-plane
stress and the magneto-crystalline anisotropy energy, we recommend experi-
ments on even smaller lattice parameters than already examined. Based on our
DFT results we suggest experiments on Cu(001), see Figure 4.16. Figure 4.16
presents the MCA in dependency on a for $x = 0.6000$. It is clearly visible that
the lattice parameter of Cu(001) ($a_{exp} = 2.556$ Å) was in best agreement with
our predicted substrate lattice parameter ($a_{lsda} = 2.557$ Å) in LSDA which
combines low stress, a large MCA, and a large saturation magnetisation, see
Table 4.13. In GGA, the maximal MCA was shifted to larger lattice parameters
($a_{gga} = 2.650$ Å). However, this value was still lower than the substrate lattice
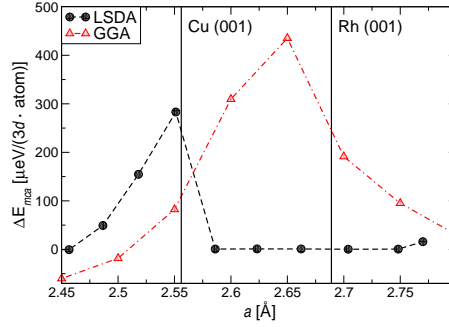
Figure 4.16: The MCA of FeCo alloys for $x = 0.6000$ using LSDA and GGA. The MCA was calculated by VCA. The experimental substrate lattice parameters for Cu(001) and Rh(001) are visualised as black vertical lines. Shown are the calculated MCA energies without using the spline method (text), in contradiction to Figure 4.12 in which the spline method was applied. The MCA is given in $\mu eV/(3d \cdot atom)$.

Table 4.13: Lattice misfit of FeCo alloys between several shown substrates and related BCC lattice parameters for a concentration $x = 0.600$. The optimised BCC lattice parameters were $a_{bcc,lsda} = 2.750$ Å and $a_{bcc,gga} = 2.830$ Å, the lattice misfit $f = 1 - \left(a_{bcc,lsda/gga}/a_{substrate,exp}\right)$ is given in %. The experimental BCC lattice parameters are taken from [141]. Experiments have already been applied on substrates going from Pt to Rh.

Substrate metal	a_{exp} [Å]	f_{lsda} [%]	f_{gga} [%]
Cu	2.556	7.054	9.681
Rh	2.689	2.182	4.982
Ru	2.704	1.673	4.452
Ir	2.715	1.273	4.064
Pd	2.750	0.000	2.827
Pt	2.775	−0.909	1.943

parameter for Rh(001) ($a_{exp} = 2.689$ Å) on which are present experiments have been conducted.

4.2.6 LSDA vs. GGA

A further discussion about the discrepancies seen between the LSDA and GGA results for the L1$_0$ structures is presented to clarify the physical correct behaviour of the MCA. Figure 4.17a and 4.17b show the calculated μ_s and μ_l in dependence on the lattice parameter a, for LSDA and GGA respectively. Calculations involving only LSDA will be called *pure LSDA* and calculations involving only GGA will be called *pure GGA*. Spin and orbital magnetic moment were higher in case of GGA, as well as the relaxed volumes than in LSDA. It was clearly visible that the μ_s and μ_l drop down at a lattice parameter of 2.578 Å in LSDA, while in GGA the moments remained almost constant during

the whole Bain Path. Additionally, the largest ΔE_{mca}, obtained for VCA (red line) and L1$_0$ structure (blue line), is drawn. The largest MCA observed for the L1$_0$ phase in LSDA was found at $a = 2.578$ Å. By going to smaller lattice parameters lower values of the μ_s and μ_l were obtained. The magnetic break-down was also observed by the VCA calculations. However, the VCA results yielded a smaller lattice parameter $a = 2.555$ Å for which the largest MCA was found, see Figure 4.17a. In GGA, this behaviour was reversed. The largest L1$_0$ MCA was at $a = 2.615$ Å, and VCA $a = 2.650$ Å. It is well-known, that LSDA overbind and deliver smaller lattice parameters than corresponding GGA calculations. Besides, magnetism is generally overestimated in GGA.

In order to rule one or two of the previous possibilities (overbinding in LSDA, and overestimation of magnetism in GGA) out, we performed LSDA calculation with relaxed volumes, which were obtained from GGA calculations (denoted: LDA-GGA), see Figure 4.17c. The break-down of the magnetism for a pure LSDA calculation, as seen in Figure 4.17a, disappeared. Thus, the magnetic moments were non-zero for all presented lattice parameters. Comparison with pure GGA calculations yielded slightly lower magnetic moments than observed from LDA-GGA calculations. Furthermore, the correct adjustment of the corresponding MCA maxima (red and blue lines), as obtained for pure GGA calculations, was recognised. We conclude that the break-down of the magnetism was caused by over-binding in LSDA. GGA and LSDA yielded for the same volumes the same magnetic solution. We remark that the ground-state of Fe (FCC) shows magnetic order [142]. Despite our calculations are not able to reflect the correct experimentally observed situation (which is a spin density wave), the results obtained with GGA were FM while the results using LSDA were non-magnetic for Fe (FCC). The results for the calculations using solely LSDA were already discussed in Subsection 4.2.5.

Figure 4.18 visualises the anisotropy energies calculated solely in LSDA (denoted as: LDA) and calculated in LSDA using the optimised volumes in GGA (denoted as: LDA-GGA). The LSDA calculations using relaxed GGA volumes clearly demonstrate that the ordered L1$_0$ structure possess an anisotropy energy of $\Delta E_{mca} = 690$ μeV/(3d $\cdot$ atom), which was of the same order of magnitude as we found for the calculations using solely GGA. The anisotropy energy was enlarged by a factor of almost 4 as compared to the results observed solely in LSDA for the L1$_0$ phase. Both, LDA and LDA-GGA, calculations yield comparable magnitudes of the MCA when using VCA. However, the position of the maximum MCA did not coincide for both methods applied, which was mainly caused by the fact that GGA generates larger volumes than LSDA, as seen in Subsection 4.2.5. As opposed to the statement for pure LSDA calculations, we come to the conclusion that order has a deep impact on the magnitude of the anisotropy. The largest MCA was found for L1$_0$ structures. A similar behaviour was reported for FePt alloys [120].

4.2.7   Summary

We demonstrated the influence of volume relaxation as well as the impact of disorder on FeCo alloys by performing first-principle calculations. Our calculations confirmed that FeCo alloys exhibit high uniaxial MCA and magnetic moments. The MCA was experimentally verified to be 0.1 meV/(3d $\cdot$ atom) [137]. The corresponding saturation magnetisation was 2 μ_B/(3d $\cdot$ atom). The anisotropy

(a) LSDA

(b) GGA
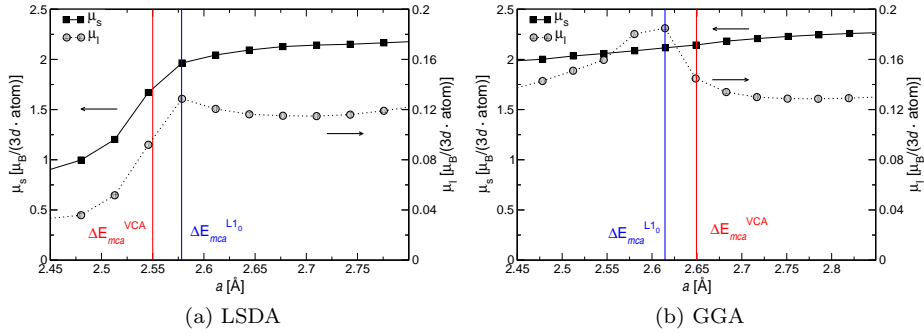
Figure 4.17: Spin (μ_s) and orbital (μ_l) magnetic moments of FeCo alloys in dependency on the lattice parameter a and $x = 0.5000$, obtained with $L1_0$ type structure. Both moments were calculated in LSDA - using relaxed volumes obtained with LSDA (Figure (a)), in GGA - using relaxed volumes obtained with GGA (Figure (b)), and in LSDA - using relaxed volumes obtained with GGA (Figure (c)). The spin moment is denoted as ■—■ and the orbital moment is denoted as ○··○. We mark the MCA which was found to be largest along the EBP using VCA and $L1_0$ type structure by ΔE_{mca}^{VCA} and $\Delta E_{mca}^{L1_0}$. The magnetic moments are given $\mu_B/(3d \cdot$ atom).

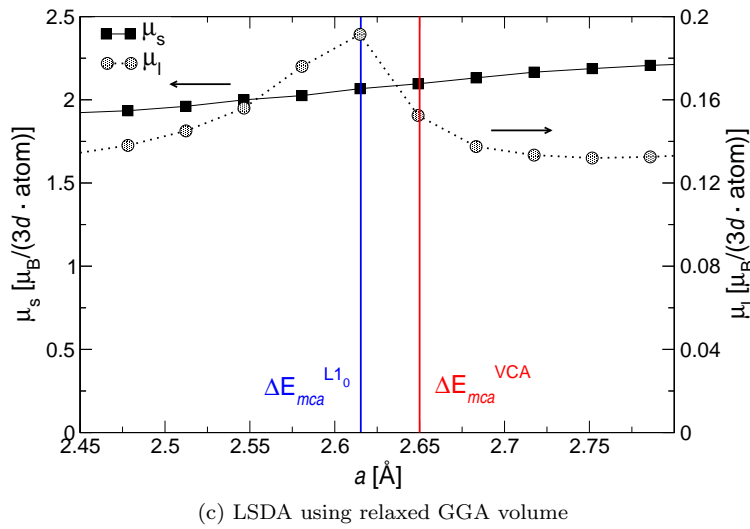(c) LSDA using relaxed GGA volume

Figure 4.17: The same notation as in Subfigures 4.17a and 4.17b is used.
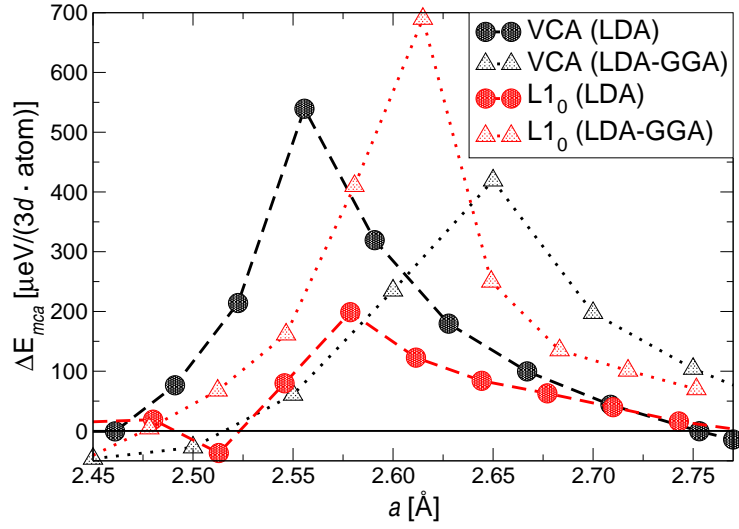
Figure 4.18: MCA of FeCo alloys with respect to the lattice parameter a and $x = 0.5000$, obtained with VCA and L1$_0$ type structure. The MCA was calculated in LSDA - using relaxed volumes obtained with LSDA (LDA) and in LSDA - using relaxed volumes obtained with GGA (LDA-GGA). The MCA is given in μeV/($3d \cdot$ atom).

energies was computed of the order of 0.2 meV/($3d \cdot$ atom) (EAVG) and 0.3 meV/($3d \cdot$ atom) (EAVG + OPC).

A reasonable agreement of the anisotropy energies with recent experiments in literature was observed. The VCA results provided much higher anisotropy energies than the EAVG results. This is based on the fact that VCA represents a perfectly ordered structure with equal atomic charge at every lattice site, and thus overestimates the MCA by $3 - 4$ times. L1$_0$ structure delivered 0.6 meV/($3d \cdot$ atom) (1.3 meV/($3d \cdot$ atom)), applied OPC is written in brackets. We conclude that order increases the MCA as similarly observed in FePt alloys [120]. We compared LSDA with GGA calculations. We come to the conclusion that the magnetic collapse, seen in the pure LSDA calculations, was only based on different observed relaxed volumes between LSDA and GGA, respectively. The LSDA results using relaxed GGA volumes yielded the same magnetic properties as we observed for calculations using solely GGA. This statement is emphasised by the fact that GGA gives the more realistic bond lengths for Fe(BCC) and Co(FCC). For that reason we believe that LSDA is for that system inappropriate to describe magnetic properties.

Volume relaxation lowered the optimum substrate lattice parameter by 5 % compared with previous non-relaxed calculations. Secondly, volume relaxation broadened the interesting range of the chemical composition x as compared with previous calculations. Thirdly, there was no sizeable effect seen on the MCA caused by volume relaxation. Furthermore, an almost vanishing in-plane stress was found at $a \approx 2.600$ Å, combining a huge anisotropy and very flat energy region. We suggest to examine experiments on Cu(001). According to the general requested thermal stability ratio, which demands: $K_U V / k_B T \cong 50 - 70$, there are needed up to $2000 - 3000$ atoms for one bit at drive

operating temperatures about $T \sim 340$ K to maintain sufficient signal stability (considered was L1$_0$ FeCo with $K_U \approx 0.7$ $meV/(3d \cdot$ atom)).

Finally, there was recognised no qualitatively change in μ_s and the MCA by applying OPB.

5

Uranium Compounds

The actinides demanded the effort of experimentalists and theoreticians to understand their properties for more than 50 years. The correct description of the ground-states of actinides by DFT has recently attracted a lot of interest [143]. For instance, one big challenge deals with the understanding of the different ground-states under pressure for Pu [144–150] and Cm [151, 152]. And even their compounds exhibit many fascinating properties which are related to the extraordinary nature of the $5f$ electrons. In that respect, the behaviour of the $5f$ electrons may change by varying the actinide material from one to another (from bonding, localised to bonding, delocalised and vice versa) [146, 153]. Thus, one of the fundamental questions concerning actinide materials addresses whether their f states are localised or delocalised. A common way to classify the degree of localisation of the f electrons is done by comparing experimental spectroscopies, and theoretical calculations.

The electronic states in transition metals are regarded as delocalised, in contrast to the lanthanides for which the $4f$ electrons are considered as localised. In actinides the f electrons show both, localised character for the light actinides [154–156] up to Pu and a delocalised character for the heavy actinides. In that respect the light actinides are well described by LSDA [157, 158]. For the heavy actinides a Mott localisation between Pu and Am is seen [159], which is caused by the decrease of f bandwidth and the increase of the intra-atomic Coulomb energy.

Figure 5.1 compares the experimental equilibrium volumes of $5d$ transition metals, lanthanides, and actinides. The progress of the equilibrium volume while going through the series is related with the localisation-delocalisation transition of the $5f$ electrons. For the light actinides the equilibrium volumes decrease parabolically indicating that the valence electrons contribute to the bonding (delocalised). The equilibrium volume remains more or less constant behind Pu as a function of the atomic number and resembles the equilibrium volume of the lanthanides. In that respect the electrons for the heavy actinides are considered not to contribute to the bonding and hence are localised (Mott transition [160–162]). In summary, the actinides are located in between the delocalised transition metals and the localised $4f$ systems. We describe here the situation in metallic solids. In non-metallic compounds it can be more complex.

In this thesis only uranium compounds were considered. In those compounds the magnetism is mainly driven by the Uranium atoms. According to Hund's second rule the spin momentum μ_s couples anti-parallel to the orbital momentum μ_l. A second fundamental question in actinides deals with the question
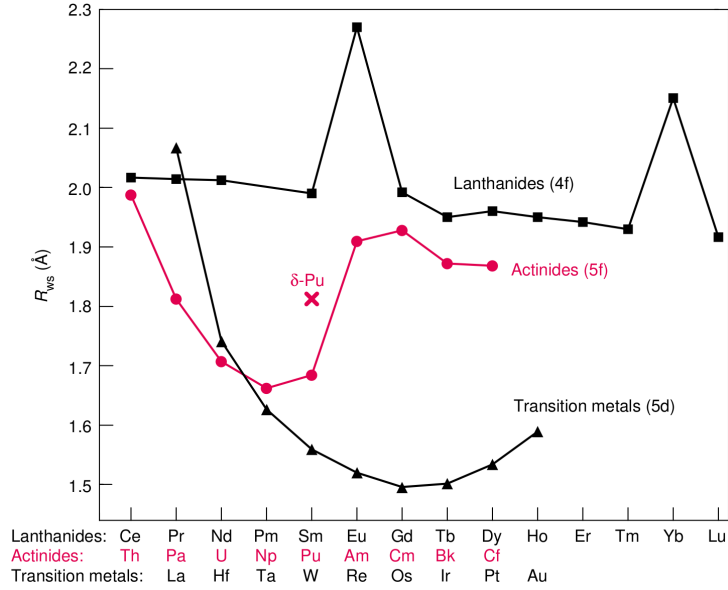
Figure 5.1: Experimentally observed Wigner-Seitz radius of elements of $4f$, $5d$ shells. The Wigner-Seitz radius is defined as the radius of the volume per atom in a solid: $r_{WS} = (3/4\pi\ V)^{1/3}$, where V is the equilibrium volume of the primitive unit cell. The anomalies for Eu and Tb are due to occupation instabilities of the $4f$ shell. The radius is given in Å. The figure is taken from [167].

whether magnetism is stable or not. An empirical rule defines the critical nearest neighbour distance of 3.400 Å for the An-An[1] distance for which magnetism sets in, which is known as the Hills limit [163]. According to this limit magnetism is non-stable for An-An distances smaller than 3.400 Å due to delocalised $5f$ electrons, and for An-An distances larger than 3.400 Å magnetism can occur based on much more localised $5f$ electrons in the actinide compounds.

A large diversity of interesting and unusual features in actinide compounds can appear due to the interplay with localisation and delocalisation. To that respect we mention the discovery of heavy fermion behaviour of actinide compounds [164], the discovery of unconventional superconductivity in PuCoGa$_5$ [165] and the problem of finding the hidden order in URu$_2$Si$_2$ [166] which has been a big mystery for more than 20 years now for both theoreticians and experimentalists.

This chapter is organised as follows: We present in Section 5.1 the classes of uranium monopnictides and monochalcogenides. For both series a large number of theoretically and experimentally investigations are around and thus our presented results are easy to classify with other results. In Section 5.2 we discuss magnetic properties of ten binary UM$_2$ compounds, where $M \in 3d$. Section 5.3 presents the results for the Compounds UAsSe and USb$_2$.

---

[1] "An" stands for any specific element of the actinides.

(a) ferromagnetic   (b) anti-ferromagnetic
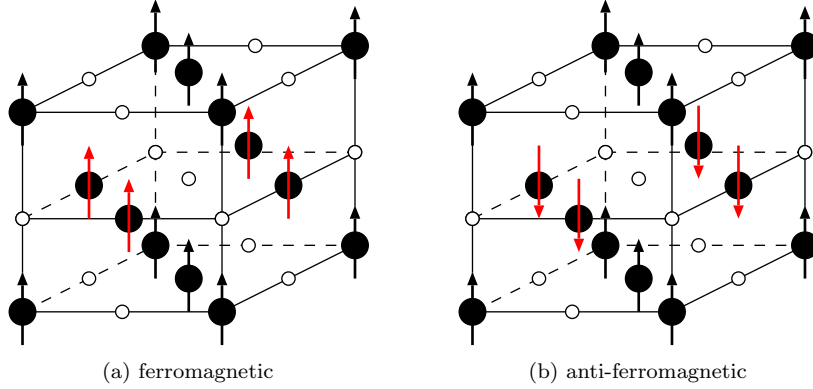
Figure 5.2: Magnetic and crystallographic structure of UX compounds. The arrows indicate the spin, ● denotes a Uranium atom, and ○ denotes a X atom. In case of FM the easy axis points along [111]-direction (Subfigure (a)), in case of AFM type-I the magnetisation points alternating along the [001]-direction (Subfigure (b)).

5.1 UX, with $X = (N, P, As, Sb, O, S, Se, and\ Te)$

In the following chapter we want to discuss the electronic properties of the UX compounds. This class of compounds is one of the most widely studied actinide compounds. All of them crystallise in the rock-salt structure. While the monochalcogenides (X = S, Se, and Te) show a *ferromagnetic* (FM) order, all monopnictides (X = N, P, As, and Sb) have a type-I *anti-ferromagnetic* (AFM) structure, see Figure 5.2. The corresponding ordering temperatures are tabulated in Table 5.3. Indeed, transitions into multi-**k** AFM structures are possible, however we have taken only type-I AFM structures into account in our calculations. No structural information about UO was found, that is why we used the FM setup for that compound, like for the other monochalcogenides.

Above T_C the FM compounds crystallise in cubic symmetry in the paramagnetic state. A rhombohedral lattice distortion was observed when decreasing the temperature [168]. Magnetisation measurements [169, 170] and neutron scattering analysis on US [171–174] and on UTe [170] revealed that these materials possess an extremely large MCA [173]. The easy axis of the three FM compounds observed to align along the [111] direction. All monopnictides keep the cubic structure when passing T_N with the magnetisation pointing along the [001] direction with alternating sign. As previously told, one is often interested in the question whether the f electrons are more localised or itinerant. For that reason investigations of the ordered magnetic U moment were analysed under pressure. In this connection rhombohedral lattice distortions under pressure were observed for the monopnictides [175, 176].

All calculations were conducted with FPLO, version 9.00-34. We used 48^3 k-points in the BZ for the k-space integrations. The XC-potentials was treated in LSDA. The default basis was used in all our calculations. The site-centered potentials and densities were expanded in spherical harmonic contributions up to $l_{max} = 4$. All calculations were done in the full relativistic mode. Since relativistic effects become more important in $5f$ shells, we took only that ver-
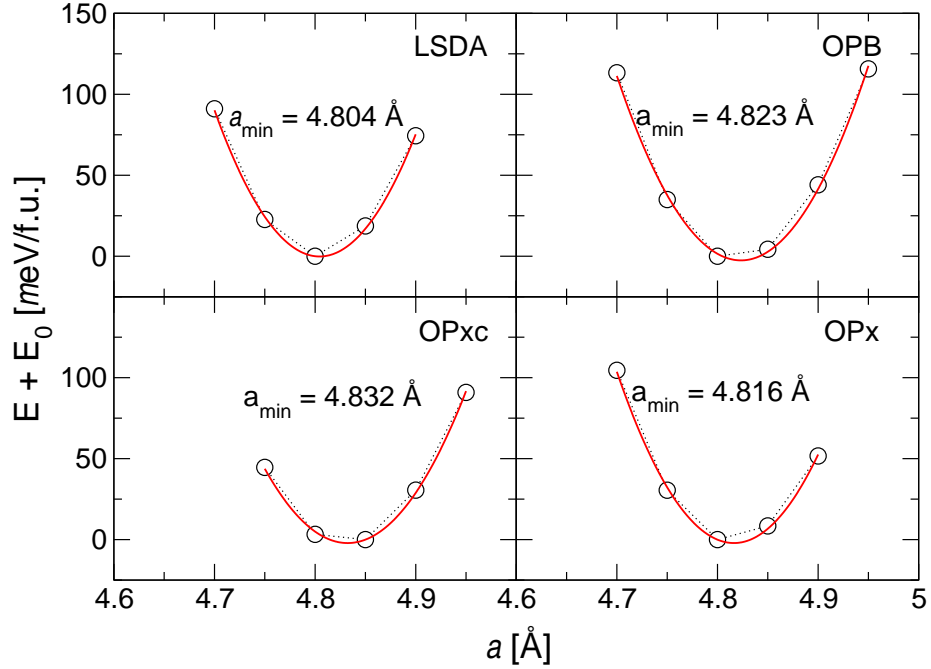
Figure 5.3: Total energy with respect to lattice parameter a, obtained within LSDA. The total energy was calculated by pure LSDA, OPB, OPxc, and OPx. The experimentally observed lattice parameter is $a_{exp} = 4.890\,Å$. The notation is as follows: $\bigcirc\cdots\bigcirc$ - calculated points, —— - polynomial fit of the order 4. The total energy is given in $meV/f.u.$

sions of OPE into account in which the Kohn-Sham-Dirac states are projected onto local SR orbitals. In Chapter 3 large differences for the OPC energies were seen between using either NR local orbitals or using SR local orbitals. Hence, making use of NR local orbitals for OPE is here not justified. Finally, OPC was applied solely to the $5f$ states. All other settings were kept as default.

We had to use two different arrangement for either a FM setup or a AFM type-I setup. The FM setup used spacegroup 225. The following Wyckoff positions have been applied: $N = (0., 0., 1/2)$, and $U = (1/2, 1/2, 1/2)$. For the AFM type-I setup the spacegroup was chosen to be 123. The following Wyckoff positions have been applied: $U_1 = (0., 0., 1/2)$, $U_2 = (1/2, 1/2, 0.)$, $N_1 = (0., 0., 0.)$, and $N_2 = (1/2, 1/2, 1/2)$.

5.1.1 UN

UN is a metal and measured as type-I AFM with a Néel temperature of 53 K [177–180]. Experimental verification of the total moment by about 0.75 ± 0.1 $\mu_B/$(f.u.)can be found here [177]. Several studies concerning the crystallographic structure were performed [168, 181, 182]. Recent investigations observed two rhombohedral distortions under pressure [176]. The structure at zero pressure was observed to be undistorted, which will be used in the calculations.

In order to analyse the influence of the OPC on the lattice parameter, we

Table 5.1: Comparison of total energy differences relative to the ground-state, where we have used $\Delta E = E_{structure}$ - E_{fm}. We assumed following ordering: *non-magnetic* (NM), FM, AFM type-I. The energies are given in *me*V/f.u. All results using FPLO were obtained with LSDA, the results using Wien2k were obtained with GGA. In both studies experimental lattice constants were applied.

Magnetic Structure	FPLO	FPLO + OPB	FPLO + OPxc	FPLO + OPx	Wien2k [194]
NM	21.0	112.0	144.3	77.6	76.3
FM	0.0	0.0	0.0	0.0	0.0
AFM type-I	7.6	−9.0	−10.9	−3.1	16.1
AFM type-II	——	——	——	——	27.6

calculated the optimised lattice parameter a without OPC, with OPB, with OPxc, and with OPx. The resulting curves are shown in see Figure 5.3. The optimum lattice parameter obtained for the pure LSDA calculation underestimates the measured lattice parameter by about two percent ($a_{exp} = 4.890$ Å.). It is seen that when applying OPC, the optimum lattice parameter is slightly increased by about $0.3 - 0.6\%$. But still, the optimised lattice parameters were smaller than the measured lattice parameter. As a conclusion all OPC show minor influence on the optimum lattice parameter.

Despite UN is a AFM with order type-I, most calculations in literature assume a FM or even a NMS [53, 72, 183–193]. In fact, the only works to our knowledge assuming AFM ordering (AFM type-I and AFM type-II[2]) in their calculations are to be found in [111, 194]. The wrong ground-state was found when using Wien2k with GGA [194]. In contradiction to experiment the authors found a FM ground-state. We performed first-principles calculations using FPLO with and without OPC. We assumed either a non-magnetic, a FM, and an AFM type-I order. The results are listed in Table 5.1. The calculations without OPC predict a FM ground-state and basically confirm previous results. So far, no explanation is given, why the ground-state observed either in GGA or in LSDA differs from the measured one. I was shown by means of neutron scattering analysis that in UN both AFM and FM instabilities are present [195]. Recently, theoretical support was given by using Fermi liquid theory [196] suggesting that UN is a weak itinerant AFM. The presence of both FM and AFM instabilities might explain why both, FPLO and Wien2k, calculations yielded a FM ground-state, using either LSDA or GGA, respectively. When OPC is applied on top of LSDA the experimentally observed AFM type-I state is calculated to be lower in energy than the FM state. This statement was found to be independent on the particularly chosen OPC functional. The calculations assuming a non-magnetic state turned out to be higher in energy than the magnetic states, either the FM or the AFM configuration, respectively.

Figure 5.4a shows the DOS for either a FM order or an AFM type-I order. The contribution of the $5f$ states at the Uranium site is drawn as shadow, either in black (FM) or in red (AFM type-I). We see that the DOS is formed solely by the $5f$ states. Both magnetic orderings yielded similar DOS resulting in an

---

[2]AFM type-I is defined in Figure 5.2b, and AFM type-II is explained in [194].

(a) DOS
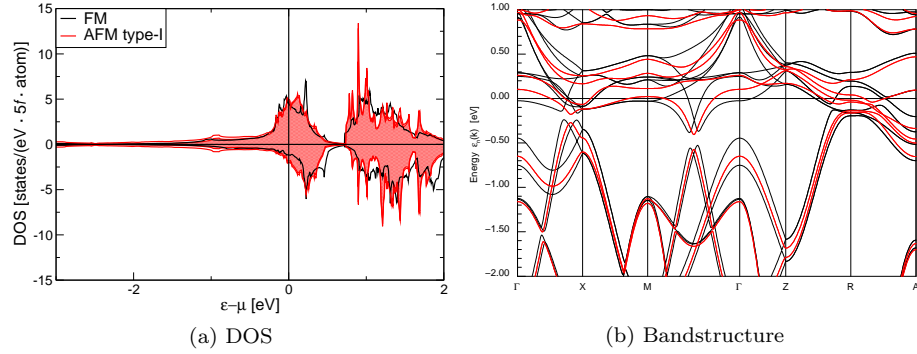
(b) Bandstructure

Figure 5.4: DOS (Figure (a)) and band structure (Figure (b)) of UN obtained with respect to a FM and a AFM type-I setup, respectively. The results were calculated using LSDA. We use the following notation: —— - FM order (U_{5f} DOS and band structure), and —— - AFM type-I order (U_{5f} DOS and band structure). The DOS is given in states/(eV · $5f$ · atom). The eigenergies $\epsilon_n(k)$ are given in eV.

unaffected spin moment μ_s, see Table 5.2. Figure 5.4b reveals differences in the band structure in dependency on the magnetic ordering. The same notation as for the DOS is used. Both magnetic orderings yielded band structures which resemble each other. However, if one takes a closer view at the band structure, differences at some peculiar points were observed. These differences are mainly reflected by a splitting of the AFM bands. The splitting is very pronounced at the X, the Γ, and the R point.

Figure 5.5 presents the Fermi surface for the two orderings. A reoccupation of the bands is seen at the M point, at which the band no. 65 is shifted above ϵ_f. We see that for the AFM type-I ordering, we obtained two-fold degenerated bands, labelled with band index 61 and 63. From Figures 5.5d - 5.5g it is clearly visible that these two bands are split in the FM case. We note that a Lifshitz transition [197] occurs in band no. 61, when going from the AFM state to the FM state. This band forms an almost two dimensional cylinder in the AFM set-up, where the Z point is the centre of the cylinder (Figure 5.5a). The cylinder is transformed into two hole-like spheres around the Z point (Figure 5.5d).

In Table 5.2 we list the calculated and experimentally observed spin, orbital, and total magnetic moments at the uranium site for UN. The pure LSDA results yield an total magnetic moment of almost zero for both the FM and AFM state, meaning that the spin magnetic moment und the orbital moment are cancelling each other. This result was confirmed by LAPW+lo calculations [194]. Non full-potential LMTO calculations [53, 111] yield non-vanishing total magnetic moments much closer to the experimentally observed than the full-potential correspondent. OPC drastically increases the orbital magnetic moment and pushes the total magnetic moment closer to experiment. We note that the total magnetic moments obtained for the AFM state are typically larger by $12 - 25$ % than the total magnetic moments calculated for the FM state. Computations using RPA on top of LSDA follow the same trend for the spin, orbital, and total magnetic moment as seen when applying OPC. When considering only the calculations using FPLO and AFM order, it is found that the magnetic moment is in best agreement with experiment for OPx. However, the calculated

(a) Band 61   (b) Band 63   (c) Band 65

(d) Band 61   (e) Band 62   (f) Band 63   (g) Band 64
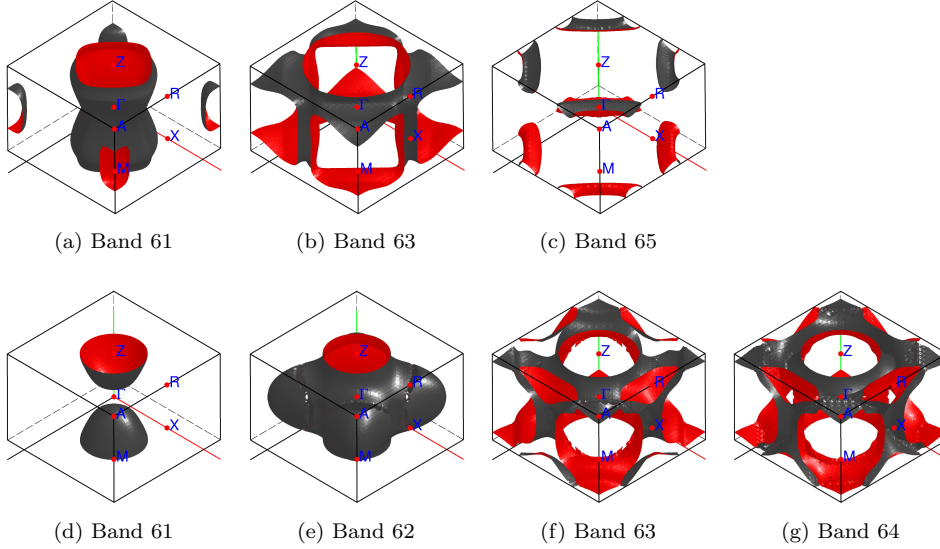
Figure 5.5: Fermi surface of UN calculated with LSDA. Figures (a) - (c) correspond to the AFM type-I configuration, and Figures (d) - (g) assume a FM configuration.

magnetic moment applying the FM order differs from experiment only by 2.7 %.

In Figure 5.6 we visualise the effect of the different applied OPC using FPLO on the DOS. The presented results were calculated for the FM state, because the DOS was not strongly altered between the two distinct magnetic orders (FM or AFM). The DOS obtained with LSDA was already discussed previously. We see, that the exchange splitting is most pronounced for OPxc on top of LSDA, and the smallest splitting is obtained for pure LSDA. OPx on top of LSDA yielded the smallest splitting of all applied OPC. OPB and OPx yielded splittings in between OPxc and LSDA. There is more overlap between OPB and OPx recognised than recognised between OPB and OPxc. These conclusions are corroborated by the results for the magnetic moments, see Table 5.2.

5.1.2 UX

We proceed by a systematical investigation of the uranium monopnictides and monochalcogenides in order to get an overview of the magnetic properties along the whole series. All presented data were calculated by assuming a FM ordering which is motivated by the fact that the DOS and the magnetic moments are stable against the magnetic order (FM or AFM), see Figure 5.4 and Table 5.2. In Table 5.3 we present the measured [198] and theoretically optimised lattice constants. First, we compare the nearest neighbour distance r_{NN} among all studied compounds, see also Table 5.3. According to Hills limit UN and UO are closely located at the transition point from delocalisation to localisation. All other studied compounds are well separated to consider the f electrons as localised. By comparing the optimised lattice constants with the measured quantities, we see different trends between the monopnictides as for the monochalcogenides On

Table 5.2: Magnetic moments of UN. The magnetic moments were calculated with LSDA. OPC is applied to the $5f$ states at both uranium sites. The LMTO results are taken from [53, 111], and the LAPW+lo are taken from [194]. The experimentally observed total magnetic moment is $\mu_t^{exp} = 0.75 \pm 0.10$ [177]. All magnetic moments are given in $\mu_B/(5f \cdot \text{atom})$.

FM			
Method	μ_s	μ_l	μ_t
FPLO	-0.98	0.97	-0.02
FPLO + OPB	-1.29	2.28	0.99
FPLO + OPxc	-1.50	2.68	1.19
FPLO + OPx	-1.30	2.03	0.73
LMTO	-0.99	1.49	0.50
LAPW+lo	-0.86	0.85	-0.01
AFM type-I			
FPLO	-0.81	1.08	0.28
FPLO + OPB	-1.23	2.49	1.26
FPLO + OPxc	-1.46	2.90	1.44
FPLO + OPx	-1.22	2.26	1.04
LMTO	-1.04	1.64	0.60
LMTO - RPA	-1.08	2.04	0.96
LMTO - cRPA	-1.12	2.28	1.16

Figure 5.6: DOS of UN obtained with respect to FM order. The DOS is calculated using either LSDA or LSDA with additional OPC applied to the U $5f$ states. The DOS is given in states/(eV $\cdot$ atom).
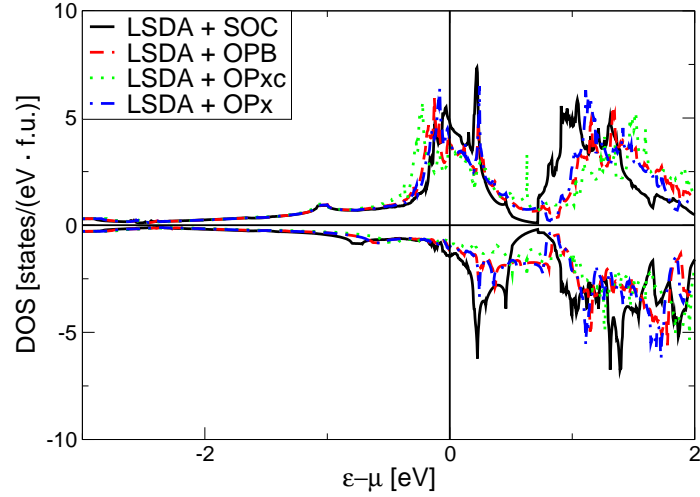
Table 5.3: Lattice parameters of UX, $X \in$ (N, P, As, Sb, O, S, Se, and Te). The lattice parameters were obtained using LSDA. All presented lengths are given in Å. The function f is defined as in Table 4.13 and is given in %. The measured lattice constants and the Temperatures $T_{C,N}$ are taken from [198]. The Temperatures are given in K.

X	a_{exp}	a_{lsda}	f_{lsda}	r_{NN}	T_N	X	a_{exp}	a_{lsda}	f_{lsda}	r_{NN}	T_C
N	4.889	4.809	1.636	3.457	53	O	4.922	4.794	2.601	3.480	— —
P	5.584	5.469	2.059	3.948	125	S	5.482	5.392	1.669	3.876	177
As	5.777	5.703	1.281	4.085	127	Se	5.730	5.692	0.668	4.052	160
Sb	6.191	6.090	1.658	4.378	213	Te	6.124	6.091	0.542	4.330	104

the one hand, we observed no clear tendency for the optimised lattice parameter of the monopnictides, where a constant underestimation of the measured lattice constant by $1.3 - 1.7$ % was found. On the other hand, we found a decrease for the lattice misfit when increasing the mass of the monochalcogenides, resulting in a underestimation of the measured lattice constant by only 0.5 %. However, the localisation of the f electrons when going from S to Te can not simply be answered by a increasing of the masses.

The calculated DOS are displayed in Figure 5.7. We obtained metallic solution for all studied compounds. The f electrons were closely located around the Fermi level. The f bands were found in between lower lying s, p electrons from the corresponding X atom and upper lying very broaden d bands, which can mainly attributed to the uranium site. From the DOS we see that the $s, p - f$ hybridisation is more pronounced for the monopnictides as for the monochalcogenides. Furthermore, it is recognised that the s, p electrons were shifted to higher energies (closer to the f electrons) when increasing the mass of the X atom for both, the monopnictides (Figs. 5.7a, 5.7c, 5.7e, and 5.7g) and monochalcogenides (Figs. 5.7b, 5.7d, 5.7f, and 5.7h), respectively.

A "pseudo-gap" was found for UN at around 0.70 eV [192]. Among the monochalcogenides a pseudo-gap was observed for US, USe, and UTe [199]. We clearly found the existence of a pseudo-gap for UN, UP, and UAs (insets in Figure 5.7). Contrarily in USb, where we obtained only a small pseudo-gap at 0.58 eV. The pseudo-gap was in case of the monochalcogenides not so conspicuous as it was for the monopnictides. For UO and US no clear formation of a gap is seen. Only for USe (at 0.44 eV) and UTe (at 0.39 eV) we found a tiny pseudo-gap as obtained in the case of USb.

In Table 5.4 we list the calculated magnetic moments of the considered UX compounds. The moments were calculated for a spin quantisation axis pointing along the [001]- or the [111]-direction, for the monopnictides and the monochalcogenides, respectively. The results show that the spin moment was calculated with opposite sign to the orbital moment. It was observed that the magnetism in all compounds was stemming mainly from the U site. In LSDA, there was found for UN and UO an almost exact cancellation of the calculated spin and orbital moments yielding a total moment of almost zero. A systematically increasing of the spin moment was observed, when increasing the masses. Larger orbital moments were also found, for larger masses, however the increase of the orbital moments was stronger that the increase of the spin

(a) UN   (b) UO
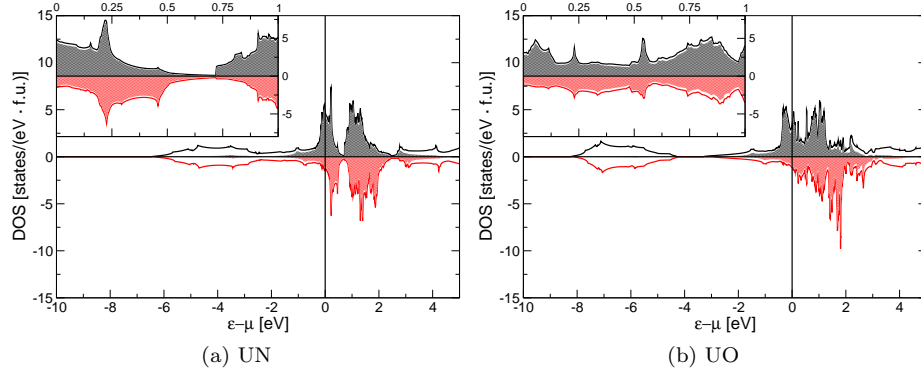
Figure 5.7: DOS of UX, $X \in (N, P, As, Sb, O, S, Se,$ and Te). The DOS was cal-
          culated using LSDA. We use the following notation: — - total DOS, ▨ -
          U$_{5f}$ DOS, with black and red for the spin up and the spin down channels,
          respectively. The DOS is given in states/(eV · atom). The inset in the left
          upper corner of every subfigure displays a zoomed DOS. The same units
          are applied for the insets as used for the subfigures.

moments resulting in a non-vanishing total moment for the other monopnic-
tides and monochalcogenides. Comparison with experimental data for the UN
compounds revealed that in LSDA the calculated total moment were too small
about 97 %, and for $X = P$, As, Sb, S, Se, and Te the calculated total moments
were too small about $50 - 70$ %.

   The total moment is better reflected when applying OPC on top of LSDA.
However, the comparison of experimentally observed spin and orbital moments
and the corresponding calculated quantities yield that both theoretical values
are overestimated when using OPC. It seems that both quantities having the
same error, so that the sum fits the measured total moment. The spin moment
is already perfectly described in LSDA for the monopnictides and slightly over-
estimated when applying OPC, at least in the case of UAs. For the monochalco-
genides the experimentally observed spin moment is already doubled in LSDA,
and even larger when applying additional OPC.

   The orbital moment is underestimated about 30 % in LSDA for UAs, 10 %
for US, 13 % for USe, and 1 % for UTe. The orbital moment is overestimated
about $10 - 25$ % when OPC is applied on top of LSDA for UAs. For the
monochalcogenides, the overestimation of the orbital moment is about $35 -
60$ %. It seems, that orbital moment is better reflected using solely LSDA for
the heavier monochalcogenides, as USe and UTe, as for the lighter one, as US.

   The total moment calculated with OPx is found to be in best agreement
with experiment for UN, UAs, US, and USe. When going to USb and UTe
the total moment is underestimated even when applying OPC. The last results
suggest that the f electrons of the heavier monochalcogenides are may be to
much localised to treat them in itinerant, as LSDA does.

   A collection of calculated magnetic moments reported so far is listed in
Tables 5.5 and 5.6 . The comparison of our data with that reported in literature
reveals that our calculations are in good agreement with those results previously
conducted. However, it is seen that calculated moments can scatter by a factor of

(c) UP (d) US

Figure 5.7: DOS of UX, $X \in (N, P, As, Sb, O, S, Se,$ and $Te)$. The same notation as in Subfigures 5.7a and 5.7b is used.

(e) UAs (f) USe

Figure 5.7: DOS of UX, $X \in (N, P, As, Sb, O, S, Se,$ and $Te)$. The same notation as in Subfigures 5.7a and 5.7b is used.

two evaluated within the same method, demonstrating that the results are basis (LMTO, ASW, LCAO, . . .) and method (LSDA, LSDA + OPB, . . .) dependent.

In Table 5.7 we discuss calculated MCA energies for the monopnictides and monochalcogenides. An unusual high MCA for cubic systems was found for the the monochalcogenides [170, 172]. In fact, the large anisotropy was at least in case of the monochalcogenides attributed to a rhombohedral lattice distortion [175], which simultaneously occurs with the magnetic phase transition. The monopnictides were also characterised by a large anisotropy [212]. In contrast to the monochalcogenides there were no structural distortions seen in the magnetically ordered state [213, 214]. A detailed overview of the magnetic structure of UX compounds can be found in [215]. The strong anisotropy in the monopnictides is manifested in a strong anisotropic exchange or the rearrangement of the domain walls when applying an external field [213].

So, for the UX compounds the MCA was defined as in Eqn. (4.1) using $\hat{\mathbf{n}}_1 =$

---

[3]These calculations were performed using larger lattice parameters than the experimentally observed.
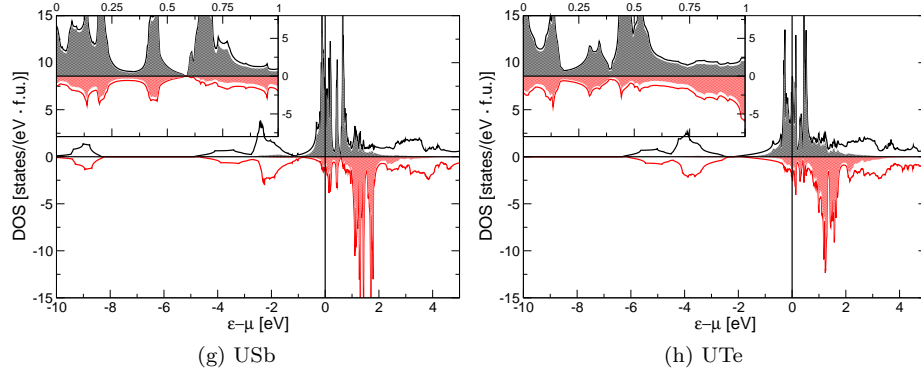
(g) USb

(h) UTe

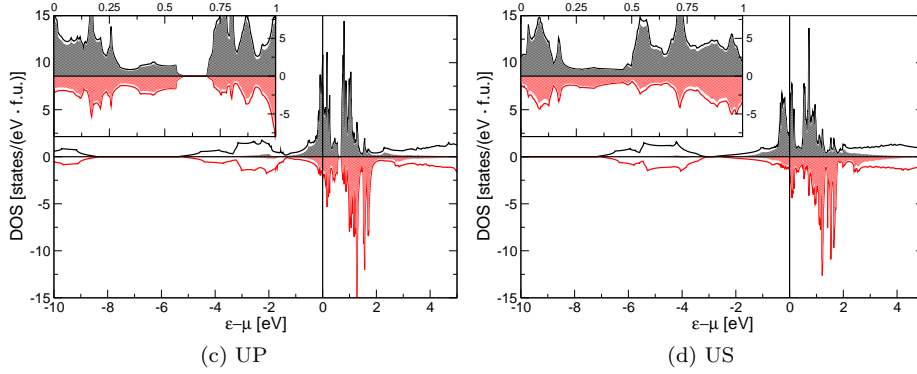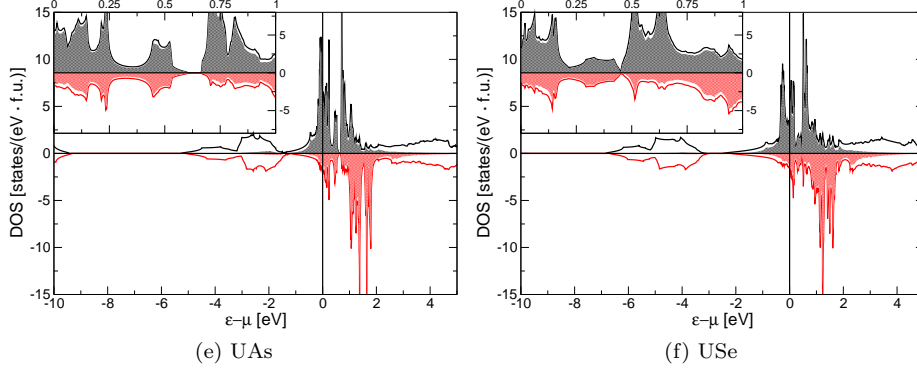Figure 5.7: DOS of U*X*, *X* ∈ (*N, P, As, Sb, O, S, Se,* and *Te*). The same notation as in Subfigures 5.7a and 5.7b is used.

Table 5.4: Magnetic moments of U*X*. The magnetic moments were calculated with LSDA. Additional OPC was applied to the 5*f* states at the uranium sites. The spin quantisation axis was chosen along the [001]- or [111]-direction, for the monopnictides or the monochalcogenides, respectively. The experimental observed total magnetic momenta are taken from [198, 200, 201]. All magnetic moments are given in $\mu_B/(5f \cdot \text{atom})$.

Method	X	μ_s	μ_l	μ_t	X	μ_s	μ_l	μ_t
FPLO	N	-0.99	0.97	-0.02	O	-1.78	1.96	0.18
FPLO + OPB		-1.30	2.29	0.99		-1.91	3.28	1.36
FPLO + OPxc		-1.50	2.69	1.19		-2.06	3.79	1.73
FPLO + OPx		-1.30	2.03	0.73		-1.94	3.19	1.25
EXP		$--$	$--$	0.75		$--$	$--$	$--$
FPLO	P	-1.50	2.03	0.53	S	-1.85	2.42	0.56
FPLO + OPB		-2.00	3.70	1.71		-2.02	3.77	1.75
FPLO + OPxc		-2.30	4.26	1.96		-2.22	4.26	2.03
FPLO + OPx		-2.08	3.66	1.57		-2.07	3.74	1.67
EXP		$--$	$--$	1.70		-0.98	2.68	1.70
FPLO	As	-2.01	2.67	0.66	Se	-1.95	2.72	0.78
FPLO + OPB		-2.32	4.27	1.95		-2.21	4.17	1.96
FPLO + OPxc		-2.55	4.77	2.22		-2.42	4.64	2.22
FPLO + OPx		-2.39	4.26	1.87		-2.28	4.20	1.92
EXP		-1.92	3.84	1.92		-1.09	3.11	2.01
FPLO	Sb	-2.37	3.37	1.00	Te	-2.19	3.23	1.04
FPLO + OPB		-2.58	4.85	2.27		-2.44	4.55	2.11
FPLO + OPxc		-2.77	5.25	2.48		-2.66	5.00	2.34
FPLO + OPx		-2.65	4.90	2.24		-2.53	4.60	2.07
EXP		$--$	$--$	2.82		-1.01	3.27	2.26

Table 5.5: Calculated magnetic moments of UX, $X \in (N, P, As,$ and Sb) taken from literature. All calculations were performed by applying LSDA, those calculations not using LSDA are specially tagged. All magnetic moments are given in $\mu_B/(5f \cdot \text{atom})$. The spin quantisation axis were chosen along the [001]- or [111]-direction, for the monopnictides or the monochalcogenides, respectively. Following abbreviations are used: *modified ASW* (MASW), *orbital Hartree-Fock* (OHF) and *mixed basis* (MB).

X	Method		μ_s	μ_l	μ_t
N	LMTO [53]		-0.99	0.49	-0.50
	LMTO [111]	AFM type-I	-1.04	1.64	0.60
		AFM type-I, RPA	-1.08	2.04	0.96
		AFM type-I, cRPA	-1.11	2.29	1.18
	LAPW [194]	FM, GGA	-0.86	0.85	-0.01
P	LMTO [202]	FM	-2.18	2.66	0.48
		FM, OPB	-2.43	3.85	1.43
	LMTO [111]	AFM type-I	-1.70	2.73	1.03
		AFM type-I, RPA	-1.70	2.94	1.25
		AFM type-I, cRPA	-1.70	3.36	1.66
As	LMTO [202]	FM	-2.32	3.00	0.68
		FM, OPB	-2.44	4.12	1.68
	LMTO [111]	AFM type-I	-1.97	3.18	1.21
		AFM type-I, RPA	-1.98	3.23	1.25
		AFM type-I, cRPA	-1.94	3.85	1.91
Sb	LAPW [203]	AFM-type I (single-**k**), non-collinear	-2.15	3.48	1.33
		AFM-type I,(double-**k**), non-collinear	-2.00	3.50	1.50
		AFM-type I,(double-**k**), non-collinear	-1.84	3.42	1.58
	MASW [204]	AFM-type I (single-**k**), non-collinear, OPB	-2.20	4.26	2.06
		AFM-type I (triple-**k**), non-collinear, OPB	-2.24	4.46	2.22
	LMTO [202]	FM	-2.37	3.50	1.13
		FM, OPB	-2.60	4.57	1.97
	LMTO [111]	AFM type-I	-2.28	3.83	1.55
		AFM type-I, RPA	-2.27	3.93	1.66
		AFM type-I, cRPA	-2.22	4.40	2.18

[001] and $\hat{\mathbf{n}}_2 = [111]$[4]. For the monopnictides the correct easy axis was obtained only for UN and UP (only in LSDA, without OPC). All other calculations yield the wrong easy axis. The correct easy axis was found for all monochalcogenides. An increasing of the MCA is observed for increasing mass when going through both series. To our knowledge the only experimentally quantification of the

---

[4]A FM order was assumed to calculate the MCA for all considered compounds.

Table 5.6: Calculated magnetic moments of UX, $X \in (O, S, Se, \text{and } Te)$ taken from literature. Same notation as in Table 5.5 is used.

S	LMTO [205] [3]	FM	−1.53	2.14	0.60
		FM, U(OP)	−1.48	3.21	1.72
		FM, U	−1.35	3.42	2.07
	ASW [206]	FM	−1.50	2.60	1.10
	LMTO [72]	FM	−2.10	3.20	1.10
		FM, OPB	−2.20	4.00	1.80
	LMTO [207]	FM, OHF	−1.51	3.12	1.61
	LAPW [208]	FM	−1.60	2.33	0.73
	LMTO [202]	FM	−1.87	2.39	0.52
		FM, OPB	−2.06	3.58	1.51
	LAPW [209]	FM	−1.70	2.58	0.88
	LCAO [210]	FM	−1.83	2.40	0.57
	LMTO [111]	FM	−1.88	2.92	1.04
		FM, RPA	−1.85	3.05	1.20
		FM, cRPA	−1.83	3.33	1.50
	LCAO [211]	FM	−1.69	2.59	0.90
		FM, MB	−1.72	2.62	0.82
Se	LMTO [205] [3]	FM	−1.75	2.54	0.79
		FM, U(OP)	−1.65	3.65	2.00
		FM, U	−1.96	4.61	2.65
	ASW [206]	FM	−1.70	2.90	1.20
	LMTO [72]	FM	−2.40	3.40	1.00
		FM, OPB	−2.20	4.30	1.90
	LAPW [208]	FM	−1.94	2.92	0.98
	LMTO [202]	FM	−2.01	2.68	0.67
		FM, OPB	−2.27	3.89	1.62
	LAPW [209]	FM	−1.96	3.11	1.15
	LCAO [210]	FM	−1.92	2.71	0.57
	LMTO [111]	FM	−2.14	3.37	1.23
		FM, RPA	−2.10	3.44	1.34
		FM, cRPA	−2.07	3.74	1.67
	LCAO [211]	FM	−1.79	2.89	1.10
		FM, MB	−1.79	2.88	1.09
Te	LMTO [205] [3]	FM	−2.12	3.12	1.47
		FM, U(OP)	−1.91	4.09	2.17
		FM, U	−2.13	4.95	2.81
	ASW [206]	FM	−2.20	3.50	1.30
	LMTO [72]	FM	−2.60	3.40	0.80
		FM, OPB	−2.60	4.60	2.00
	LAPW [208]	FM	−2.22	3.42	1.20
	LMTO [202]	FM	−2.35	3.23	0.88
		FM, OPB	−2.60	4.26	1.66
	LAPW [209]	FM	−2.31	3.71	1.40
	LCAO [210]	FM	−2.11	3.18	1.07
	LMTO [111]	FM	−2.43	3.82	1.39
		FM, RPA	−2.40	3.84	1.43
		FM, cRPA	−2.33	4.11	1.77
	LCAO [211]	FM	−2.01	3.39	1.38
		FM, MB	−2.00	3.40	1.40

MCA for the UX compounds was given for US. Here, the experimental situation is rather controversial as results of extrapolation to 0 K vary from 7.3 meV [171] up to 86.0 meV [216]. The same ordering for the MCA energies as found for the orbital magnetic moments was obtained: LSDA $\leq$ OPx, OPB $\leq$ OPxc.

Table 5.7: MCA of UX. The MCA was calculated using LSDA. Calculations were performed assuming FM order for all compounds. The measured MCA energies for US are taken from [171, 216]. All MCA energies are given in meV/($5f$ atom).

Method	X	MCA	X	MCA
FPLO	N	-0.1	O	7.9
FPLO + OPB		-8.9		40.4
FPLO + OPxc		-6.8		43.7
FPLO + OPx		-6.0		37.3
EXP		$--$		$--$
FPLO	P	-0.1	S	10.5
FPLO + OPB		15.0		51.4
FPLO + OPxc		33.7		67.1
FPLO + OPx		16.9		49.4
EXP		$--$		$7.3 - 86.0$
FPLO	As	7.3	Se	15.9
FPLO + OPB		34.2		50.2
FPLO + OPxc		46.3		58.0
FPLO + OPx		37.2		47.9
EXP		$--$		$--$
FPLO	Sb	19.7	Te	15.4
FPLO + OPB		42.7		44.5
FPLO + OPxc		45.7		36.9
FPLO + OPx		44.6		41.0
EXP		$--$		$--$

5.1.3 Summary

We calculated magnetic moments of the ground-state of several UX compounds. First we investigated the ground-state of UN. For that purpose calculations applying either the FM or the AFM type-I order were conducted. The measured AFM ground-state was only obtained when using additionally OPC on top of LSDA.

Second, we investigated the class of UX compounds and showed the necessity of OPC to properly quantify the magnetic moments. We performed calculations using OPxc and OPx obtained with local SR, see Chapter orbitals 3. Applying OPC to the $5f$ states yielded much larger orbital momenta than obtained with pure LSDA. We demonstrated that the OPx yielded for this class of compounds magnetic moments much closer to experiments than OPxc. The results of OPB and OPx were comparable.

Third, we calculated the MCA for these two classes of compounds by assuming a FM order for these investigations. We observed the wrong easy axis for

UP, UAs, and USb. A possible explanation is that the experimentally obtained ground-state for these compounds is a non-collinear multiple-**k** ground-state. Our calculations only admitted a collinear AFM type-I order. In fact, the experimentally reported MCA for US was observed even for a non-distorted cubic structure. We saw, that the MCA calculated without applying OPC can be seen as an lower estimation. The calculations using OPC yielded MCA which turned out to be an upper estimation.

5.2 UM_2, with $M = (Sc,\ Ti,\ V,\ Cr,\ Mn,\ Fe,\ Co,\ Ni,$ $Cu,\ and\ Zn)$

5.2.1   Calculational Details

The class of UM_2 compounds with $M \in 3d$, having cubic Laves phase symmetry [217], is discussed as next. As opposed to the previously studied case, the magnetism here is not solely driven by the $5f$ states moreover become the $3d$ states important. Among this class, we mention UFe$_2$ which has been intensively studied since the late 1960s. UFe$_2$ is reported to order FM below 160 K with a low anisotropy similar to that of pure Fe. This compound has attracted interest due to the fact that the spin and orbital magnetic moment at the U site are almost cancelling each other leading to a magnetisation mainly stemming from the Fe site. In that respect, it is interesting to discuss the $d - f$ hybridisation along the series.

We used 24^3 k-points in the BZ for the k-space integrations. OPC was applied to the $5f$ states at the U site and to the $3d$ states at the $3d$ site. All other settings were as in Section 5.1 introduced. The following symmetry was applied: Spacegroup 227, Wyckoff positions $U = (1/8, 1/8, 1/8)$ and $3d = (1/2, 1/2, 1/2)$. Thus, the primitive cell contained 4 atoms of type M and 2 atoms of type U. We assumed the cubic structure in all our calculations in order to make consistent statements along the series. Nevertheless, it is known that UNi$_2$ crystallises in a hexagonal Laves phase [198]. Calculations assuming this symmetry can be found in [218]. In fact, structural informations for UM_2 with $M \in Sc,\ Ti,\ V,\ Cr,\ Cu,$ and Zn are to the best of our knowledge not existent, thus the calculations for these compounds show a hypothetical character.

5.2.2   Results

In Table 5.8 we list the theoretical and the experimental [219] lattice constants. We found a parabolic shape of the volume along the series, as similarly observed for the pure transition metals, indicating that the d electrons play a crucial role in this compounds. We used the calculated lattice constants to discuss the magnetic properties. In Table 5.8 are also shown the nearest neighbour distances for the d atoms (d$_{d-d}$) and U atoms (d$_{U-U}$). According to Hill's limit all but one (the only exception is USc$_2$) compounds exhibit itinerant f electrons, and should be non-magnetic. Only USc$_2$ is close to the border of having localised f electrons and magnetic order may occur.

In Table 5.9 we present the calculated magnetic moments obtained without and with applied OPC to the $3d$ states at the M sites and the $5f$ at the U site. We found a magnetic solution for $Sc,\ Mn,\ Fe,\ Co,\ Ni,\ Cu,$ and Zn
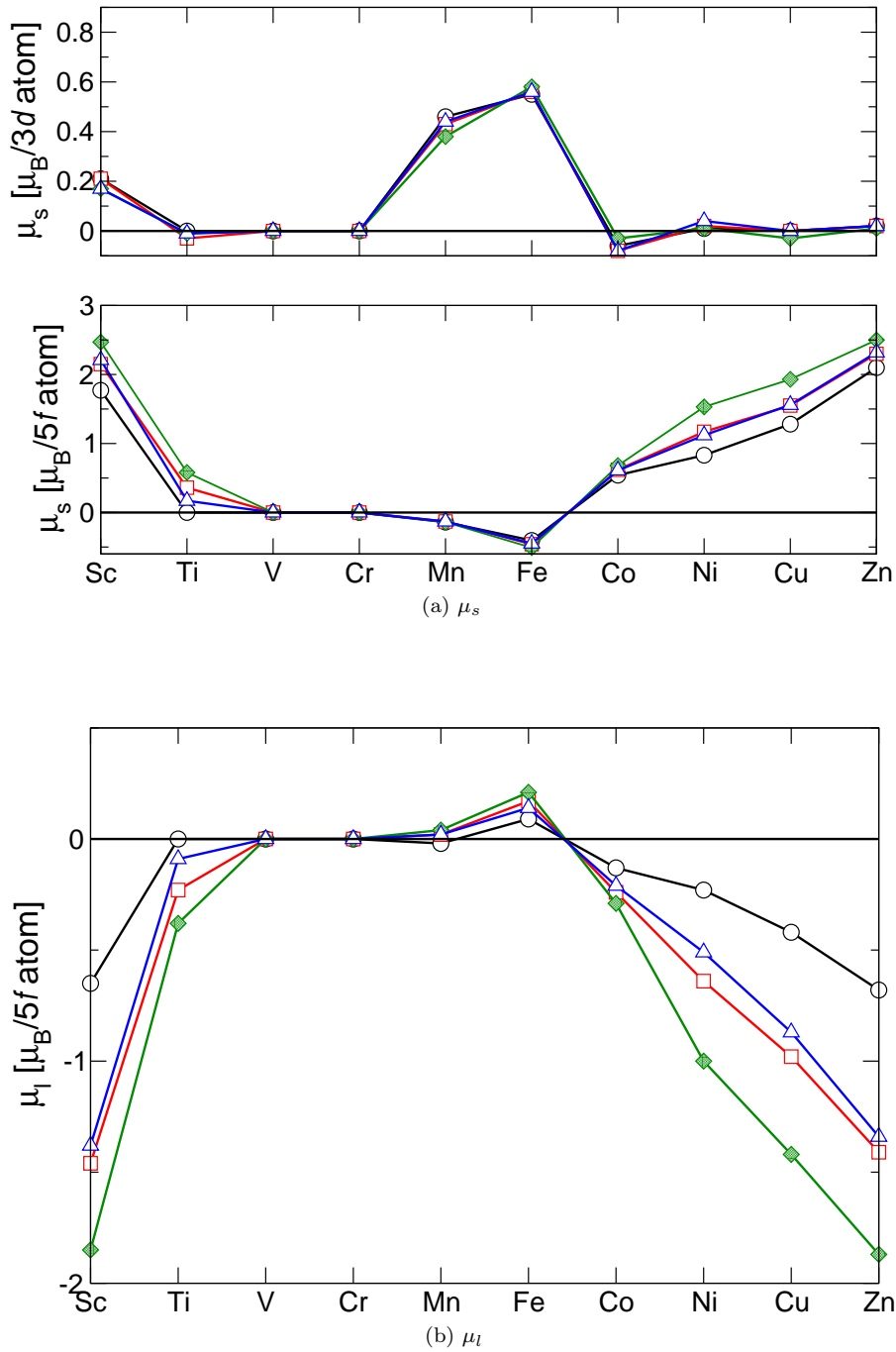
(a) μ_s

(b) μ_l

Figure 5.8: Magnetic moments of UM_2. The magnetic moments were obtained using LSDA. The magnetic moments are given in μ_B/atom. Notation as following: ○—○ - FPLO + SOC, □—□ - FPLO + OPB, ◆—◆ - FPLO + OPxc, and △—△ - FPLO + OPx.

Table 5.8: Lattice parameters UM_2 with $M = (Sc, Ti, V, Cr, Mn, Fe, Co, Ni, Cu,$ $and\ Zn)$. The optimised parameters were obtained using FPLO with LSDA. Measured lattice constants are taken from [219]. All lengths are given in Å.

M	a_{exp}	a_{lsda}	d_{d-d}	d_{U-U}
Sc	$--$	8.025	2.837	3.475
Ti	$--$	7.496	2.650	3.246
V	$--$	7.180	2.538	3.109
Cr	$--$	6.999	2.475	3.030
Mn	7.160	6.885	2.434	2.981
Fe	7.055	6.819	2.411	2.953
Co	7.000	6.815	2.409	2.951
Ni	$--$	6.899	2.439	2.987
Cu	$--$	7.081	2.503	3.066
Zn	$--$	7.353	2.600	3.184

in a pure LSDA + SOC calculation. Ti, V, and Cr are found to be non-magnetic. Applied OPC yield a magnetic state for Ti. V and Cr are found non-magnetic for all conducted calculations, even when OPC was applied. By comparing the orbital magnetic moments obtained with additional OPC, one recognises that the following relation was obtained for all calculated μ_l with the particular method: $\mu_l^{lsda} \leq \mu_l^{opx} \leq \mu_l^{opb} \leq \mu_l^{opxc}$. Interestingly, for the spin moment holds: $\mu_s^{lsda} \leq \mu_s^{opx}$, $\mu_s^{opb} \leq \mu_s^{opxc}$, which means that the ordering of the calculated orbital moments applying OPB and OPx was interchanged with respect to the ordering of the obtained spin moments for $M = Co, Ni, Cu,$ and Zn, respectively.

In Figure 5.8 we display the site resolved spin and orbital magnetic moments. A non-vanishing moment at the M site was found for Sc, Mn, and Fe. In the case of Sc the spin moment is found to align parallel to the spin moment at the U site. For Mn and Fe the spin moments are found to be anti-parallel. The largest spin moment at the M site was observed for Fe. A rapid disappearance of the spin moment at the M site was seen when going from Fe to Co. The spin moment at the M site was almost zero for $Co, Ni, Cu,$ and Zn. An increasing of the spin moment at the U site was observed for these compounds when going from Co to Zn. By comparing the calculated site resolved orbital moments in Figure 5.8b and the total orbital moments Table 5.9 one recognises that the orbital moment is carried only by the $5f$ states. In all cases the orbital moment is anti-parallel to the spin moment at the U site.

Figure 5.9a displays the occupation number in dependence on the d band filling. We recognised that the U occupation remains constant at $n_{5f} \approx 2.7$, which is lower than found in atoms with $n_{5f} = 3.0$, indicating a possible $d - f$ hybridisation or a possible charge transfer. The n_{6d} remains also constant, at $n_{6d} \approx 2.2$. For the d band we found a linear dependency of n_{3d} on the band filling. As a result the occupation number was of similar amount as obtained for pure $3d$ elements.

With the help of the Stoner criterion [220], which defines the instability of the non-magnetic state with respect to the FM state, we are able to relate the DOS at the Fermi level and the magnetic state of the U and M atoms. In our

Table 5.9: Magnetic moments of UM_2 with M = (Sc, Ti, V, Cr, Mn, Fe, Co, Ni, Cu, and Zn). The magnetic moments were obtained with LSDA. All moments are given in $\mu_B/$(f.u.).

M	Method	μ_s	μ_l	μ_t
Sc	FPLO	2.18	−0.65	1.54
	FPLO + OPB	2.57	−1.46	1.11
	FPLO + OPxc	2.90	−1.86	1.05
	FPLO + OPx	2.66	−1.38	1.28
Ti	FPLO	0.00	0.00	0.00
	FPLO + OPB	0.30	−0.23	0.07
	FPLO + OPxc	0.48	−0.38	0.10
	FPLO + OPx	0.15	−0.10	0.05
V	FPLO	0.00	0.00	0.00
	FPLO + OPB	0.00	0.00	0.00
	FPLO + OPxc	0.00	0.00	0.00
	FPLO + OPx	0.00	0.00	0.00
Cr	FPLO	0.00	0.00	0.00
	FPLO + OPB	0.00	0.00	0.00
	FPLO + OPxc	0.00	0.00	0.00
	FPLO + OPx	0.00	0.00	0.00
Mn	FPLO	−0.79	−0.01	−0.80
	FPLO + OPB	−0.73	−0.04	−0.77
	FPLO + OPxc	−0.69	−0.05	−0.77
	FPLO + OPx	−0.74	−0.03	−0.77
Fe	FPLO	−0.70	−0.11	−0.81
	FPLO + OPB	−0.67	−0.23	−0.90
	FPLO + OPxc	−0.65	−0.29	−0.94
	FPLO + OPx	−0.68	−0.19	−0.87
Co	FPLO	0.41	−0.13	0.28
	FPLO + OPB	0.47	−0.26	0.21
	FPLO + OPxc	0.51	−0.30	0.20
	FPLO + OPx	0.46	−0.22	0.24
Ni	FPLO	0.85	−0.23	0.62
	FPLO + OPB	1.22	−0.64	0.58
	FPLO + OPxc	1.61	−1.01	0.60
	FPLO + OPx	1.16	−0.52	0.64
Cu	FPLO	1.28	−0.42	0.86
	FPLO + OPB	1.54	−0.97	0.57
	FPLO + OPxc	1.93	−1.41	0.52
	FPLO + OPx	1.56	−0.86	0.70
Zn	FPLO	2.14	−0.68	1.47
	FPLO + OPB	2.34	−1.42	0.92
	FPLO + OPxc	2.54	−1.88	0.66
	FPLO + OPx	2.36	−1.34	1.02

(a) occupation number

(b) DOS(ϵ_f)
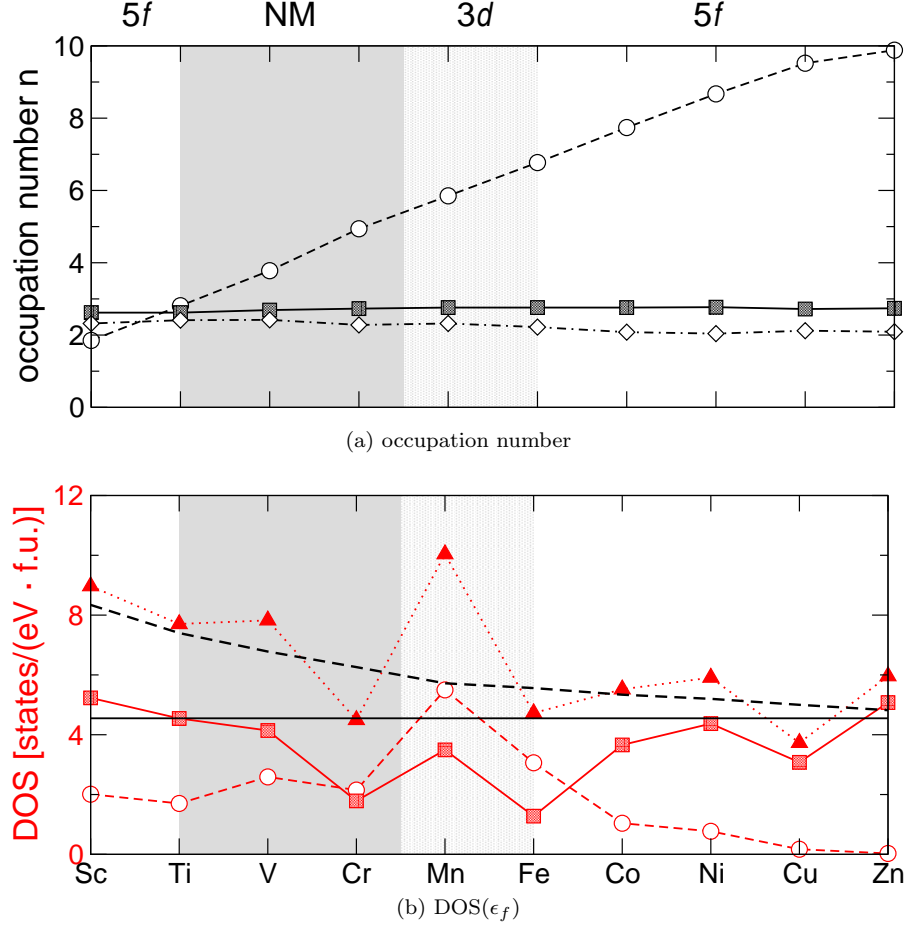
Figure 5.9: DOS(ϵ_f) and occupation numbers UM_2. The calculations were performed using LSDA and assuming a non-magnetic ground-state. The DOS is given in states/(eV · f.u.). Notation as following - DOS: ▲··▲ - total contribution, ■—■ - 5f contribution, and ○-○ - 3d contribution, occupation number: ■—■ - 5f contribution, ◇-◇ - 6d contribution, and ○··○ - 3d contribution. The dashed line $^{-\,-}$ denotes the critical DOS at ϵ_f to stabilise FM at the 3d site, the full line — denotes the critical DOS at ϵ_f at the U site. The shaded region marked ■ denotes non-magnetic solutions, and the shaded region marked □ denotes the region in which the magnetism is carried mainly by the 3d states.

calculations for the UM_2 compounds only the FM state was taken into account, thus the use of the FM Stoner criterion is justified. In Figure 5.9b we plot the total and partial DOS at the Fermi level in dependence on the $3d$ band filling for a non-magnetic calculation. First, we want to discuss the magnetic situation for every single atom. For that reason we calculated the critical DOS at ϵ_f for which magnetism is stabilised based on the exchange integrals given in [221] (dashed and dotted black lines in this figure). In case of the $3d$ atoms, the critical value was obtained only for Mn. In the case of Fe, for which we observed the largest spin moment at the $3d$ site, the Stoner criterion obviously is not ful-filled in contradiction to previous calculations [222]. The critical DOS was reached for Sc, Ni, and Zn at the U site for the $5f$ states. For the non-magnetic calculated compounds with Ti and V the Stoner criterion was almost ful-filled.

When applying the Stoner criterion for the whole primitive cell as demonstrated in [222], the Stoner criterion was for none of the compounds ful-filled. This is mainly caused by a lower DOS at ϵ_f as obtained in previous calculations for, e.g. UFe_2 and UCo_2 [222].

By comparing our results with available data in literature we want to classify our results. To our knowledge no experiments and calculations are reported on $M = Sc$, Ti, V, and Cr. Thus, our calculations show a predictive character. Magnetisation measurements suggested that UMn_2 possess an AFM structure which was explained by an anomaly of the susceptibility at 260 K [223]. However, a number of experiments disagreed with the previous paper. On the one hand no evidence of magnetic ordering was found [224] and on the other hand there was reported the absence of magnetic ordering [225, 226]. The same controversial situation is found for the theoretical calculations, where UMn_2 was said either to be paramagnetic [227] or to be FM [228]. Our calculations approve the calculations of [228] and hence are in disagreement with the experimental results. The question arises whether this discrepancy is caused by the structural transformations which occur at $T \sim 210 - 240\ K$ [226] or by the existence of meta-magnetic states.

The situation in UFe_2 is much clearer. Neutron measurements indicated a cancellation of the spin and the orbital momentum at the U site such that the magnetism is mainly driven from the Fe site [229]. This behaviour was qualitatively correct predicted by previous DFT calculations [222]. A collection of available data in literature is provided by Table 5.10. The cancellation of the magnetic moment at the U site was confirmed by neutron measurements [230] and XMCD [231]. All DFT calculations overestimate both, the spin and the orbital moment resulting in a slightly too large total magnetic moment at the U site. In fact, the only calculation yielding a vanishing total magnetic moment at the U site is the LMTO + U(OP) calculation [232]. The total magnetic moment was not affected by applying OPC, caused by a simultaneously increasing of μ_l and μ_s due to large SO coupling. Our calculated μ_s at site U and Fe were in best agreement with experiments, however the cancellation of μ_s and μ_l was not correctly reproduced. The calculated total magnetic moment agreed well with the measured moment. In fact, the only calculations yielding similar μ_t are these by KKR [233] and the LMTO [232], but the local magnetic site moment was overestimated in both cases.

UCo_2 has been reported to be an exchange-enhanced Pauli paramagnet [236, 237]. Theoretical foundation was given in [222]. According Figure 5.9b we confirm previous calculation, however the calculated state assuming FM order

Table 5.10: Magnetic moments UFe$_2$ from literature. The LMTO results are taken from [232, 234]. The KKR results are from [233]. Experiments are from [230, 231, 235]. All magnetic moments are given in μ_B/(f.u.).

Method	U			Fe			UFe$_2$		
	μ_s	μ_l	μ_t	μ_s	μ_l	μ_t	μ_s	μ_l	μ_t
LMTO	−0.71	0.47	−0.24	0.75	0.07	0.82	0.79	0.61	1.40
LMTO + OP	−1.03	0.88	−0.15	0.82	0.07	0.89	0.61	1.02	1.63
LMTO	−0.61	0.35	−0.26	0.68	0.06	0.74	0.75	0.47	1.22
LMTO + U(OP)	−0.71	0.72	0.01	0.71	0.08	0.79	0.71	0.88	1.59
LMTO + U	−1.83	3.08	1.25	1.14	0.20	1.34	0.45	3.48	3.93
KKR	−0.56	0.29	−0.27	0.69	0.06	0.75	0.82	0.41	1.23
FPLO	−0.41	0.09	−0.31	0.55	0.01	0.56	0.69	0.11	0.80
FPLO + OPB	−0.46	0.17	−0.29	0.56	0.03	0.59	0.66	0.23	0.89
FPLO + OPxc	−0.51	0.21	−0.30	0.58	0.04	0.62	0.65	0.29	0.94
FPLO + OPx	−0.45	0.14	−0.31	0.56	0.02	0.58	0.68	0.19	0.87
EXP (Neutrons)	−0.22	0.22	0.01	0.59	−−	−−	−−	−−	1.19
EXP (XMCD)	−0.20	0.21	0.01	−−	−−	−−	−−	−−	−−
EXP (MCS)	−0.20	−−	−−	0.52	−−	−−	−−	−−	−−

is lower in energy than the non-magnetic.

UNi$_2$ orders FM with a T$_C$ = 21 K [238] in the hexagonal MgZn$_2$ structure [239]. Neutron measurements indicated that the magnetism is mainly carried by the 5f electrons with a large orbital contribution which is cancelled by the spin contribution at the U site [240]. Magnetisation measurements approved a total magnetic moment of 0.08 μ_B/(f.u.) [239]. By fixing the spin magnetic moment at the measured amount with the FSM and taking into account both SO coupling and OPC, the calculated magnetic moments were in best agreement with the measured moments [218]. A simple band theoretical approach explaining why the magnetism in UFe$_2$ is driven by the 3d states, UCo$_2$ is paramagnetic, and UNi$_2$ is again FM, by using the 3d band filling as argument for this scenario, can be found in [241]. As seen by Figure 5.9 our results support these previous claimed arguments.

Following the trend of this simple band picture for UCu$_2$, this compound would again be close to the border of being FM like UCo$_2$ when the $f_{5/2}$ shell crosses ϵ_f. This is also seen in Figure 5.9b, where the DOS of the 3d states is almost zero at ϵ_f and the DOS is entirely made by the 5f states. From that point of view, we would expect a stronger polarisation at the U site accompanied by non-magnetic Cu, as seen in Figure 5.8. However, experiments observed a decreasing of the magnetisation and T_C by doping UNi$_2$ with Cu [241]. It seems that LSDA predicts the wrong ground-state, which may be remedied by including correlation effects.

5.2.3   Summary

We performed DFT calculations for the UM_2, $M \in 3d$, compounds. We calculated the magnetic moments with and without OPC using the optimised LSDA

Chapter 5. Uranium Compounds

lattice parameters. We obtained FM and non-magnetic order along the series. The magnetism was carried by two different electronic states. For Ti, Co, Ni, Cu, and Zn the magnetism was caused by the $5f$ electrons, while for Mn and Fe the magnetism was caused by the $3d$ states. When looking on Table 5.8 one concludes that localised magnetism is only possible for USc_2. Here, the U-U nearest neighbour distance is close to Hill's limit. For all other compounds the valence electrons can be seen as itinerant according to their nearest neighbour distances.

It could be shown, that the $3d$ occupation significantly contributes to the total DOS up to Co. As the $3d$ band is almost completely filled, the d band was moving to lower energies that ϵ_f. The DOS at the ϵ_f is then solely determined by the $5f$ states, which are responsible for the magnetism.

When applying OPC the orbital moment and the spin moment were increased such, that the total moment is unaffected by OPC. Discrepancies in obtaining the correct magnetic ground-state were found for Mn and Co, which turned out to be magnetic while being non-magnetic in experiment. The Stoner criterion was not ful-filled for the FM UFe_2, which was previously correctly predicted by DFT calculations [222]. This is mainly caused by a drastic decrease of the DOS at ϵ_f as opposed to previous calculations. A possible explanation is given by the fact that the previous investigations considered the experimental observed hexagonal structure, while a cubic structure was assumed in our calculations. The cancellation of orbital and spin moment in UNi_2 was not reproduced by LSDA and also not by additionally applying OPC.

5.3 UAsSe, USb_2

5.3.1 Calculational Details

The classes of uranium dipnictides and dichalcogenides are beautiful examples for exploring the dual nature of the $5f$ electrons. In that respect, by changing the pictogen or chalcogen anion radius, intriguing physical properties may evolve. In this way the inter-atomic distances are modified leading to more or less hybridisation of the $5f$ states with its surrounding. We calculated the magnetic properties for UAsSe and USb_2. UAsSe crystallises in the Pb-FCl crystal structure, despite USb_2 crystallises in the anti-Cu_2Sb structure (both have P4/nmm space group). UAsSe is a FM with [111]-direction of the easy axis and $T_C = 113~K$ [242]. USb_2 is a AFM with following stacking $+ - - +$, resulting that the magnetic unit cell is as twice as large as the crystallographic. The Néel Temperature was measured $T_N = 206~K$ [243]. In order to reduce numerical effort, we assumed FM order for both compounds. Figure 5.10 visualises schematically the structure assumed in our calculations.

We used 24^3 k-points in the BZ for the k-space integrations, all other settings were as in Section 5.1 introduced. We used the measured lattice constants. The lattice parameters were for UAsSe $a = 3.984$ Å and $c = 8.371$ Å, and for USb_2 we had $a = 4.270$ Å and $c = 8.748$ Å. The nearest neighbour distance was located for UAsSe about $d_{U-U} = 3.984$, and for USb_2 $d_{U-U} = 4.270$ in the U plane. The out-of-plane nearest neighbour distance was about for UAsSe $d_{U-U} = 4.777$, and for USb_2 $d_{U-U} = 4.891$. According Hills limit there is to be expected localised FM behaviour. Typically one finds for very large U-U
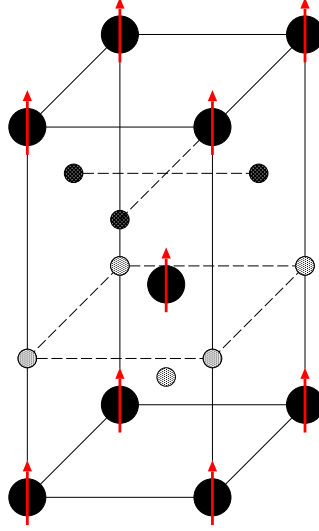
Figure 5.10: Structure of UAsSe and USb$_2$. Notation as following: ● - U atoms ○ - As, Sb atoms ◑ - Se, Sb atoms. The red bars indicate the spin quantisation axes, which are chosen for UAsSe to point along the [111] direction and for USb$_2$ to point along the [100] direction.

spacings AFM behaviour, which is indeed the case for USb$_2$.

Magnetic susceptibility measurements [244, 245], polarised neutron experiments [242], and photoemission experiments [246] favoured localised 5f states for UAsSe. However, the enhanced Sommerfield coefficient was reported to be between 27.4 and 40.6 mJ/(mol K^2) [247] as well as the experimental and calculated magneto-optical Kerr spectra [248, 249] suggested a more itinerant character of the 5f states, at least when the f electrons in the U-U planes are considered. Recently investigation by means of DFT calculations and ARPES underlined the fact of strong delocalisation in the U-U planes and strong localisation in perpendicular direction [250]. Treating the 5f states as partially localised and partially delocalised was successfully demonstrated in [251], supporting here the idea of having basal delocalisation and perpendicular localisation of the 5f states.

5.3.2   Results

Experimentally it was observed that for both compounds the Fermi surface is quasi two dimensional [252]. For USb$_2$ 4 two dimensional cylinders by means of de Haas - van Alphen measurements were observed [253, 254]. DFT calculations correctly reproduced this topology of the Fermi surface for USb$_2$ [255]. In order to justify the applicability of a FM configuration, we calculated the band structure and compared it with the calculated AFM band structure from literature. Figure 5.11 shows both band structures. The FM band structure was calculated without applied OPC, the AFM calculation is done fully relativistic without OPC and taken from [256]. By comparing both results we recognise differences at the M point, between the Γ and the X points, and between the

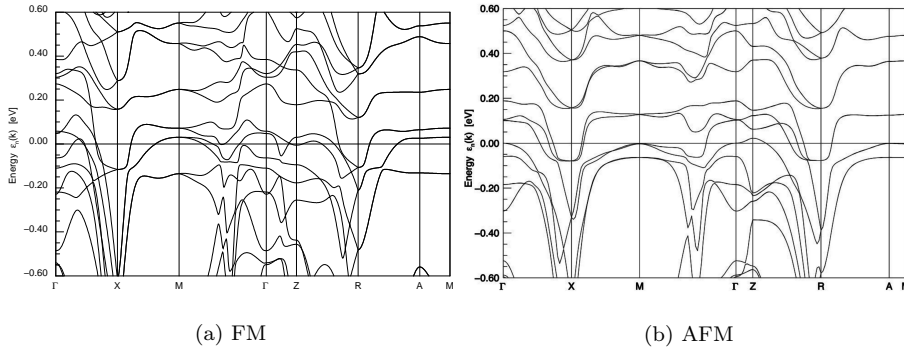(a) FM   (b) AFM

Figure 5.11: Calculated Band structure of USb$_2$. The FM calculation was done with
FPLO9, the AFM band structure was calculated with FPLO using LSDA,
and is taken from [256].

Γ and the M points. Apparently, the FM configuration produces more band
crossings than the AFM configuration leading to a slightly different Fermi sur-
face. However, the two dimensionality remains in both calculations. For both
compounds a FM set-up was chosen by reason of that the magnetic moment at
the uranium site is not strongly dependent on the magnetic order as seen in the
previous sections.

In Table 5.11 we list the calculated magnetic moments of UAsSe and USb$_2$.
The spin quantisation axis was defined for UAsSe along the [111] direction and
for USb$_2$ along [100] direction. The calculated DOS at ϵ_f is mainly driven by
the $5f$ states [257], indicating that here the $5f$ are then responsible for the
magnetism. Comparison with experimental and theoretical data from literature
reveals that the spin moment was in all calculations applying OPC overesti-
mated by a factor of $3.4 - 3.6$. Already, in a pure LSDA calculation the spin
moment was overestimated by a factor of 2.7. The measured orbital moment
was underestimated by a pure relativistic LSDA by 47%. All calculation using
OPC yielded slightly smaller orbital momenta than the measured. Apparently,
the orbital moment is calculated too small even when applying any OPC sug-
gesting that the f states have to be considered within a localised picture. We
found the wrong sign of μ_t for a pure LSDA calculation. Additionally, calcu-
lations performed with OPC showed that the total magnetic moment is almost
zero, caused by a large spin momentum and at the same time to small orbital
momenta.

For USb$_2$ only the ordered total magnetic moment is measured. As seen
for UAsSe, the calculated total moment is by far to small in comparison with
experiment. We reach same conclusions for the spin and orbital moment with
respect to OPC as previously for UAsSe.

When comparing the occupation numbers, we find for USb$_2$ for the $5f$ shell
2.85 (LSDA), 2.88 (OPB), 2.92 (OPxc), and 2.89 (OPx) and for the $6d$ shell 2.01,
1.99, 1.96, and 1.98 in the same notation. In that sense the $5f$ occupation is
larger that obtained for UM$_2$ compounds (Section 5.2). Even higher occupation
of the $5f$ states are found for UAsSe with: 2.91, 2.93, 2.99, and 2.95 and for the
$6d$ states: 1.74, 1.67, 1.63, and 1.66.

Table 5.11: Magnetic moments of UAsSe and USb$_2$. The magnetic moments were obtained using LSDA. Additional OPC was applied to the $5f$ states at the uranium site. The ASW calculation is taken from [249]. The FP-LMTO calculation is taken from [255] Experiments are taken from [242, 243, 258]. All moments are given in μ_B/(f.u.).

Cpd.	Method	μ_s	μ_l	μ_t
UAsSe	FPLO	1.79	−1.18	0.61
	FPLO + OPB	2.23	−2.23	−0.00
	FPLO + OPxc	2.40	−2.48	−0.16
	FPLO + OPx	2.28	−2.23	0.05
	ASW + SOC	1.86	−2.63	−0.77
	EXP (Neutrons)	*0.66*	*-2.08*	*-1.42*
	EXP (Magn.)	*–*	*–*	*-1.29*
USb$_2$	FPLO	1.35	−1.10	0.23
	FPLO + OPB	1.63	−1.89	−0.21
	FPLO + OPxc	1.89	−2.22	−0.33
	FPLO + OPx	1.69	−1.89	−0.20
	FPLMTO + SOC	2.05	−3.00	−0.95
	EXP (Neutrons)	*–*	*–*	*-1.88*

5.3.3 Summary

By electronic structure calculations, we have shown that for UAsSe and USb$_2$ OPC improve the description of the orbital momentum. However, it turns out, that the calculated spin moment is for UAsSe calculated too large by a factor of about $3 - 3.5$ in comparison with experiment. A possible way of avoiding this problem would be to fix the spin momentum by the measured ratio and do a fully relativistic calculation including OPC, as proposed in [218].

Band structure calculations reproduced the two dimensional character of the Fermi surface. We mark that at the high symmetry point M little changes of external variables (pressure, doping, magnetisation, ...) would produce a Lifshitz transition. Further calculations have to be done to clarify this situation, in order to find a singularity in a measurable and appropriate physical quantity, e.g. the thermopower [259].

6

Summary and Outlook

In this thesis magnetic properties from selected solids in the framework of DFT were discussed.

In Chapter 3 the applicability of the three Hund's rules on solids was discussed. In common approximations like LSDA and GGA, there are missing orbital dependent potentials, which however are necessary to describe appropriately OP in solids. By introducing a Stoner like expression for the OP, one gets rid of the underestimation of μ_l using conventional LSDA or GGA. The OP energies for $3d$, $4d$, $5d$, $4f$, and $5f$ shells, based on a previously proposed method, were presented. In order to account for relativistic effects we used either NR atomic orbitals or SR atomic orbitals to evaluate the OP energies.

In Chapter 4 we investigated magnetic moments and MCA of the transition metals Fe, Co, and Ni. A careful analysis of these magnetic properties using the OPC was done and the obtained results were compared with available data in literature. Orbital moments are better represented when applying OPC, but OPC often overestimates the measured MCA. In the Second part of Chapter four we analysed properties of thin FeCo films. Comparing ordered and disordered alloys it was demonstrated that these alloys have a large saturation magnetisation and at the same time have a large MCA. By applying the EBP, meaning that relaxed structures have been taken into account in the calculations, it was shown that smaller substrates, as currently used in experiments, will further increase the MCA. It was clearly demonstrated that the effect of ordering increases the MCA, as similar observed for FePt alloys.

In Chapter 5 a careful study of uranium compounds was done. We investigated the applicability of OPC on selected uranium compounds. The optimised lattice constant for UN showed no strong dependency on either of the OPC applied. By assuming different magnetic structures, the experimentally observed anti-ferromagnetic structure was reproduced only when OPC is applied. In all other cases, the wrong ground-state was observed. We estimated the MCA of these systems. It was found for US that the measured MCA was reproduced only by applying OPC. Furthermore, large MCA were also obtained for the other UX compounds and experimentally verification is desirable. In the second part of this chapter we investigated the class of UM_2 compounds. It was demonstrated that along the series different magnetic ground-states were observed. The question was answered whether possible magnetism is driven from the $3d$ states or the $5f$ states. The stability of FM was checked by applying the Stoner criterion on the NM states. It was shown that not all FM observed compounds ful-fill this criterion. The last part of this chapter presented the results of electronic struc-

ture calculations of ternary uranium dipnictides and dichalcogenides. It was shown that applied OPC improves the description of the orbital momenta. Further investigations of these quasi-two dimensional compounds about electronic topological transitions look promising.

A

Definitions

A.1 Spherical Harmonics

The complex spherical harmonics $\mathcal{Y}_L$ and the real spherical harmonics Y_L[1][2] are defined as,

$$\mathcal{Y}_L = (-1)^{\frac{m+|m|}{2}} P^l_{|m|}(\cos\theta) \sqrt{\frac{2l+1}{4\pi}} \sqrt{\frac{(l-|m|)!}{(l+|m|)!}} e^{im\phi} \tag{A.1}$$

$$Y_L = P^l_{|m|}(\cos\theta) \sqrt{\frac{2l+1}{2\pi(1+\delta_{m0})}} \sqrt{\frac{(l-|m|)!}{(l+|m|)!}} \begin{cases} \cos(|m|\phi) & m \leq 0 \\ \sin(|m|\phi) & m < 0 \end{cases} . \tag{A.2}$$

Conversion between $\mathcal{Y}_L$ and Y_L is to be done with,

$$\mathcal{Y}_L = a_m Y_{lm} + b_m Y_{l-m}, \tag{A.3}$$

in which

$$a_m = \begin{cases} -\frac{i}{\sqrt{2}} & m < 0 \\ 1 & m = 0 \\ -\frac{1}{\sqrt{2}}(-1)^m & m > 0 \end{cases} \qquad b_m = \begin{cases} \frac{1}{\sqrt{2}} & m < 0 \\ 0 & m = 0 \\ -\frac{i}{\sqrt{2}}(-1)^m & m > 0 \end{cases} . \tag{A.4}$$

The spherical spinors [54] as eigenvectors of the operators J^2, J_z, and L^2 with corresponding eigenvalues j, μ, and l are,

$$\chi_{\kappa\mu} = \Omega_{jl\mu} = \begin{pmatrix} c_{\kappa\mu\uparrow} \mathcal{Y}_{l_\kappa\mu-\frac{1}{2}} \\ c_{\kappa\mu\downarrow} \mathcal{Y}_{l_\kappa\mu+\frac{1}{2}} . \end{pmatrix} \tag{A.5}$$

Here the Clebsch-Gordon coefficients are,

---

[1]For further reading, we suggest [260].
[2]The subscript L refers here to lm.

$$
\begin{aligned}
c_{\kappa\mu\uparrow} &= & \sqrt{\frac{j+\mu}{2j}} & \\
c_{\kappa\mu\downarrow} &= & \sqrt{\frac{j-\mu}{2j}} & \left.\right\} \quad j = l_\kappa + \tfrac{1}{2} \\
c_{\kappa\mu\uparrow} &= & -\sqrt{\frac{j-\mu+1}{2j+2}} & \\
c_{\kappa\mu\downarrow} &= & \sqrt{\frac{j+\mu+1}{2j+2}} & \left.\right\} \quad j = l_\kappa - \tfrac{1}{2},
\end{aligned}
\tag{A.6}
$$

and

$$
l_\kappa = \begin{cases} \kappa & \kappa > 0 \\ -\kappa - 1 & \kappa < 0 \end{cases}
\tag{A.7}
$$

A.2 Other Definitions Used in Text

- Pauli matrices:

$$
\sigma_1 = \begin{pmatrix} 0 & 1 \\ 1 & 0 \end{pmatrix} \qquad \sigma_2 = \begin{pmatrix} 0 & -i \\ i & 0 \end{pmatrix} \qquad \sigma_3 = \begin{pmatrix} 1 & 0 \\ 0 & -1 \end{pmatrix}
\tag{A.8}
$$

- β matrix:

$$
\beta = \begin{pmatrix} \mathbb{1}_2 & 0 \\ 0 & -\mathbb{1}_2 \end{pmatrix}
\tag{A.9}
$$

- α matrices:

$$
\alpha_k = \begin{pmatrix} 0 & \sigma_k \\ \sigma_k & 0 \end{pmatrix}
\tag{A.10}
$$

- γ matrices:

$$
\gamma_k = \begin{pmatrix} 0 & -i\sigma_k \\ i\sigma_k & 0 \end{pmatrix}
\tag{A.11}
$$

- $\mathbf{\Sigma}$ matrix:

$$
\mathbf{\Sigma} = \begin{pmatrix} \boldsymbol{\sigma} & 0 \\ 0 & \boldsymbol{\sigma} \end{pmatrix}
\tag{A.12}
$$

- $\bar{a}_k^l$:

$$
\bar{a}_{k=1}^{l=2} = \frac{1}{14}, \qquad \bar{a}_{k=2}^{l=2} = \frac{1}{14}
\tag{A.13}
$$

$$
\bar{a}_{k=1}^{l=3} = \frac{2}{45}, \qquad \bar{a}_{k=2}^{l=3} = \frac{1}{33}, \qquad \bar{a}_{k=3}^{l=3} = \frac{50}{1287}
\tag{A.14}
$$

B

Input Parameters for Bulk DFT Calculations to Evaluate the Racah Parameter

B.1 d-Shells

Table B.1: Input settings for the bulk DFT calculations for the $3d$ elements.

$3d$	Spacegroup	a $[\text{Å}]$	b $[\text{Å}]$	c $[\text{Å}]$	Wyckoff
Ca	225	5.5884	5.5884	5.5884	(0, 0, 0)
Sc	194	3.3090	3.3090	5.2733	(1/3, 2/3, 1/4)
Ti	194	2.9508	2.9508	4.6855	(1/3, 2/3, 1/4)
V	229	3.0300	3.0300	3.0300	(0, 0, 0)
Cr	229	2.9100	2.9100	2.9100	(0, 0, 0)
Mn	217	8.9125	8.9125	8.9125	(0, 0, 0)
					(0.316, 0.316, 0.316)
					(0.356, 0.356, 0.034)
					(0.089, 0.089, 0.282)
Fe	229	2.8665	2.8665	2.8665	(0, 0, 0)
Co	194	2.5071	2.5701	4.0695	(1/3, 2/3, 1/4)
Ni	225	3.5240	3.5240	3.5240	(0, 0, 0)
Cu	225	3.6149	3.6149	3.6149	(0, 0, 0)
Zn	194	2.6649	2.6649	4.9468	(1/3, 2/3, 1/4)

Table B.2: Input settings for the bulk DFT calculations for the 4*d* elements.

4*d*	Spacegroup	a [Å]	b [Å]	c [Å]	Wyckoff
Sr	225	6.0849	6.0849	6.0849	(0, 0, 0)
Y	194	3.6474	3.6474	5.7306	(1/3, 2/3, 1/4)
Zr	194	3.2320	3.2508	5.1470	(1/3, 2/3, 1/4)
Nb	229	3.0004	3.0004	3.0004	(0, 0, 0)
Mo	229	3.1470	3.1470	3.1470	(0, 0, 0)
Tc	194	2.7350	2.7350	4.3880	(1/3, 2/3, 1/4)
Ru	194	2.7059	2.7059	4.2815	(1/3, 2/3, 1/4)
Rh	225	3.8034	3.8034	3.8034	(0, 0, 0)
Pd	225	3.8907	3.8907	3.8907	(0, 0, 0)
Ag	225	4.0853	4.0853	4.0853	(0, 0, 0)
Cd	194	2.9794	2.9794	5.6186	(1/3, 2/3, 1/4)

Table B.3: Input settings for the bulk DFT calculations for the 5*d* elements.

5*d*	Spacegroup	a [Å]	b [Å]	c [Å]	Wyckoff
Ba	229	5.0280	5.0280	5.0280	(0, 0, 0)
La	194	3.7720	3.7720	12.144	(0, 0, 0)
					(1/3, 2/3, 1/4)
Hf	194	3.1964	3.1964	5.0511	(1/3, 2/3, 1/4)
Ta	229	3.3013	3.3013	3.3013	(0, 0, 0)
W	229	3.1652	3.1652	3.1652	(0, 0, 0)
Re	194	2.7610	2.7610	4.4560	(1/3, 2/3, 1/4)
Os	194	2.7344	2.7344	4.4317	(1/3, 2/3, 1/4)
Ir	225	3.8390	3.8390	3.8390	(0, 0, 0)
Pt	225	3.9242	3.9242	3.9242	(0, 0, 0)
Au	225	4.0782	4.0782	4.0782	(0, 0, 0)
Hg	166	3.4600	3.4600	6.7020	(0, 0, 0)

B.2 f-Shells

Table B.4: Input settings for the bulk DFT calculations for the $4f$ elements.

$4f$	Spacegroup	$a\,[\text{Å}]$	$b\,[\text{Å}]$	$c\,[\text{Å}]$	Wyckoff
La	194	3.7720	3.7720	12.144	(0, 0, 0)
					(1/3, 2/3, 1/4)
Ce	194	3.6200	3.6200	5.9900	(1/3, 2/3, 1/4)
Pr	194	3.6725	3.6725	11.8354	(0, 0, 0)
					(1/3, 2/3, 1/4)
Nd	194	3.6580	3.6580	11.7990	(0, 0, 0)
					(1/3, 2/3, 1/4)
Pm	194	3.6435	3.6435	11.7626	(0, 0, 0)
					(1/3, 2/3, 1/4)
Sm	166	3.6199	3.6199	11.6800	(0, 0, 0)
					(1/3, 2/3, 1/4)
Eu	229	4.5810	4.5810	4.5810	(0, 0, 0)
Gd	194	3.6360	3.6360	5.7825	(1/3, 2/3, 1/4)
Tb	194	3.6010	3.6010	5.6936	(1/3, 2/3, 1/4)
Dy	194	3.5930	3.5930	5.6537	(1/3, 2/3, 1/4)
Ho	194	3.5773	3.5773	5.6158	(1/3, 2/3, 1/4)
Er	194	3.5588	3.5588	5.5874	(1/3, 2/3, 1/4)
Tm	194	3.5375	3.5375	5.5546	(1/3, 2/3, 1/4)
Yb	225	5.4847	5.4847	5.4847	(0, 0, 0)
Lu	194	3.5031	3.5031	5.5509	(1/3, 2/3, 1/4)

Table B.5: Input settings for the bulk DFT calculations for the $5f$ elements.

$5f$	Spacegroup	$a\,[\text{Å}]$	$b\,[\text{Å}]$	$c\,[\text{Å}]$	Wyckoff
Ac	225	5.6700	5.6700	5.6700	(0, 0, 0)
Th	225	5.0847	5.0847	5.0847	(0, 0, 0)
Pr	139	3.9250	3.9250	3.2380	(0, 0, 0)
U	63	2.8537	5.8695	4.9548	(0, 0.10199, 1/4)

Bibliography

[1] M. Born and R. Oppenheimer. Zur Quantentheorie der Molekeln. *Ann. Phys.*, 389:457 – 484, 1927.

[2] V. Fock. Näherungsmethode zur Lösung des quantenmechanischen Mehrkörperproblems. *Z. Phys. A: Hadrons Nucl.*, 61:126 – 148, 1930.

[3] D. R. Hartree. The wave mechanics of an atom with a non-coulomb central field. I. Theory and methods. *Proc. Cambridge Philos. Soc.*, 24:89 – 110, 1928.

[4] J.C. Slater. Note on Hartree's Method. *Phys. Rev.*, 35:210 – 211, 1930.

[5] L.H. Thomas. The calculation of atomic fields. *Proc. Cambridge Philos. Soc*, 23:542 – 548, 1927.

[6] E. Fermi. Un metodo statistico per la determinazione di alcune priorieta dell'atome. *Rend. Accad. Naz. Lincei*, 6:602 – 607, 1927.

[7] P. Hohenberg and W. Kohn. Inhomogeneous Electron Gas. *Phys. Rev.*, 136:B864 – B871, 1964.

[8] W. Kohn and L. J. Sham. Self-Consistent Equations Including Exchange and Correlation Effects. *Phys. Rev.*, 140:A1133 – A1138, 1965.

[9] U. von Barth and L. Hedin. A local exchange-correlation potential for the spin polarized case:I. *J. Phys. C*, 5:1629 – 1642, 1972.

[10] E.C. Stoner. Collective Electron Specific Heat and Spin Paramagnetism in Metals. *Proc. R. Soc. London A*, 154:656 – 678, 1936.

[11] E.C. Stoner. Collective Electron Ferromagnetism. II. Energy and Specific Heat. *Proc. R. Soc. London A*, 169:339 – 371, 1939.

[12] O. Gunnarsson. The Stoner Model in the Spin-Density-Functional Formalism. *Physica B+C*, 91B:329 – 336, 1977.

[13] R. M. Dreizler and E. K. U. Gross. *Density Functional Theory*. Springer Verlag, 1999.

[14] V.I. Anisimov, J. Zaanen, and O.K. Andersen. Band theory and Mott insulators: Hubbard U instead of Stoner I. *Phys. Rev. B*, 44:943 – 954, 1991.

[15] V.I. Anisimov, F. Aryasetiawan, and A.I. Liechtenstein. First-principles calculations of the electronic structure and spectra of strongly correlated systems: the LDA + U method. *J. Phys.: Condens. Matter*, 9:767 – 808, 1997.

[16] M. Richter. *Density Functional Theory applied to 4f and 5f Elements and Metallic Compounds*, volume 13, pages 87 – 229. Elsevier, 2001.

[17] A. K. Rajagopal and J. Callaway. Inhomogeneous Electron Gas. *Phys. Rev. B*, 7:1912 – 1919, 1973.

[18] H. Eschrig, G. Seifert, and P. Ziesche. Current Density Functional Theory of Quantum Electrodynamics. *Sol. St. Commun.*, 56:777 – 780, 1985.

[19] A. K. Rajagopal. Inhomogeneous relativistic electron gas. *Journal of Physics C: Solid State Physics*, 11:L943 – L948, 1978.

[20] A.H. MacDonald and S. H. Vosko. A relativistic density functional formalism. *Journal of Physics C: Solid State Physics*, 12:2977 – 2990, 1979.

[21] G. Vignale and M. Rasolt. Density-functional theory in strong magnetic fields. *Phys. Rev. Lett.*, 59:2360 – 2363, 1987.

[22] G. Vignale and Mark Rasolt. Current- and spin-density-functional theory for inhomogeneous electronic systems in strong magnetic fields. *Phys. Rev. B*, 37:10685 – 10696, 1988.

[23] P. Skudlarski and G. Vignale. Exchange-correlation energy of a three-dimensional electron gas in a magnetic field. *Phys. Rev. B*, 48:8547 – 8559, 1993.

[24] H. Ebert, M. Battocletti, and E.K.U. Gross. Current density functional theory of spontaneously magnetised solids. *Europhys. Lett.*, 40:545 – 550, 1997.

[25] O. Eriksson, M.S.S. Brooks, and B. Johansson. Orbital polarization in narrow-band systems: Application to volume collapses in light lanthanides. *Phys. Rev. B*, 41:7311 – 7314, 1990.

[26] I.V. Solovyev, A.I. Liechtenstein, and K. Terakura. Is Hund's Second Rule Responsible for the Orbital Magnetism in Solids? *Phys. Rev. Lett.*, 80:5758 – 5761, 1998.

[27] O. K. Andersen. Linear methods in band theory. *Phys. Rev. B*, 12:3060 – 3083, 1975.

[28] J. Korringa. On the calculation of the energy of a Bloch wave in a metal. *Physica*, 13:392 – 400, 1947.

[29] N. Kohn, W. und Rostoker. Solution of the Schrödinger Equation in Periodic Lattices with an Application to Metallic Lithium. *Phys. Rev.*, 94:1111 – 1120, 1954.

[30] A. R. Williams, J. Kübler, and C. D. Gelatt. Cohesive properties of metallic compounds: Augmented-spherical-wave calculations. *Phys. Rev. B*, 19:6094 – 6118, 1979.

[31] J. C. Slater. Wave Functions in a Periodic Potential. *Phys. Rev.*, 51:846 – 851, 1937.

[32] O. K. Andersen. Simple approach to the band-structure problem. *Solid State Communications*, 13:133 – 136, 1973.

[33] H. Ebert. Fully Relativistic Bandstructure Calculations for Magnetic Solids - Formalism and Application. In H. Dreysse, editor, *Electronic Structure and Physical Properties of Solids*, volume 535 of *Lecture Notes in Physics*, page 191. Springer, Berlin, 2000.

[34] H. Eschrig. *Optimized LCAO method and the electronic structure of extended systems.* Springer Verlag, Berlin, 1989.

[35] K. Koepernik and H. Eschrig. Full-potential nonorthogonal local-orbital minimum-basis band-structure scheme. *Phys. Rev. B*, 59:1743 – 1757, 1999.

[36] M. Levy. Electron densities in search of Hamiltonians. *Phys. Rev. A.*, 26:1200 – 1208, 1982.

[37] E.H. Lieb. Density Functionals for Coulomb-Systems. *Int. J. Quan. Chem.*, 24:243 – 277, 1983.

[38] R. G. Parr and W. Yang. *Density-Functional Theory of Atoms and Molecules.* Oxford University Press, 1989.

[39] P. Fulde. *Electron Correlations in Molecules and Solids.* Springer Verlag, 1995.

[40] H. Eschrig. *The Fundamentals of Density Functional Theory.* B.G. Teubner Verlagsgesellschaft, 1996.

[41] J. F. Janak. Proof that $\frac{\partial E}{\partial n_i} = \epsilon$ in density-functional theory. *Phys. Rev. B*, 18:7165 – 7168, 1978.

[42] D. M. Ceperley and B. J. Alder. Ground state of the electron gas by a stochastic method. *Phys. Rev. Lett.*, 45:566 – 569, 1980.

[43] S. H. S. H. Vosko, L. Wilk, and M. Nusair. Accurate spin-dependent electron liquid correlation energies for local spin density calculations: a critical analysis. *Can. J. Phys.*, 58:1200 – 1211.

[44] J. P. Perdew and A. Zunger. Self-interaction correction to density-functional approximations for many-electron systems. *Phys. Rev. B*, 23:5048 – 5079, 1981.

[45] John P. Perdew and Yue Wang. Accurate and simple analytic representation of the electron-gas correlation energy. *Phys. Rev. B*, 45:13244 – 13249, 1992.

[46] O. Opahle. PhD thesis, 2001.

[47] J.P. Perdew, K. Burke, and Y. Wang. Generalized gradient approximation for the exchange-correlation hole of a many-electron system. *Phys. Rev. B*, 54:16533 – 16539, 1996.

[48] A. Svane. Electronic structure of cerium in the self-interaction-corrected local-spin-density approximation. *Phys. Rev. B*, 53:4275 – 4286, 1996.

[49] H. Eschrig, K. Koepernik, and I. Chaplygin. Density functional application to strongly correlated electron systems. *J. Sol. St. Chem.*, 176:482 – 495, 2003.

[50] H. Eschrig, M. Richter, and I. Opahle. Relativitic Solid State Calculations. In *Relativistic Electronic Structure Theory, Part 2: Applications*, volume 14. Elsevier B.V., 2004.

[51] C. Itzykson and J. B. Zuber. *Quantum Field Theory*. McGraw-Hill Book Company, New York, 1980.

[52] W. Gordon. Der Strom der Diracschen Elektronentheorie. *Z. Phys. A*, 50:630 – 632, 1928.

[53] M. S. S. Brooks and P. J. Kelly. Large Orbital-Moment Contribution to $5f$ Band Magnetism. *Phys. Rev. Lett.*, 51:1708 – 1711, 1983.

[54] J. J. Sakurai. *Advanced Quantum Mechanics*. Addison-Wesley Publishing Company, Inc., 1967.

[55] K. Koepernik, B. Velický, R. Hayn, and H. Eschrig. Self-consistent LCAO-CPA method for disordered alloys . *Phys. Rev. B*, 55:5717 – 5729, 1997.

[56] P. Ewald. Die Berechnung optischer und elektrostatischer Gitterpotentiale. *Ann. Phys.*, 369:253 – 287, 1921.

[57] G. Lehmann and M. Taut. On the Numerical Calculation of the Density of States and Related Properties. *Phys. Status Solidi (b)*, 54:469 – 477, 1972.

[58] Peter E. Blöchl, O. Jepsen, and O. K. Andersen. Improved tetrahedron method for Brillouin-zone integrations. *Phys. Rev. B*, 49:16223 – 16233, 1994.

[59] G.H.O. Daalderop, P.J. Kelly, and M.F.H. Schuurmans. Magnetocrystalline anisotropy and orbital moments in transition-metal compounds. *Phys. Rev. B*, 44:12054 – 12057, 1991.

[60] L. Nordström, M.S.S. Brooks, and B. Johansson. Orbital magnetization and anisotropy energy in YCo_5. *J. Phys.: Condens. Matter*, 4:3261 – 3272, 1992.

[61] J. Trygg. PhD thesis, 1995.

[62] S. Chikazumi. *Physics of Ferromagnetism*. Oxford, Clarendon Press, 1997.

[63] J.H. van Vleck. On the Anisotropy of Cubic Ferromagnetic Crystals. *Phys. Rev.*, 52:1178 – 1198, 1937.

[64] N.S. Akulov. Über das magnetische Quadrupolmoment des Eisenatoms. *Z. Physik*, 57:249 – 256, 1929.

[65] N.S. Akulov. Zur Theorie der Feinstruktur der Magnetisierungskurven der Einkristalle. *Z. Physik*, 69:78 – 99, 1931.

[66] M. Kuz'min and R. Richter. Magnetic Anisotropy Calculations: Materials of Technological Interest. In K.H.J. Buschow, R.W.C. Merton, C. Flemings, E.J. Ilschner, B. Kramer, S. Mahajan, and Veyssiere P., editors, *Encyclopedia of Materials: Science and Technology*, pages 1 – 7. Elsevier, Oxford, 2001.

[67] H.J.F. Jansen. Magnetic anisotropy in density-functional theory. *Phys. Rev. B*, 59:4699 – 4707, 1999.

[68] I. Turek, V. Drchal, J. Kudrnovský, M. Šŏb, and P. Weinberger. *Electronic Structure of Disordered Alloys, Surfaces and Interfaces.*

[69] L. Nørdheim. Elektronentheorie der Metalle I. *Ann. Phys.*, 401:607 – 640, 1931.

[70] T. Muto. On the Electronic Structure of Alloys. *Sci. Pap. Inst. Phys. Chem. Res.*, 34:377, 1938.

[71] K. Yosida. *Theory of Magnetism.* Springer Verlag Berlin, 1996.

[72] M.S.S. Brooks. Calculated ground state properties of light actinide metals and their compounds. *Physica B+C*, 130B:6 – 12, 1985.

[73] B.R. Judd. *Operator Techniques in Atomic Spectroscopy.* McGraw-Hill, New York, 1969.

[74] H. Eschrig, M. Sargolzaei, K. Koepernik, and M. Richter. Orbital polarization in the Kohn-Sham-Dirac theory. *Euro. Phys. Lett.*, 72:611 – 617, 2005.

[75] M. Sargolzaei. *Orbital Polarization in Relativistic Density Functional Theory.* PhD thesis, 2006.

[76] J.C. Slater. Average Energy of States of Given Multiplicites in Atoms. *Phys. Rev.*, 165:655 – 658, 1968.

[77] R.D. Cowan. *The Theory of Atomic Structure and Spectra*, volume 1.

[78] J.A. Gaunt. On the triplets of helium. *Philos. Trans. Roy. Soc. London, Ser. A*, 228:151 – 196, 1929.

[79] O. Eriksson, B. Johansson, R.C. Albers, A.M. Boring, and M.S.S. Brooks. Orbital magnetism in Fe, Co, and Ni. *Phys. Rev. B*, 42:2707 – 2710, 1990.

[80] J.M. Wills, O. Eriksson, M. Alouani, and D.L. Price. *Electronic Structure and Physical Properties of Solids: The Uses of the LMTO Method.*

[81] T. Burkert, O. Eriksson, P. James, S.I. Simak, B. Johansson, and L. Nordström. Calculation of uniaxial magnetic anisotropy energy of tetragonal and trigonal Fe, Co, and Ni. *Phys. Rev. B*, 70:139901, 2004.

[82] T. Burkert, L. Nordström, O. Eriksson, and O. Heinonen. Giant Magnetic Anisotropy in Tetragonal FeCo Alloys. *Phys. Rev. Lett.*, 93:027203 – 027206, 2004.

[83] G. Andersson, T. Burkert, P. Warnicke, M. Björck, B Sanyal, C. Chacon, C. Zlotea, L. Nordström, P. Nordblad, and O. Eriksson. Perpendicular Magnetocrystalline Anisotropy in Tetragonally Distorted Fe-Co Alloys. *Phys. Rev. Lett.*, 96:037205 – 037208, 2006.

[84] E.C. Bain. The nature of martensite. *Trans. AIME*, 70:25, 1924.

[85] M.B. Stearns. *Magnetic Properties of 3d, 4d, and 5d Elements, Alloys and Compounds*, volume III/19a of *Landolt-Börnstein.* Springer-Verlag, 1986.

[86] A.R. Mackintosh and O.K. Andersen. *Electrons at the Fermi Surface*, volume 1. Cambridge University Press, New York, 1980.

[87] P. Bruno. Tight-binding approach to the orbital magnetic moment and magnetocrystalline anisotropy of transition-metal monolayers. *Phys. Rev. B*, 39:865 − 868, 1989.

[88] L. Steinbeck, M. Richter, and H. Eschrig. Itinerant-electron magnetocrystalline anisotropy energy of YCo_5 and related compounds. *Phys. Rev. B*, 63:184431, 2001.

[89] S. Chadov, J. Minár, M.I. Katsnelson, H. Ebert, D. Ködderitzsch, and A.I. Lichtenstein. Orbital magnetism in transition metal systems: The role of local correlation effects. *Europhys. Lett.*, 82:37001, 2008.

[90] M.T. Czyżyk and G.A. Sawatzky. Local-density functional and on-site correlations: The electronic structure of La_2CuO_4 and $LaCuO_3$. *Phys. Rev. B*, 49:14211 − 14228, 1994.

[91] A. Grechnev, I. Di Marco, M.I. Katsnelson, A.I. Lichtenstein, J. Wills, and O. Eriksson. Theory of bulk and surface quasiparticle spectra for Fe, Co, and Ni. *Phys. Rev. B*, 76:035107, 2007.

[92] D. Chandesris, J. Lecante, and Y. Petroff. Two-electron resonances in transition metals. *Phys. Rev. B*, 27:2630 − 2635, 1983.

[93] A. Gutiérrez and M.F. López. Angle-resolved resonant photoemission at the $MIII$ absorption threshold of Co and Fe metal. *Phys. Rev. B*, 56:1111 − 1113, 1997.

[94] C. Guillot, Y. Ballu, J. Paigné, J. Lecante, K.P. Jain, P. Thiry, R. Pinchaux, Y. Pétroff, and L.M. Falicov. Resonant Photoemission in Nickel Metal. *Phys. Rev. Lett.*, 39:1632 − 1635, 1977.

[95] J. Sánchez-Barriga, J. Fink, V. Boni, I. Di Marco, J. Braun, J. Minár, A. Varykhalov, O. Rader, V. Bellini, F. Manghi, H. Ebert, M. I. Katsnelson, A.I. Lichtenstein, O. Eriksson, W. Eberhardt, and H.A. Dürr. Strength of Correlation Effects in the Electronic Structure of Iron. *Phys. Rev. Lett.*, 103:267203, 2009.

[96] A.I. Lichtenstein, M.I. Katsnelson, and G. Kotliar. Finite-temperature magnetism of transition metals: an LDA+DMFT approach. *ArXiv Condensed Matter e-prints*, 2001.

[97] J. Schäfer, M. Hoinkis, E. Rotenberg, P Blaha, and R. Claessen. Fermi surface and electron correlation effects of ferromagnetic iron. *Phys. Rev. B*, 72:155115, 2005.

[98] C.G. Shull and Y. Yamada. . *J. Phys. Soc. Japan*, 17:Suppl. B−III p. 1, 1961.

[99] R.M. Moon. Distribution of Magnetic Moment in Hexagonal Cobalt. *Phys. Rev.*, 136:A195 − A202, 1964.

[100] H.A. Mook. Magnetic Moment Distribution of Nickel Metal. *Phys. Rev.*, 148:495 – 501, 1966.

[101] A. J. P. Meyer and G. Asch. Experimental g' and g Values of Fe, Co, Ni, and Their Alloys. *Journal of Applied Physics*, 32:S330 – S333, 1961.

[102] R.A. Reck and D.L. Fry. Orbital and Spin Magnetization in Fe-Co, Fe-Ni, and Ni-Co. *Phys. Rev.*, 184:492 – 495, 1969.

[103] C.T. Chen, Y.U. Idzerda, H.J. Lin, N.V. Smith, G. Meigs, E. Chaban, G.H. Ho, E. Pellegrin, and F. Sette. Experimental Confirmation of the X-Ray Magnetic Circular Dichroism Sum Rules for Iron and Cobalt. *Phys. Rev. Lett.*, 75:152 – 155, 1995.

[104] P. Söderlind, O. Eriksson, B. Johansson, R.C. Albers, and A.M. Boring. Spin and orbital magnetism in Fe-Co and Co-Ni alloys. *Phys. Rev. B*, 45:12911 – 12916, 1992.

[105] G. Kotliar, S.Y. Savrasov, K. Haule, V.S. Oudovenko, O. Parcollet, and C.A. Marianetti. Electronic structure calculations with dynamical mean-field theory. *Rev. Mod. Phys.*, 78:865 – 951, 2006.

[106] M. Okutani and T. Jo. Orbital Magnetic Moment in Superlattices of Transition Metals. *J. Phys. Soc. Jpn.*, 69:598 – 606, 2000.

[107] G.H.O. Daalderop, P.J. Kelly, and M.F.H. Schuurmans. First-principles calculation of the magnetocrystalline anisotropy energy of iron, cobalt, and nickel. *Phys. Rev. B*, 41:11919 – 11937, 1990.

[108] H.J.F. Jansen. Origin of orbital momentum and magnetic anisotropy in transition metals. *J. Appl. Phys.*, 67:4555 – 4557, 1990.

[109] S. Sharma, S. Pittalis, S. Kurth, S. Shallcross, J.K. Dewhurst, and E.K.U. Gross. Comparison of exact-exchange calculations for solids in current-spin-density- and spin-density-functional theory. *Phys. Rev. B*, 76:100401 – 100404, 2007.

[110] S. Sharma, J. K. Dewhurst, C. Ambrosch-Draxl, S. Kurth, N. Helbig, S. Pittalis, S. Shallcross, L. Nordström, and E. K. U. Gross. First-Principles Approach to Noncollinear Magnetism: Towards Spin Dynamics. *Phys. Rev. Lett.*, 98:196405, 2007.

[111] I.V. Solovyev. Orbital Polarization in Itinerant Magnets. *Phys. Rev. Lett.*, 95:267205 – 267208, 2005.

[112] J. Friedel. *Transition metals. Electronic structure of the d-band. Its role in the crystalline and magnetic structures.*

[113] K.Z. Gao, O. Heinonen, and Y. Chen. Read and write processes, and head technology for perpendicular recording. *J. Magn. Magn. Mater.*, 321:495 – 507, 2009.

[114] S.H. Charap, P.L. Lu, and Y.J. He. Thermal Stability of Recorded Information at High Densities. *IEEE Trans. Magn.*, 33:978 – 983, 1997.

[115] D. Weller and A. Moser. Thermal Effect Limits in Ultrahigh-Density Magnetic Recording. *IEEE Transactions on Magnetics*, 35:4423 – 4439, 1999.

[116] Y. Kubota, L. Folks, and E.E. Marinero. Intergrain magnetic coupling and microstructure in CoPtCr, CoPtCrTa, and CoPtCrB alloys. *J. Appl. Phys.*, 84:6202 – 6207, 1998.

[117] M.F. Toney, E.E. Marinero, M.F. Doerner, and P.M. Rice. High anisotropy CoPtCrB magnetic recording media. *J. Appl. Phys.*, 94:4018 – 4023, 2003.

[118] T. Shimatsu, H. Sato, K. Mitsuzuka, T. Oikawa, Y. Inaba, H. Aoi, H. Muraoka, Y. Nakamura, O. Kitakami, and S. Okamoto. K_{u2} magnetic anisotropy term of coptcr-sio$_2$ media for high density recording. *J. Appl. Phys.*, 97:10N111, 2005.

[119] J.R. Childress, J.L. Duvail, S. Jasmin, A. Barthémé, A. Fert, A. Schuhl, O Durand, and P. Galtier. Perpendicular magnetic anisotropy in Co_xPd_{1-x} alloy films grown by molecular beam epitaxy. *J. Appl. Phys.*, 75:6412 – 6414, 1994.

[120] T. Burkert, O. Eriksson, S.I. Simak, A.V. Ruban, B. Sanyal, L. Nordström, and J.M. Wills. Magnetic anisotropy of L1$_0$ FePt and Fe$_{1-x}$Mn$_x$Pt. *Phys. Rev. B*, 71:134411, 2005.

[121] D. Weller, A. Moser, L. Folks, M.E. Best, W. Lee, M.F. Toney, M. Schwickert, J.U. Thiele, and M.F. Doerner. High K_U Materials Approach to 100 Gbits/in^2. *IEEE Transactions on Magnetics*, 36:10 – 15, 2000.

[122] A. Sakuma. Electronic Structure and Magnetocrystalline Anisotropy Energy of MnAl. *J. Phys. Soc. Jpn.*, 63:1422 – 1428, 1994.

[123] I. Opahle, M. Richter, M.D. Kuz'min, U. Nitzsche, K. Koepernik, and L. Schramm. Calculated magnetocrystalline anisotropy of existing and hypothetical MCo$_5$ compounds. *Journal of Magnetism and Magnetic Materials*, 290-291:374 – 377, 2005.

[124] P. Larson, I.I. Mazin, and D.A. Papaconstantopoulos. Calculation of magnetic anisotropy energy in SmCo$_5$. *Phys. Rev. B*, 67:214405, 2003.

[125] P.H. Dederichs, S. Blügel, R. Zeller, and H. Akai. Ground States of Constrained Systems: Application to Cerium Impurities. *Phys. Rev. Lett.*, 53:2512 – 2515, 1984.

[126] K. Schwarz and P. Mohn. Itinerant metamagnetism in YCO$_2$. *Journal of Physics F: Metal Physics*, 14:L129, 1984.

[127] A.R. Williams, V.L. Moruzzi, J. Kübler, and K. Schwarz. *Bull. Am. Phys. Soc.*, 20:278, 1984.

[128] V.L. Moruzzi, P.M. Marcus, K. Schwarz, and P. Mohn. Ferromagnetic phases of bcc and fcc Fe, Co, and Ni. *Phys. Rev. B*, 34:1784 – 1791, 1986.

[129] L. Nordström, B. Johansson, O. Eriksson, and M.S.S. Brooks. Theoretical study of metamagnetism in ThCo$_5$. *Phys. Rev. B.*, 42:8367 – 8374, 1990.

[130] P. M. Marcus, F. Jona, and S. L. Qiu. Epitaxial Bain paths and metastable phases from first-principles total-energy calculations. *Phys. Rev. B*, 66:064111, 2002.

[131] M. Šob, L. G. Wang, and V. Vitek. Local stability of higher-energy phases in metallic materials and its relation to the structure of extended defects. *Comput. Mater. Sci.*, 8:100 – 106, 1997.

[132] F. Milstein, H.E. Fang, and J. Marschall. Mechanics and energetics of the Bain transformation. *Philos. Mag. A*, 70:621 – 629, 1994.

[133] P. Alippi, P.M. Marcus, and M. Scheffler. Strained Tetragonal States and Bain Paths in Metals. *Phys. Rev. Lett.*, 78:3892 – 3895, 1997.

[134] J. Buschbeck, I. Opahle, S. Fähler, L. Schultz, and M. Richter. Magnetic properties of Fe-Pd magnetic shape memory alloys: Density functional calculations and epitaxial films. *Phys. Rev. B*, 77:174421, 2008.

[135] J. Häglund. Fixed-spin-moment calculations on bcc and fcc iron using the generalized gradient approximation. *Phys. Rev. B*, 47:566 – 569, 1993.

[136] A. Winkelmann, M. Przybylski, F. Luo, Y. Shi, and J. Barthel. Perpendicular Magnetic Anisotropy Induced by Tetragonal Distortion of FeCo Alloy Films Grown on Pd(001). *Phys. Rev. Lett.*, 96:257205, 2006.

[137] F. Luo, X.L. Fu, A. Winkelmann, and M. Przybylski. Tuning the perpendicular magnetic anisotropy in tetragonally distorted Fe$_x$Co$_{1-x}$ alloy films on Rh(001) by varying the alloy composition. *Appl. Phys. Lett.*, 91:262512, 2007.

[138] F. Yildiz, F. Luo, C. Tieg, R.M. Abrudan, X.L. Fu, A. Winkelmann, M. Przybylski, and J. Kirschner. Strongly Enhanced Orbital Moment by Reduced Lattice Symmetry and Varying Composition of Fe$_{1-x}$Co$_x$ Alloy Films. *Phys. Rev. Lett.*, 100:037205, 2008.

[139] F. Yildiz, M. Przybylski, X.D. Ma, and J. Kirschner. Strong perpendicular anisotropy in Fe$_{1-x}$Co$_x$ alloy films epitaxially grown on mismatching Pd(001), Ir(001), and Rh(001) substrates. *Phys. Rev. B*, 80:064415, 2009.

[140] F. Yildiz, M. Przybylski, and J. Kirschner. Volume contribution to perpendicular anisotropy in Fe$_{0.5}$Co$_{0.5}$ alloy films on Pd(001), Ir(001), and Rh(001). *J. Appl. Phys.*, 105:07E129, 2009.

[141] W.B. Pearson. *A Handbook of Lattice Spacings and Structures of Metals and Alloys*, volume 1. Pergamon Press, 1958.

[142] Y. Tsunoda. Spin-density wave in cubic γ-Fe and γ-Fe$_{100-x}$Co$_x$ precipitates in Cu. *J. Phys.: Condens. Matter*, 1:10427 – 10438, 1989.

[143] L. Petit, A. Svane, Z. Szotek, W.M. Temmermann, and G.M. Stocks. Self-interaction corrected local spin density calculations of actinides. In *Materials Science and Engineering*, volume 9.

[144] J. van Ek, P.A. Sterne, and A. Gonis. Phase stability of plutonium. *Phys. Rev. B*, 48:16280 – 16289, 1993.

[145] J. Kollár, L. Vitos, and H.L Skriver. Anomalous atomic volume of α-Pu. *Phys. Rev. B*, 55:15353 – 15355, 1997.

[146] A.L. Kutepov and S.G. Kutepova. The ab initio ground state properties and magnetic structure of plutonium. *Journal of Physics: Condensed Matter*, 15:2607 – 2624, 2003.

[147] P. Söderlind, J.M. Wills, B. Johansson, and O. Eriksson. Structural properties of plutonium from first-principles theory. *Phys. Rev. B*, 55:1997 – 2004, 1997.

[148] L.V. Pourovskii, M.I. Katsnelson, A.I. Lichtenstein, L. Havela, T. Gouder, F. Wastin, A.B. A. B. Shick, Drchal. V., and G.H. G. H. Lander. Nature of non-magnetic strongly-correlated state in δ-plutonium. *Euro. Phys. Lett.*, 74:479, 2006.

[149] J.H. Shim, K. Haule, and G. Kotliar. Fluctuating valence in a correlated solid and the anomalous properties of *delta*-plutonium. *Nature*, 446:513 – 516, 2007.

[150] A.B. Shick, J. Kolorenč, L. Havela, V. Drchal, and T. T. Gouder. Multiplet effects in the electronic structure of δ-Pu, Am and their compounds. *Euro. Phys. Lett.*, 77:17003, 2007.

[151] S. Heathman, R.G. Haire, T. Le Bihan, A. Lindbaum, M. Idiri, P. Normile, S. Li, R. Ahuja, B. Johansson, and G.H. Lander. A High-Pressure Structure in Curium Linked to Magnetism. *Science*, 309:110 – 113, 2005.

[152] K.T. Moore, G. van der Laan, R.G. Haire, M.A. Wall, A.J. Schwartz, , and P. Söderlind. Emergence of Strong Exchange Interaction in the Actinide Series: The Driving Force for Magnetic Stabilization of Curium. *Phys. Rev. Lett.*, 98:236402, 2007.

[153] K.T. Moore and G. van der Laan. Nature of the 5f states in actinide metals. *Rev. Mod. Phys.*, 81:235 – 298, 2009.

[154] A.J. Freeman and D.D. Koelling. In A.J. Freeman and J.E. Darby, editors, *The Actinides: Electronic Structure and Related Properties*, volume 1. 1974.

[155] W.E. Pickett, A.J. Freeman, and D.D. Koelling. Self-consistent linearized augmented-plane-wave study of the electronic structure and superconductivity of fcc lanthanum under pressure. *Phys. Rev. B*, 22:2695 – 2715, 1980.

[156] W.E. Pickett, A.J. Freeman, and D.D. Koelling. Erratum: Self-consistent linearized augmented-plane-wave study of the electronic structure and superconductivity of fcc lanthanum under pressure. *Phys. Rev. B*, 23:5651, 1981.

[157] T. Gasche, M.S.S. Brooks, and B. Johansson. Calculated optical properties of thorium, protactinium, and uranium metals. *Phys. Rev. B*, 54:2446 – 2452, 1996.

[158] V.N. Antonov, B.N. Harmon, A.N. Yaresko, and A.Y. Perlov. Fully relativistic spin-polarized LMTO calculations of the magneto-optical Kerr effect of d and f ferromagnetic materials. III. Uranium chalcogenides and pnictides. *Phys. Rev. B*, 59:14571 – 14582, 1999.

[159] B. Johansson. Nature of the $5f$ electrons in the actinide series. *Phys. Rev. B*, 11:2740 – 2743, 1975.

[160] H.L. Skriver, O.K. Andersen, and B. Johansson. Calculated Bulk Properties of the Actinide Metals. *Phys. Rev. Lett.*, 41:42 – 45, 1978.

[161] H.L. Skriver, O.K. Andersen, and B. Johansson. 5f-electron Delocalization in Americium. *Phys. Rev. Lett.*, 44:1230 – 1233, 1980.

[162] M.S.S. Brooks and H.L. Skriver. In A.J. Freeman and G.H. Lander, editors, *Handbook on the Physics and Chemistry of the Actinides*. 1984.

[163] H.H. Hill. The early "Actinides": the periodic systems's f electron transition metal series. In W.N. Miner, editor, *Plutonium and other actinides: International Conference*, 1970.

[164] G.R. Stewart. Non-Fermi-liquid behavior in d- and f-electron metals. *Rev. Mod. Phys.*, 73:797 – 855, 2001.

[165] J.L. Sarrao, L.A. Morales, J.D. Thompson, B.L. Scott, F. Stewart, G.R. Wastin, J. Rebizant, P. Boulet, E. Colineau, and G.H. Lander. Plutonium-based superconductivity with a transition temperature above 18 K. *Nature*, 420:297 – 299, 2002.

[166] S. Elgazzar, J. Rusz, M. Amft, P.M. Oppeneer, and J.A. Mydosh. Hidden order in URu_2Si_2 originates from Fermi surface gapping induced by dynamic symmetry breaking. *Nature Materials*, 8:337 – 341, 2009.

[167] J.M. Wills and O. Eriksson. Actinide Ground-State Properties. *Los Alamos Science*, 26:128 – 151, 2000.

[168] J.S. Olsen, L. Gerward, and U. Benedict. A New High-Pressure Phase of Uranium Nitride Studied by X-ray Diffraction and Synchrotron Radiation. *J. Appl. Cryst.*, 18:37 – 41, 1985.

[169] O. Vogt and K. Mattenberger. Magnetic measurements on rare earth and actinide monopnictides and monochalcogenides. In K.A. Gscheidner Jr., L. Eyring, G.H. Lander, and G.R. Choppin, editors, *Handbook on the Physics and Chemistry of Rare Earths*, volume 17, pages 302 – 398. Elsevier, 1993.

[170] G. Busch, O. Vogt, A. Delapalme, and G.H. Lander. Magnetisation and neutron studies of UTe and $USb_{0.8}Te_{0.2}$. *J. Phys. C*, 12:1391 – 1401, 1979.

[171] D.L. Tillwick and P.d.V du Plessis. Large magnetic anisotropy in single crystal US. *J. Magn. Magn. Mater.*, 3:329 – 336, 1976.

[172] F.A. Wedgwood and M. Kuznietz. Actinide pnictides and chalcogenides : I. Study of magnetic ordering and ordered moments in uranium monochalcogenides by neutron diffraction. *J. Phys. C*, 5:3012 – 3020, 1972.

[173] G.H. Lander, M.S.S. Brooks, B. Lebech, P.J. Brown, O. Vogt, and Mattenberger K. Measurement of anisotropy constant in US with polarized neutrons (invited). *J. Appl. Phys.*, 69:4803 – 4806, 1991.

[174] A. Bombardi, N. Kernavanois, P. Dalmas de Réotier, G.H. Lander, J.P. Sanchez, A. Yaouanc, P. Burlet, E. Lelièvre-Berna, A. Rogalev, O. Vogt, and K. K. Mattenberger. On the evolution of the ground state in the system $U_xLa_{1-x}S$: Polarized neutron diffraction and X-ray magnetic circular dichroism study. *Euro. Phys. J. B*, 21:547 – 552, 2001.

[175] T. Herrmannsdörfer, P. Fischer, K. Mattenberger, and O. Vogt. Temperature dependences of rhombohedral lattice distortion and of ferromagnetic uranium ordering in the uranium monochalcogenides. *J. Alloys Compd.*, 414:14 – 19, 2006.

[176] T. Le Bihan, M. Idiri, and S. Heathman. New investigation of pressure-induced rhombohedral distortion of uranium nitride. *J. Alloys Compd.*, 358:120 – 125, 2003.

[177] N.A. Curry. An investigation of magnetic strucutre of uranium nitride by neutron diffraction. *Proc. Phys. Soc.*, 86:1193 – 1198, 1965.

[178] R. Troć. Magnetic susceptibility of the uranium nitrides. *J. Solid State Chem.*, 13:14 – 23, 1975.

[179] P.d.V. du Plessis and C.F. van Doorn. Magnetic susceptibility, electrical resistivity and elastic constants of antiferromagnetic un single crystals. *Physica B+C*, 86 - 88:993 – 994, 1977.

[180] T.M. Holden, W.J.L. Buyers, E.C. Svensson, J.A. Jackman, A.F. Murray, O. Vogt, and P.d.V. du Plessis. Magnetic excitations and lattice vibrations in uranium rock-salt structure compounds. *J. Appl. Phys.*, 53:1967 – 1972, 1982.

[181] J.A.C. Marples, C.F. Sampson, F.A. Wedgwood, and M. Kuznietz. Actinide pnictides and chalcogenides: IV. X-ray search for tetragonal distortion in UN and UAs in the antiferromagnetic state. *J. Phys. C:Solid State Phys.*, 8:708 – 716, 1975.

[182] T. Muromura and H. Tagawa. Lattice parameter of uranium mononitride. *J. Nucl. Mater.*, 79:264 – 266, 1979.

[183] M. Erbudak and J. Keller. Electronic Structure of Cubic Uranium Compounds. 32:281 – 286, 1979.

[184] M.S.S. Brooks and D. Glötzel. Some Aspects of the Electronic Structure of Uranium Pnictides and Chalcogenides. *Physica B*, 102:51 – 58, 1980.

[185] M.S.S. Brooks and D. Glötzel. Relativistic energy bands of NaCl structure uranium compounds. *Journal of Magnetism and Magnetic Materials*, 15 - 18:873 – 874, 1980.

[186] M.S.S. Brooks. Electronic structure of the actinide nitride series. *Journal of Magnetism and Magnetic Materials*, 29:257 – 261, 1982.

[187] M.S.S. Brooks. Electronic structure of NaCl-type compounds of the light actinides: I. UN, UC and UO. *J.Phys. F: Met. Phys.*, 14:639 – 652, 1984.

[188] M.S.S. Brooks. Electronic structure of NaCl-type compounds of the light actinides. III. The actinide nitride series. *J.Phys. F: Met. Phys.*, 14:857 – 871, 1984.

[189] P. Weinberger, C.P. Mallett, R. Podloucky, and A. Neckel. The electronic structure of HfN, TaN and UN. *J. Phys. C: Solid State Phys*, 13:173 – 187, 1980.

[190] E.A. Kotomin, R.W. Grimes, Y. Mastrikov, and N.J Ashley. Atomic scale DFT simulations of point defects in uranium nitride. *J. Phys.: Condens. Matter*, 19:106208, 2007.

[191] P.F. Weck, E. Kim, N. Balakrishnan, F. Poineau, C.B. Yeamans, and R. Kenneth Czerwinski. First-principles study of single-crystal uranium mono- and dinitride. *Chem. Phys. Lett.*, 443:82 – 86, 2007.

[192] M. Samsel-Czekała, E. Talik, P.d.V. de V. du Plessis, R. Tro ć, H. Misiorek, and C. Sułkowski. Electronic structure and magnetic and transport properties of single-crystalline UN. *Phys. Rev. B*, 76:144426, 2007.

[193] L. Petit, A. Svane, Z. Szotek, W.M. Temmerman, and G.M. Stocks. Ground-state electronic structure of actinide monocarbides and mononitrides. *Phys. Rev. B*, 80:045124, 2009.

[194] R. Atta-Fynn and A.K. Ray. Density functional study of the actinide nitrides. *Phys. Rev. B*, 76:115101 – 115112, 2007.

[195] T.M. Holden, W.J.L. Buyers, E.C. Svensson, and G.H. Lander. Magnetic excitations in uranium nitride. *Phys. Rev. B*, 30:114 – 121, 1984.

[196] A. Solontsov and V.P. Silin. Uranium nitride-a spin polarized weak itinerant electron antiferromagnet with strongly correlated electrons. *Physics Letters A*, 334:453 – 459, 2005.

[197] I.M. Lifshitz. Anomalies of electron characteristics of a metal in the high pressure region. *Soviet Physics JETP*, 11:1130 1135, 1960.

[198] J.M. Fournier and R. Troć. In A.J. Freeman and G.H. Lander, editors, *Handbook on the Physics and Chemistry of the Actinides*, volume 2, pages 29 – 174. North-Holland Amsterdam, 1985.

[199] Q.G. Sheng and B.R. Cooper. Pressure-induced magnetic ordering effects in correlated-electron uranium monochalcogenides. *J. Magn. Magn. Mater.*, 164:335 – 344, 1996.

[200] S. Langridge, G.H. Lander, N. Bernhoeft, A. Stunault, C. Vettier, G. Grübel, C. Sutter, F. de Bergevin, W.J. Nuttall, W.G. Stirling, K. Mattenberger, and O. Vogt. Separation of the spin and orbital moments in antiferromagnetic UAs. *Phys. Rev. B*, 55:6392 – 6398, 1997.

[201] N. Kernavanois, P. Dalmas de Réotier, A. Yaouanc, J.-P. Sanchez, V. Honkimä, T. Tschentscher, J. McCarthy, and V. Vogt. Orbital and spin magnetism in US-comparison with USe and UTe. *J.Phys.: Condens. Matter*, 13:9677 – 9690, 2001.

[202] E.M. Collins, N. Kioussis, S.P. Lim, and B.R. Cooper. Ab initio study of anisotropic magnetism in uranium compounds. *J. Appl. Phys.*, 85:6226 – 6228, 1999.

[203] H. Yamagami. Fully relativistic noncollinear magnetism in spin-density-functional theory: Application to USb by means of the fully relativistic spin-polarized LAPW method. *Phys. Rev. B*, 61:6246 – 6256, 2000.

[204] K. Knöpfle and L. M. Sandratskii. Multiple k magnetic structure and Fermi surface of USb. *Phys. Rev. B*, 63:014411, 2000.

[205] V.N. Antonov, B.N. Harmon, O.V. Andryushchenko, L.V. Bekenev, and A.N. Yaresko. Electronic structure and x-ray magnetic circular dichrosim in uranium monochalcogenides. *J. Low Temp. Phys.*, 30:305 – 316, 2004.

[206] T. Kraft, P.M. Oppeneer, V.N. Antonov, and H. Eschrig. Relativistic calculations of the magneto-optical Kerr spectra in (001) and (111) US, USe, and UTe. *Phys. Rev. B*, 52:3561 – 3570, 1995.

[207] L. Severin, M.S.S. Brooks, and B. Johansson. Relationship between the Coulomb Integral U and the Stoner Integral I. *Phys. Rev. Lett.*, 71:3214 – 3217, 1993.

[208] T. Shishidou and T. Oguchi. Band-theoretical prediction of magnetic anisotropy in uranium monochalcogenides. *Phys. Rev. B*, 62:11747 – 11750, 2000.

[209] H. Yamagami. All-Electron Spin-Polarized Relativistic Linearized APW Method: Electronic and Magnetic Properties of BCC Fe, HCP Gd and Uranium Monochalcogenides. *J. Phys. Soc. Jpn.*, 67:3176 – 3190, 1998.

[210] S. Suzuki, T. Ariizumi, and M.F. Li. Mulliken Population Analysis of X-ray Magnetic Circular Dichroism in Uranium Monochalcogenides: Examination of Sum Rules by Fully Relativistic Full-Potential LCAO Method. *Journal of the Physical Society of Japan*, 78:074715, 2009.

[211] S. Suzuki and H. Ohta. Fully Relativistic Full-Potential Calculations of Magnetic Moments in Uranium Monochalcogenides with the Dirac Current. *Journal of the Physical Society of Japan*, 79:074703, 2010.

[212] A.M. Strydom and P.d.V. du Plessis. Critical properties of uranium selenide. *J. Magn. Magn. Mater.*, 119.

[213] O. Vogt. Magnetization Measurements on Single Crystals of Uranium Chalcogenides and Pnictides. *Physica B+C*, 102:206 – 211, 1980.

[214] J. Rossat-Mignod, P. Burlet, S. Quezel, and O. Vogt. Magnetic ordering in cerium and uranium monopnictides. *Physica B+C*, 102:237 – 248, 1980.

[215] G.H. Lander and P. Burlet. On the magnetic structure of actinide monopnictides. *Physica B*, 215:7 – 21, 1995.

[216] G.H. Lander, M.S.S. Brooks, B. Lebech, P.J. Brown, O. Vogt, and K. Mattenberger. Measurement of giant magnetic anisotropy in a uranium compound. *Appl. Phys. Lett.*, 57:989 – 991, 1990.

[217] A.P. Gonçalves, M.S. Henriques, J.C. Waerenborgh, L.C.J. Pereira, E.B. Lopes, M. Almeida, S. Mašková, L. Havela, A.B. Shick, Z. Arnold, D. Berthebaud, O. Tougait, and H. H Noël. Peculiarities of U-based Laves phases. *IOP Conf. Series: Mater. Sci. Eng.*, 9:012090, 2010.

[218] L. Severin, L. Nordström, M.S.S. Brooks, and B. Johansson. Theoretical study of the ferromagnetism in UNi_2. *Phys. Rev. B*, 44:9392 – 9399, 1991.

[219] P. Villars and L.D. Calvert. *Pearson's Handbook of Crystallgraphic Data for Intermetallic Phases*, volume 1 - 4. ASM International, 1991.

[220] R.M. White. *Quantum Theory of Magnetism*. Springer-Verlag Berlin, 1983.

[221] M.S.S. Brooks and B. Johansson. Exchange integral matrices and cohesive energies of transition metal atoms. *J.Phys. F: Met. Phys*, 13:L197 – L202, 1983.

[222] M.S.S. Brooks, O. Eriksson, B. Johansson, J.J.M. Franse, and P.H. Frings. Chemical bonding and magnetism in 3d-5f intermetallics. *J. Phys. F: Met. Phys.*, 18:L33 – L39, 1988.

[223] S.T. Lin and A.R. Kaufmann. Magnetic Properties of UMn_2. *Phys. Rev.*, 108:1171 – 1174, 1957.

[224] G.R. Marpoe and G.H. Lander. Observation of a structural transition from cubic to monoclinic in UMn_2. *Solid State Communications*, 26:599 – 602, 1978.

[225] R. Grössinger, G. Hilscher, J. Kamesberger, H. Sassik, G. Wiesinger, V. Sechovský, and J. J. Toul. Onset of magnetism and the crystallographic distortion in $U(Fe_{1-x}Mn_x)_2$. *J. Magn. Magn. Mater.*, 29:305 – 313, 1982.

[226] S. Giri, H. Nakamura, and M. Shiga. ^{55}Mn NMR and NQR study of the cubic Laves-phase compound UMn_2. *Phys. Rev. B*, 61:12233 – 12240, 2000.

[227] A.M. Boring, R.C. Albers, G.H. Schadler, A.C. Lawson, P. Weinberger, and N.E. Christensen. Electronic structure and magnetic behavior of UMn_2 and UFe_2. *Phys. Rev. B*, 36:5507 – 5511, 1987.

[228] O. Eriksson, B. Johansson, H.L. Skriver, and M.S.S. Brooks. Electronic structure of the uranium-$3d$ transition metal laves phases. *Physica B+C*, 144:32 – 40, 1986.

[229] M. Wulff, G.H. Lander, B. Lebech, and A. Delapalme. Cancellation of orbital and spin magnetism in UFe_2. *Phys. Rev. B*, 39:4719 – 4721, 1989.

[230] M. Wulff, B. Lebech, A. Delapalme, G.H. Lander, J. Rebizant, and J.C. Spirlet. U form factor and 3d-5f hybridization in UFe₂. *Physica B*, 156 - 157:836 – 838, 1989.

[231] M. Finazzi, P. Sainctavit, A.M. Dias, J.P. Kappler, G. Krill, J.P. Sanchez, P. Dalmas de Réotier, A. Yaouanc, A. Rogalev, and J. Goulon. X-ray magnetic circular dichroism at the U $M_{4,5}$ absorption edges of UFe₂. *Phys. Rev. B*, 55:3010 – 3014, 1997.

[232] V.N. Antonov, B.N. Harmon, and A.N. Yaresko. Electronic structure and x-ray magnetic circular dichroism in uranium compounds. I. UFe₂. *Phys. Rev. B*, 68:214424, 2003.

[233] D. Benea, S. Mankovsky, and H. Ebert. Fully relativistic description of magnetic Compton profiles with an application to UFe_2. *Phys. Rev. B*, 73:094411, 2006.

[234] O. Eriksson, M.S.S. Brooks, and B. Johansson. Theoretical aspects of the magnetism in the ferromagnetic AFe₂ systems (A = U, Np, Pu, and Am). *Phys. Rev. B*, 41:9087 – 9094, 1990.

[235] P.K. Lawson, M.J. Cooper, M.A.G. Dixon, D.N. Timms, E. Zukowski, F. Itoh, and H. Sakurai. Magnetic-Compton-scattering study of spin moments in UFe₂. *Phys. Rev. B*, 56:3239 – 3243, 1997.

[236] J. Hrebik and B. R. Coles. The influence of non-stoichiometry on the magnetic properties of UCo₂. *Physica B+C*, 86 - 88:169 – 170, 1977.

[237] J.J.M. Franse. Itinerant-electron magnetism studied in high-magnetic field and high-pressure experiments. *J. Magn. Magn. Mater.*, 31 - 34:819 – 828, 1983.

[238] V. Sechovský, Z. Smetana, G. Hilscher, E. Gratz, and H. Sassik. Onset of ferromagnetism in U(Co$_x$Ni$_{1-x}$)₂. *Physica B+C*, 102:277 – 281, 1980.

[239] P.H. Frings, J.J.M. Franse, A. Menovsky, S. Zemirli, and B. Barbara. Magnetic properties of single-crystalline UNi₂. *J. Magn. Magn. Mater.*, 54 - 57:541 – 542, 1986.

[240] J.M. Fournier, A. Boeuf, P. Frings, M. Bonnet, J. v. Boucherle, A. Delapalme, and A. Menovsky. Polarived neutron diffraction study of UNi₂. *Journal of the Less Common Metals*, 121:249 – 252, 1986.

[241] G. Hilscher and V. Sechovský. The Origin of Magnetism in UNi₂ - A Simple Band Approach. *Solid State Communications*, 40:881 – 884, 1981.

[242] P. Wiśniewski, A. Gukasov, Z. Henkie, and A. Wojakowski. Polarized neutron diffraction study of spin and orbital moments in UAsSe. *J. Phys.: Condens. Matter*, 11:6311 – 6317, 1999.

[243] J. Leciejewicz, R. Troć, A. Murasik, and A. Zygmunt. Neutron-Diffraction Study of Antiferromagnetism in USb$_2$ and UBi$_2$. *Phys. Stat. Sol. (b)*, 22:517 – 526, 1967.

[244] Z. Henkie, R. Fabrowski, A. Wojakowski, and A.J. Zaleski. Suppression of the ferromagnetic state by disorder in the anisotropic Kondo lattice system UAsSe. *J. Magn. Magn. Mat.*, 140-144:1433 – 1434, 1995.

[245] A. Zygmunt and M. Duczmal. Magnetic properties of UAsY compounds (Y = S, Se, Te). *Phys. Stat. Sol. (a)*.

[246] J. Brunner, M. Erbudak, and F. Hulliger. Localized 5f-electrons in metallic UAsSe. *Solid State Commun.*, 38:841 – 843, 1981.

[247] Z. Henkie, A. Pietraszko, A. Wojakowski, L. Kecpiński, and T. Cichorek. Crystallochemistry and Kondo-like behaviour of the thorium and uranium arsenoselenides. *J. Alloys Compd.*, 317 - 318:52 – 59, 2001.

[248] W. Reim. Magneto-optical Kerr-effect of uranium compounds: A study of the electronic structure. *J. Magn. Magn. Mater.*, 58:1 – 47, 1986.

[249] P.M. Oppeneer, M.S.S. Brooks, V.N. Antonov, T. Kraft, and H. Eschrig. Band-theoretical description of the magneto-optical spectra of UAsSe. *Phys. Rev. B*, 53:R10437 – R10440, 1996.

[250] E. Guziewicz, T. Durakiewicz, P.M. Oppeneer, J.J. Joyce, J.D. Thompson, C.G. Olson, M.T. Butterfield, A. Wojakowski, D.P. Moore, and A.J. Arko. Angle-resolved photoemission study of dispersive and narrow-band 5f states in UAsSe. *Phys. Rev. B*, 73:155119, 2006.

[251] D.V. Efremov, N. Hasselmann, E. Runge, P. Fulde, and G. Zwicknagl. Dual nature of 5f electrons: Effect of intra-atomic correlations on hopping anisotropies. *Phys. Rev. B*, 69:115114, 2004.

[252] E. Guziewicz, T. Durakiewicz, M.T. Butterfield, C.G. C.G. Olson, J.J. Joyce, A.J. A.J. Arko, J.L. Sarrao, A. Wojakowski, and T. Cichorek. Electronic Structure of UAsSe and USb$_2$ Compounds: The 5f Photoemission. In *Materials Research Society Symposium Proceedings*, volume 802, pages 183 – 187. Materials Research Society, 2004.

[253] D. Aoki, P. Wiśniewski, K. Miyake, N. Watanabe, Y. Inada, R. Settai, E. Yamamoto, Y. Haga, and Y. Ōnuki. Crystal Growth and Cylindrical Fermi Surfaces of USb$_2$. *J. Phys. Soc. Jpn.*, 68:2182 – 2185, 1999.

[254] D. Aoki, P. Wìniewski, K. Miyake, N. Watanabe, Y. Inada, R. Settai, E. Yamamoto, Y. Haga, and Y. Onuki. Cylindrical Fermi surfaces formed by a fiat magnetic Brillouin zone in uranium dipnictides. *Philos. Mag. B*, 80:1517 – 1544, 2000.

[255] S. Lebègue, P.M. Oppeneer, and O. Eriksson. Ab initio study of the electronic properties and Fermi surface of the uranium dipnictides. *Phys. Rev. B*, 73:045119, 2006.

[256] X. Yang, P.S. Riseborough, T. Durakiewicz, C.G. Olson, J.J. Joyce, E.D. Bauer, J.L. Sarrao, D.P. Moore, K.S. Graham, S. Elgazzar, P.M. Oppeneer, E. Guziewicz, and M.T. Butterfield. Unusual quasiparticle renormalizations from angle resolved photoemission on USb$_2$. *Philosophical Magazine*, 89:1893 – 1911, 2009.

[257] R.L. Withers, H.J.P. van Midden, A. Prodan, P.A. Midgley, J. Schoenes, and R. Vincent. As-As dimerization, Fermi surfaces and the anomalous electrical transport properties of UAsSe and ThAsSe. *J. Solid State Chem.*, 179:2190 – 2198, 2006.

[258] J. Leciejewicz, R. Troć, A. Murasik, and A. Zygmunt. Erratum. *Phys. Stat. Sol. (b)*, 24:723, 1967.

[259] H. Zhang. PhD thesis, 2009.

[260] J.D. Jackson. *Classical Electrodynamics.* John Wiley and Sons, 1975.

Acknowledgment

At this point, I want to thank everyone who supported me during the last years. I want to mention that without their support the success of this thesis could not be assured.

First I would like to thank Prof. Dr. H. Eschrig. He gave me the opportunity for this work. Furthermore, his professional guidance and support let me gain an insight in many interesting domains in physics. During his lectures, he carefully explained the origin of mathematical formulae and how they are to understand in a physical sense. This knowledge helped me to get a broader impression of physics, not only of solid state physics, but also to get the connection between formally different ideas and theories in modern physics.

The second thanks are given to Dr. M. Richter, who helped me every time with all kind of problems, physical or non-physical. He spent a large effort in correcting my presentations and my thesis. Thus, with the help of his critical suggestions, the quality of presenting my results were improved. In our discussion he drove my ideas to new topics, with which I explored new features. He also encouraged me to check results twice to be sure of numerical stability.

Many thanks with respect to numerical problems are given to Dr. K. Koepernik, Dr. I. Opahle, and Ms. U. Nitzsche. Dr. Koepernik developes the FPLO package and with his new releases it was possible to get more precise results, and of course faster. I enjoyed a lot discussions about physics, as well as he gave me a lot of ideas and suggestions to solve my problems. The same holds for Dr. Opahle. Also, both of them left me small programmes, which made my life more comfortable. Ms. Nitzsche took care of the system administration, she managed that the computer system was very stable over the years and this approved a work without engine idling. In addition, we had many philosophical discussions about the sense of Linux and other commercial operating systems.

I want to thank all my colleagues, which whom i have shared a room. Especially Dr. H. Zhang and Mr. S. Schönecker. Both of them are more than colleagues. We talked not only a lot about physical problems, but we spent our spare time together as well. Further, discussions with PD. Dr. A. Möbius, Dr. M. Sargolzaei, Dr. F. Tasnadi, Dr. S. Elgazzar, Mr. M. Bayer, and many more gave me suggestions for problems of the daily life. Miss A. Heinrich and Miss G. Roetzer take care of my administrative problems, so many thanks to them for their help to let me find the correct bus every time.

I am glad to met the new dutch group at the end of my studying. I want to thank them for having nice discussions and giving me the opportunity to see the world from a different angle. So, i want to thank Dr. C. Ortix, Dr. S. Johnston, Dr. L. Ament, Mr. J. Venderbos, and Mr. Kien Trinh.

At last, but not least I want to thank my family, including my parents, my sister and my brother-in-law, as well as my niece and my nephew. I want to thank a special girl, Miss S. Bläsche, for sharing life for some years. I want also to mention my best friends Mr. M. Flehmig, Mr. D. Wieltsch, Dr. T. Klauss, Mr. F. Roth, Mr. M. Willig, Mr. K. Knebel and many more. They exhibited appreciation of my efforts and always encouraged me in my work.

Versicherung

Hiermit versichere ich, dass ich die vorliegende Arbeit ohne unzulässige Hilfe Dritter und ohne Benutzung anderer als der angegebenen Hilfsmittel angefertigt habe, die aus fremden Quellen direkt oder indirekt übernommenen Gedanken sind als solche kenntlich gemacht. Die Arbeit wurde bisher weder im Inland noch im Ausland in gleicher oder ähnlicher Form einer anderen Prüfungsbehörde vorgelegt. Die Arbeit entstand mit wissenschaftlicher Betreuung durch Prof. Helmut Eschrig am Leibniz-Institut für Festkörper- und Werkstoffforschung Dresden. Ich habe vorher kein anderes Promotionsverfahren eröffnet. Ich erkenne die Promotionsordnung der Fakultät Mathematik und Naturwissenschaften der Technischen Universität Dresden in der aktuell gültigen Fassung an.

_____   _____
Ort, Datum   Carsten Neise